Presentata in Segreteria il 2/11/88

IL SEGRETARIO

UNIVERSITA' DEGLI STUDI DI PISA

Facolta' di Scienze Matematiche Fisiche e Naturali
Corso di laurea in fisica

Tesi di laurea :

DIMUON PRODUCTION AT CDF

Relatori :

Ch.ma Prof.sa M. Franklin
Ch.mo Prof. G. Bellettini

Controrelatori :

Ch.mo Prof. R. Castaldi
Ch.mo Prof I. Mannelli

Candidato :

- Marco Incagli -

ANNO ACCADEMICO 1987/1988

Presentata in Segreteria il 2/11/88

IL SEGRETARIO

UNIVERSITA' DEGLI STUDI DI PISA

Facolta' di Scienze Matematiche Fisiche e Naturali
Corso di laurea in fisica

FERMILAB-MASTERS-1988-03

Tesi di laurea :

DIMUON PRODUCTION AT CDF

Relatori :

Ch.ma Prof.sa M. Franklin
Ch.mo Prof. G. Bellettini

Controrelatori :

Ch.mo Prof. R. Castaldi
Ch.mo Prof I. Mannelli

Candidato :

- Marco Incagli -

ANNO ACCADEMICO 1987/1988

TABLE OF CONTENTS

TESINE:

1) Solitoni per il trasporto di energia e loro esistenza a Temperature biologiche

RELATORE Ch.mo Prof. GREGOLINI

2) Modello di evoluzione per le galassie a spirale.

RELATORE Ch.mo Prof. FERRINI

3) Uso di raggi-X mouili in archeologia

RELATORE Ch.mo prof. BRACCI

1 INTRODUCTION

1.1 - The Standard Model

The theoretical model that is best able to explain the present experimental data, is known as the "Standard Model" [1]. The fundamental particles are spin 1/2 fermions (and the relative anti-fermions) grouped in two families :

$$\text{LEPTONS} \begin{bmatrix} e \\ \nu_e \end{bmatrix} \begin{bmatrix} \mu \\ \mu_\nu \end{bmatrix} \begin{bmatrix} \tau \\ \nu_\tau \end{bmatrix} \begin{matrix} Q = -1 \\ Q = 0 \end{matrix} \quad \text{QUARKS} \begin{bmatrix} u \\ d \end{bmatrix} \begin{bmatrix} c \\ s \end{bmatrix} \begin{bmatrix} (t) \\ b \end{bmatrix} \begin{matrix} Q = 2/3 \\ Q = -1/3 \end{matrix}$$

The top quark ("t") has not been observed, yet. The 12 fermions are grouped in isospin doublets.

These particles undergo three different types of fundamental interactions , all mediated by spin 1 bosons . They are :

- *Strong interactions* mediated by eight massless gluons and coupled to a charge called colour .
- *Electromagnetic interactions* mediated by massless photons coupled to the electric charge .
- *Weak interactions* mediated by massive bosons ($W^{\pm}$, Z°) coupled to weak isospin .

There is also a fourth fundamental interaction, gravitation, that is not included in the "Standard model" .

Leptons undergo weak and, if charged, electromagnetic interactions; quarks all of them .

Electromagnetic interactions are described by *Quantum-Electro Dynamics* (QED). QED is based on a U(1) symmetry . The conserved current related to the simmetry, is the electric charge *e* .

Glashow, Salam and Weinberg [2] incorporated the laws of electromagnetism and weak interactions in one unified model. This model is based on a Non-Abelian, spontaneously broken symmetry SU(2) $\otimes$ U(1) . The breaking of the symmetry is the reason why the

eigenstgates of the Weak Interactions hamiltonian are massive bosons. Three of them form a triplet, and for this they are called vector Bosons, while the other is a singlet state. The two neutral physical states, Z° and γ, are not the eigenstates of the weak hamiltonian. They are a mixture of the two eigenstates, B° and W°, determined by the Weinberg angle θ_w :

$$\begin{bmatrix} Z^\circ \\ \gamma \end{bmatrix} = \begin{bmatrix} \cos\theta_W & \sin\theta_W \\ -\sin\theta_W & \cos\theta_W \end{bmatrix} \begin{bmatrix} W^\circ \\ B^\circ \end{bmatrix}$$

The Weinberg angle is chosen so that the photon is massless.

The masses of the three vector bosons can be expressed in terms of the same parameter, the Weinberg angle θ_w , in the following way :

$$M^2_{W^\pm} = \frac{\pi\alpha}{2G^2} \frac{1}{\sin^2\theta_w}$$

$$M^2_{Z^\circ} = \frac{2\pi\alpha}{G^2} \frac{1}{\sin^2 2\theta_W}$$

In analogy to QED, Quantum Chromo-Dynamics (QCD) was developed for the strong interactions. QCD is a non-abelian exact SU(3) symmetry coupled to a conserved charge called *colour* . The carriers of this charge are called *gluons* . Gluons and quarks, both, are called *partons* . Quarks are held together by strong interactions mediated by gluons . The coupling constant of strong interactions, α_s, can be expressed as a function of the relative distance, or, equivalently, as a function of the momentum Q^2 transferred between coloured states :

$$\alpha_s = \frac{12\pi}{(33-2f)\,\mathrm{Ln}\,Q^2/\Lambda^2} .$$

f is the number of existing quarks, or *flavours* , and Λ is a constant determining the scale of strong interactions. The generally accepted

value of Λ is : Λ = 200MeV. It corresponds to a distance between quarks of about 1 fm. When we are probing quarks at short distances (r«1fm) or, equivalently, with very high energies ($Q^2 \gg \Lambda^2$) , $\alpha_s \rightarrow 0$. This means that quarks behave as free particles. On the other hand, when quarks are far apart, that is $Q^2 \ll \Lambda^2$, $\alpha_s \rightarrow \infty$. Because of this quarks are bound inside hadrons. The two opposite behaviours, at high and at low energies, are known as *asymptotic freedom*, $\alpha_s \rightarrow 0$, and *quark confinement*, $\alpha_s \rightarrow \infty$.

At Tevatron energies ($\sqrt{s}$ = 1800 GeV) the momentum exchanged between partons can be high enough to consider them as free particles and parton-parton interactions as pointlike. This allows us to make kinematic predictions of parton-parton scattering and of the resulting event topology.

The outcoming partons fragment into group of colourless particles. Because of their characteristic form, these bundles of hadrons are called *jets* . An example of a jet event is shown in fig1.1. A good model providing a parametrization of the properties of jets of mesons, is by Field and Feynman [3] . The important parameter describing the fragmentation is :

$$Z = \frac{(P_{PAR})_{HAD}}{(P)_{QUARK}} .$$

where P_{PAR} is the component of the hadron momentum parallel to the quark momentum. For high momentum quarks z represents, approximately, the momentum fraction transferred to the hadron in the fragmentation process.

The fragmentation function, D(z), expresses the probability for a meson to keep a fraction z of the momentum of the outgoing parton.

Mesons produced by the fragmentation of light quarks, u-d-s, or by gluons have, on average, only 28% of the initial parton energy. Heavy quarks have a 'harder' fragmentation [4]. The average values of the parameter z is 59% , for c-quark , and 77% for b-quarks. That is mesons keep a higher fraction of the quark momentum. For

this reason jets from heavy quarks have a lower charge multiplicity, than light quarks jets, and are stiffer than the others.

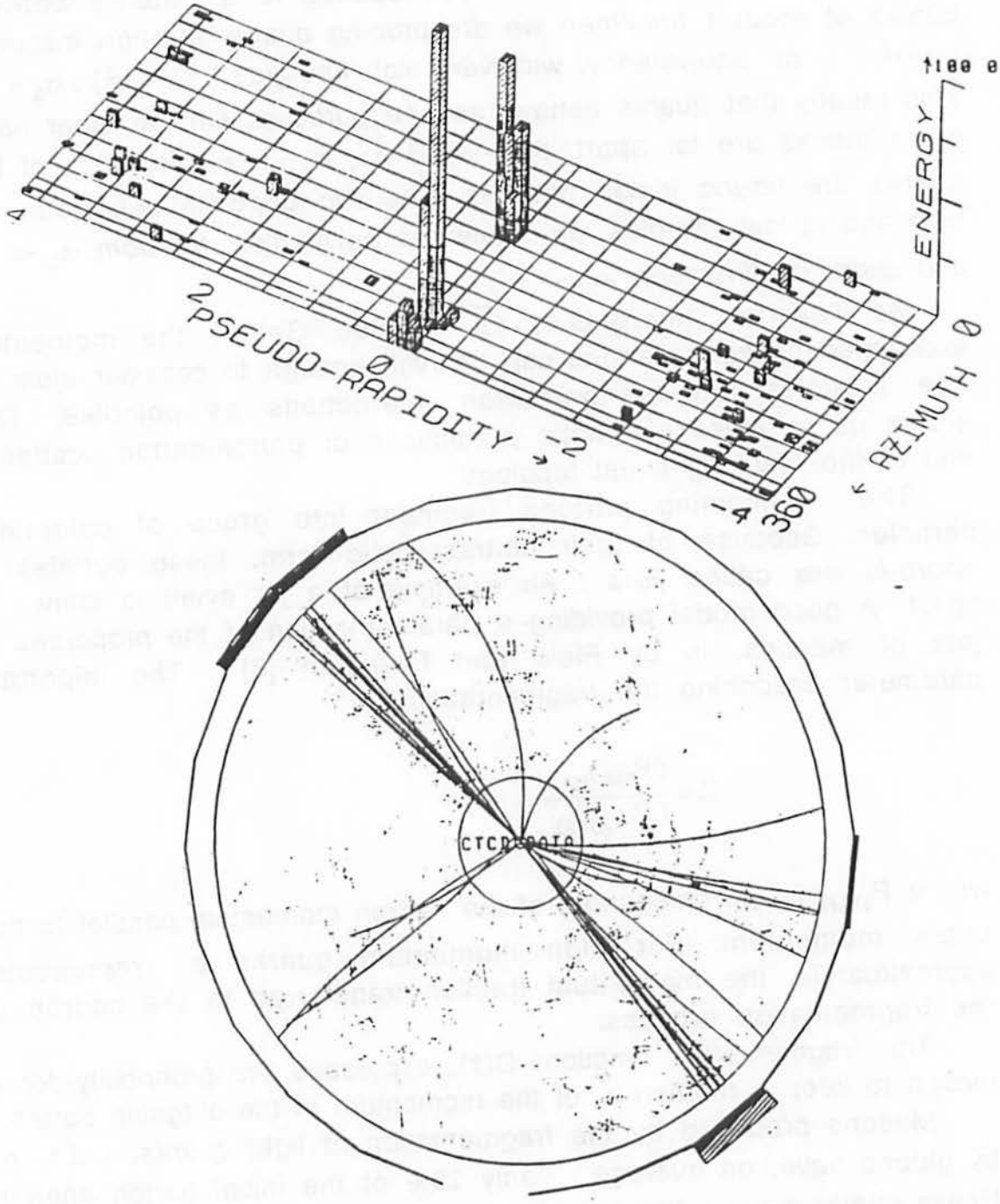

FIG 1.1 - Example of a jet event. The lower figure shows the reconstruction done in the Central Tracking Chamber (3.2) . It is evident the hadron activity concentrated in two cones approximately back to back.

Although the Standard Model is in good agreement with experiment it is not believed to be the ultimate theory.

1.2 - The p-$\bar{p}$ collider

In collider machines high center of mass energies are reached. In fact two beams of energy E colliding head to head result in a center of mass energy of $E^*=2E$. On the other hand a beam of energy E scattering on a fixed target of mass m results in a center of mass energy of $E^*\approx\sqrt{2mE}$. For example, the 900 GeV Tevatron beam allows center of mass energies of 1800 GeV, for $p\bar{p}$ collisions, and 40 GeV for collisions on a fixed proton target.

Existing colliders have p-$\bar{p}$ and e^+-e^- beams. In e^+-e^- collisions lower energies can be reached. The reason for this is that some energy is lost by *synchroton radiation* . This effect is not important in $p\bar{p}$ colliders because the energy lost in every revolution is proportional to M^{-4} . Therefore, for particles having the same momentum, it is $(M_p/m_e)^4 \approx 2000^4$ times bigger for electrons than for protons! For example an electron accelerated to 10 GeV in a 1km ring radius (Fermilab main ring's radius) radiates 1 MeV per turn rising up to 16 MeV for 20 GeV electrons. For a proton, this energy is $\approx 10^{13}$ times smaller.

On the other hand their are some disadvantages in using $p\bar{p}$ colliders. The first one is that the result of $p\bar{p}$ interactions have much a higher multiplicity of particles produced compared to e^+e^- collisions. In fact the proton is composed of quarks and gluons, therefore there are spectator partons to all hard scattering. This makes the reconstruction of the event more difficult. The second disadvantage is that the center of mass energy for elementary collisions, $\sqrt{s'}$, is smaller than the energy $\sqrt{s}$. However now and in the near future, the highest energies will be available at the hadron colliders, and this will generally overcompensate the small ratio s'/s . For all these reasons electron and proton accelerators constitute a complementary source of information in high energy physics.

The Fermilab synchroton is the $p\bar{p}$ collider with the highest

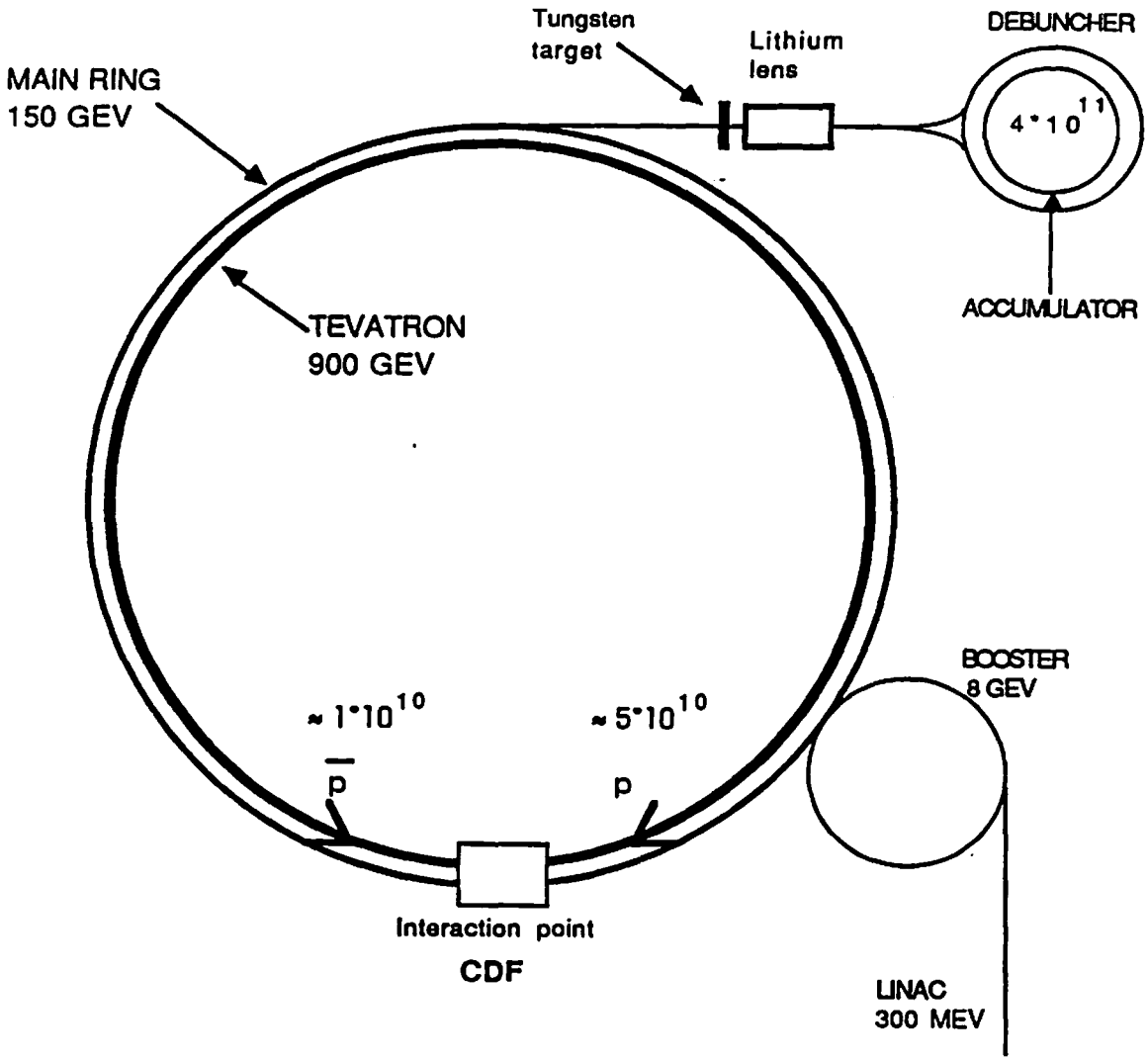

FIG 1.2 - Schematic view of fermilab synchroton. The linear accelarator and the other interaction points are not reported in the figure.
The Tevatron is situated 1-2 meters above the Main Ring. The Accumulator and the Debuncher are not exactly circular for technical convenience.

center of mass energy. Protons and anti-protons are accelarated to 900 GeV. A schematic drawing of the collider is reported in fig 1.2 .

Protons are originated in a gas bottle and they are accelerated to 200 MeV in a linear accelerator 150 m long (LINAC) . They are then

injected in a 70 m radius circular accelerator called the BOOSTER used for accelerating the particles up to 8 GeV and to reduce the momentum spread of the different bunches of protons down to 0.2%. After they have reached 8 GeV they enter the Main Ring, the old conventional electromagnetic accelerator. The Main Ring can reach energies of 400 GeV, but, since the installation of the Tevatron, it is used as an injector and it accelerates particles up to 150 GeV. The last step is the Tevatron. The Tevatron uses superconducting magnets. They provide high enough magnetic fields to allow the beam to reach energies of 900 GeV in a ring of the same radius as the Main Ring. About $5 * 10^{10}$ protons per bunch are accelerated in this way.

Protons accelerated in the Main Ring are extracted from the ring and collide on a tungsten target to produce anti-protons. In this way $7 * 10^{7}$ 8 GeV antiprotons per bunch are generated. They are focused by a lithium lense and they enter the DEBUNCHER with a momentum spread of 3% . In the DEBUNCHER they are organized in bunches having a 0.2 % momentum spread and they are injected in the ACCUMULATOR. In it successive bunches are accumuated using the technique of the stochastic cooling [5]. The stacking rate is $1\text{-}2 * 10^{10}$ anti-protons/hour . The total number of anti-protons per bunch is $\approx 1 * 10^{10}$. Therefore the time for the preparation of a *shot* (the injection into the Main Ring of the anti-protons, is about 3/4 hours, when three bunches are injected (1987 run), or six hours in a six bunches mode (1988 run) . After the accumulation is done the bunches of anti-protons are injected into the Main Ring and then into the Tevatron where they are accelerated together with the protons, but in the opposite direction, to 900 GeV. Table 1.1 summarizes all these steps.

The design goal is to have six bunches of protons and anti-protons accelerated. This would result in a beam crossing every 3.5 μs . Given the density of the bunches and the CM energy available, the design luminosity is $L \approx 10^{30}$ $cm^{-2}sec^{-1}$. During the 1987 run the peak luminosity was at $4 * 10^{29}$ $cm^{-2}sec^{-1}$ with 3 bunches of protons and antiprotons accelerated. The goal of 10^{30} $cm^{-2}sec^{-1}$ was reached during the first week of September 1988, with 6 bunches operation.

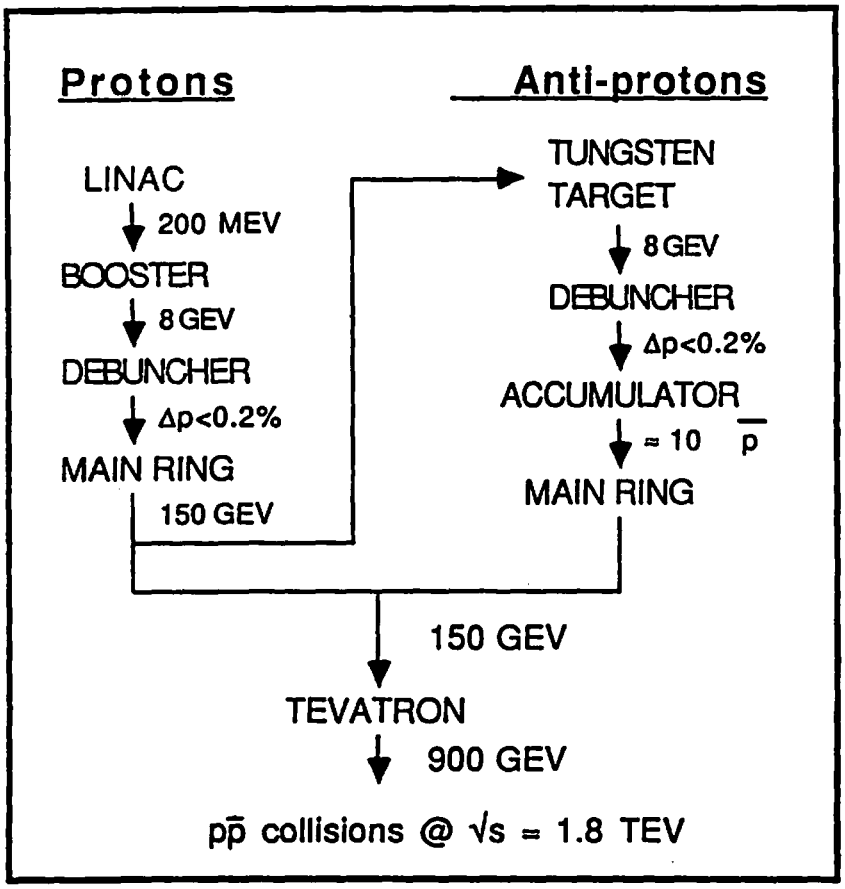

- TABLE 1.1 - $p\bar{p}$ path to the collision .

1.3 - Physics at the $p\bar{p}$ collider

In high energy proton-antiproton collisions we probe the internal structure of the nucleons. As already mentioned nucleons, and hadrons in general, are composed of partons. Partons are distributed inside the nucleons according to some probability functions. That is to say partons have not a fixed momentum, but a fraction x of the nucleon momentum. The value of x is determined by some probability distributions. They have been measured in deep inelastic scattering experiments, but little information are available on their behaviour at low values of x. In fig 1.3 a possible parametrization of these *distribution functions* is shown [6] .

Low values of x can be probed at the center of mass available at CDF of $\sqrt{s}$ = 1800 GeV . At this energy all the interactions described in section 1.1 contribute :

- *Weak interactions* : given the high center of mass energy ($\sqrt{s}$=1800 GeV), quarks and antiquarks can couple, with detectable

----- $x * G(x)$ = Gluon distribution

- - - $x * (u_v(x) + d_v(x))$ = Valence quark distribution

..... $q_v(x)$ = Sea quark distribution

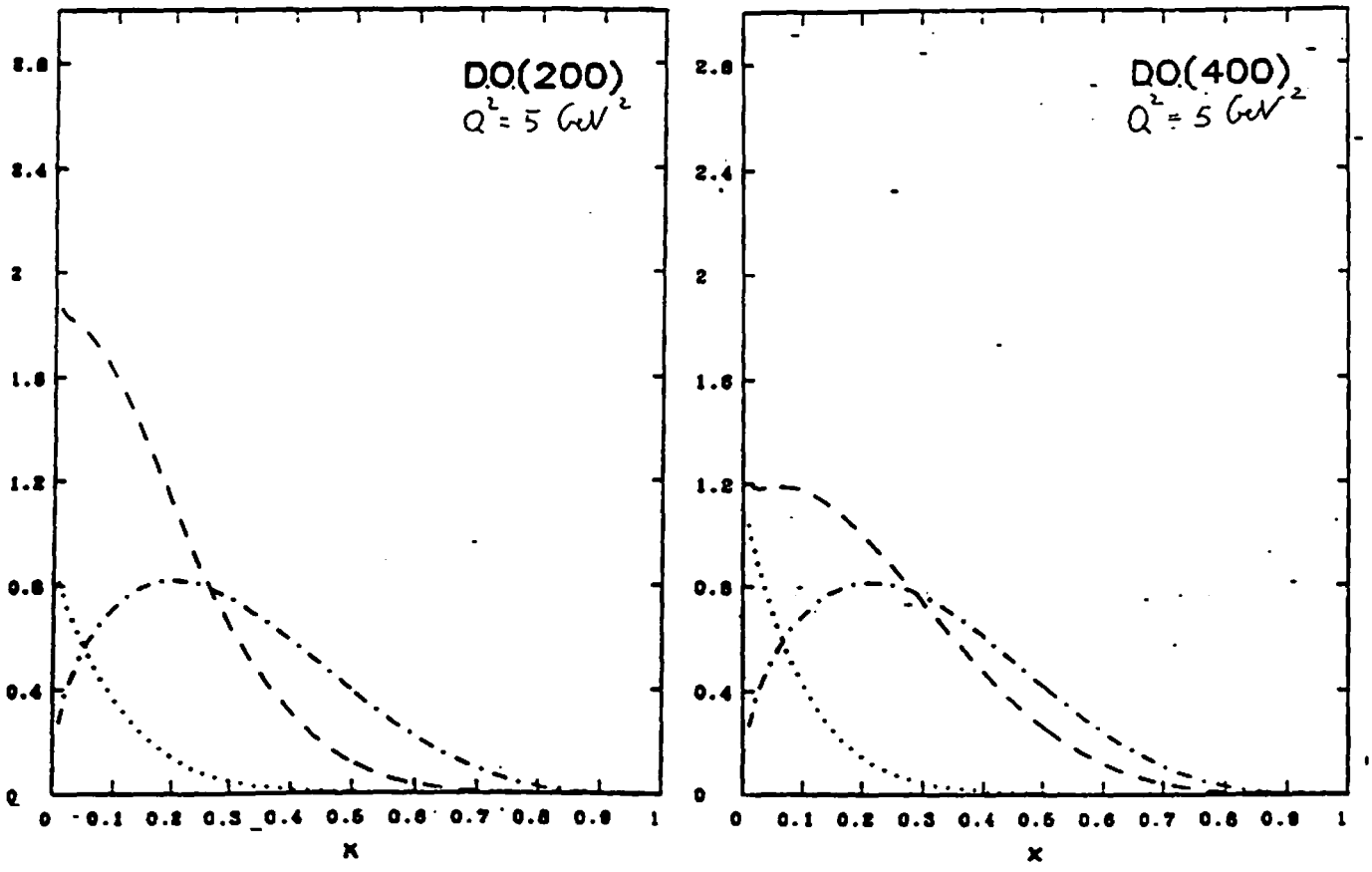

FIG 1.3 - Duke and Owens parametrization for gluon and quark structure functions. The two plots represent QCD calculations using a value of Λ (QCD scale) of 200 MeV (left) and 400 MeV (right) . The first value is the 'soft gluon parametrization', the second is the hard one. This can be sen by the functions in the graphs that represent gluon (dashed line), valence quarks (dashed-dotted line) and sea quarks (dotted line) distribution inside the proton [6] .

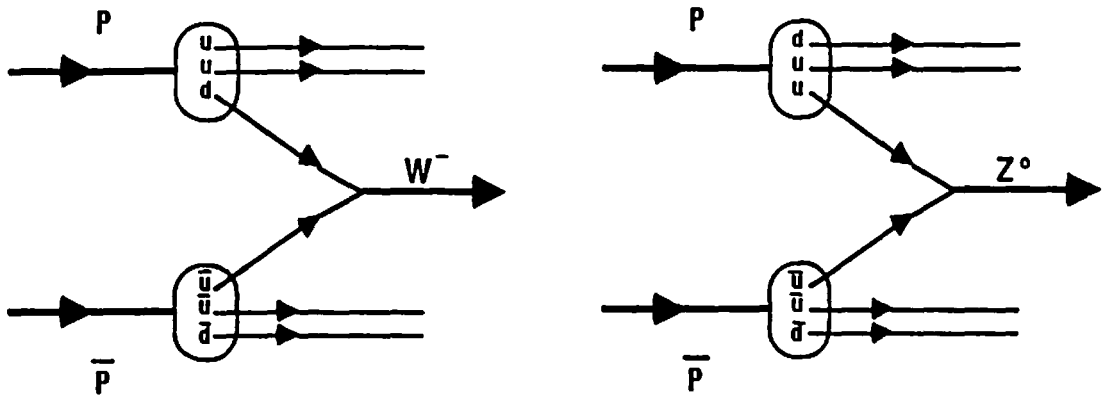

FIG 1.4 - Production of Intermediate Vector Bosons in $\bar{p}p$ collisions.

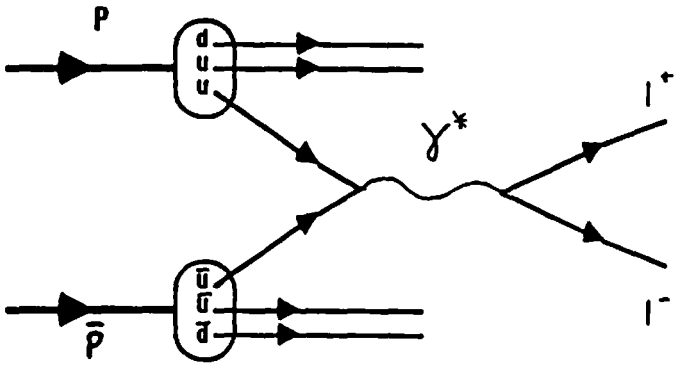

FIG 1.5 - $q\bar{q}$ electromagnetic interaction via Drell-Yan event.

rate, to a Z° or a $W^{\pm}$ (fig 1.4) .

- *Electromagnetic interactions* : a quark and an antiquark can also annihilate into a virtual (time-like) photon by electromagnetic interaction. This process was studied by Drell and Yan in 1970 [8] that proposed a simple parton

model for it (see fig 1.5) .

- *Strong interactions* : these are the most common and involve quarks, antiquarks and gluons . The pointlike basic interaction can be calculated and parametrized in functions of the three Mandelstam variables, referred to the elementary process :

$$s = (p_1 + p_2)^2 \qquad t = (p_1 - p_3)^2 \qquad u = (p_1 - p_4)^2$$

where p_i (i = 1,..,4) are the 4-momenta of the incoming and the outgoing particles as shown in fig 1.6 . *s* represents the square of the center of mass energy of the partons' system; *t* and *u* are related to the momentum trasferred from the incoming parton to the outgoing products. The differential cross section can be parametrized as :

$$\frac{d\sigma}{dt} = \alpha_s^2(Q^2)\frac{|M|^2}{s^2}$$

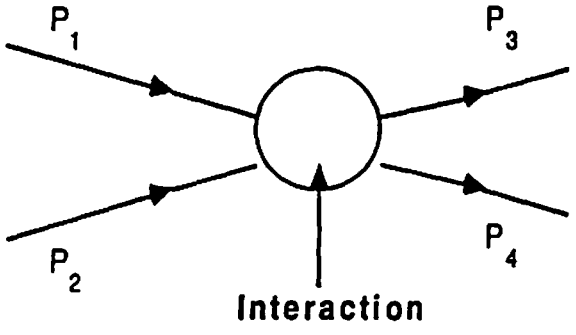

FIG 1.6 - The 4-momenta of the incoming and of the outgoing partons.

where |M| is the matrix element between the initial and the final state . It can be calculated for the elementary process and its values, calculated at first order, are reported in table 1.2 [6] . The last column in table 1.2 indicates the value for the cross section assuming $\theta^* = 90°$. We can note that the cross section for gluon scattering is much bigger than that for quarks. Provided gluons and quarks have the same distribution inside the nucleons, gluon interactions are the dominating QCD process. If we look at the

functions of fig 1.3 we see that gluon distribution inside the nucleon steeply falls to zero as we move to high values of x. For this gluon interactions are predominant at low x values, while, at high x values, quarks interactions are the dominating QCD effect. The momentum fraction carried by the parton, x, is connected to the center of mass energy s and to the momentum transferred, Q^2 by the relation :

$$Q^2 = x_1 x_2 s$$

Where x_1 and x_2 are the momentum fractions of the colliding partons.

From table 1.2 we can notice, also, that strong interactions can produce heavy quarks, like charm, beauty and, eventually, top . These quarks can be studied analyzing the products of their fragmentation, when they produce jets, or looking at the leptons produced by semileptonical decays like :

$$c \rightarrow s\,\mu^+\,\nu_\mu$$
$$b \rightarrow c\,e^-\bar{\nu}_e$$

In summary a nucleon collision can be temporally separated into three steps. We have the nucleons, characterized by their

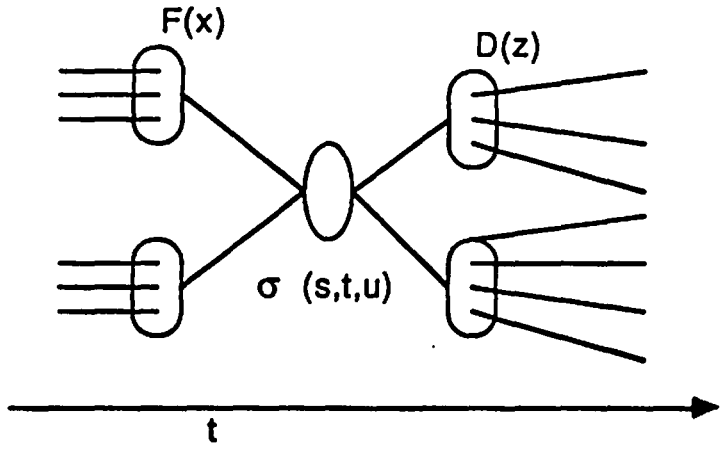

FIG 1.7 - The collision process is determined by the structure functions, F(x) ; the elementary scattering, σ (s,t,u) ; the fragmentation function, D(z) .

- *TABLE 1.2* - Matrix element expressed in terms of the Mandelstam variables. q^* is the center of mass scattering angle.

Elementary process	Matrix element $\|M\|^2$	Value at $q^*=90°$
$\bar{q}q \to \bar{q}q$	$\frac{4}{9}\left[\frac{t^2+u^2}{s^2}+\frac{s^2+u^2}{t^2}-\frac{2u^2}{3st}\right]$	2.57
$\bar{q}q \to gg$	$\frac{8}{3}(t^2+u^2)\left[\frac{1}{t^2}-\frac{4}{9su}\right]$	1.04
$\bar{q}q \to \bar{Q}Q$	$\frac{4}{9}\ \frac{t^2+u^2}{s^2}$	0.22
$gg \to \bar{q}q$	$\frac{4}{9}(t^2+u^2)\left[\frac{1}{t^2}-\frac{4}{9su}\right]$	0.16
$gq \to gq$	$(s^2+u^2)\left[\frac{1}{t^2}-\frac{4}{9su}\right]$	6.12
$gg \to gg$	$\frac{9}{2}\left[3-\frac{tu}{s^2}-\frac{st}{u^2}-\frac{us}{t^2}\right]$	30.4

structure functions expressed in terms of x ; we then have the scattering process, described by the Mandelstam variables; finally we have the outgoing partons that fragment according to some distributions parametrized by the variable z (fig 1.7) .

Besides all these standard processes, the high CM energy available allows the exploration of new energy regions. Thus non-standard physics can be probed at CDF .

1.4 - Natural coordinate system

The coordinate system used at CDF is specified in fig 1.8 .

The 'natural' coordinates for describing particle kinematics in hadron colliders are :

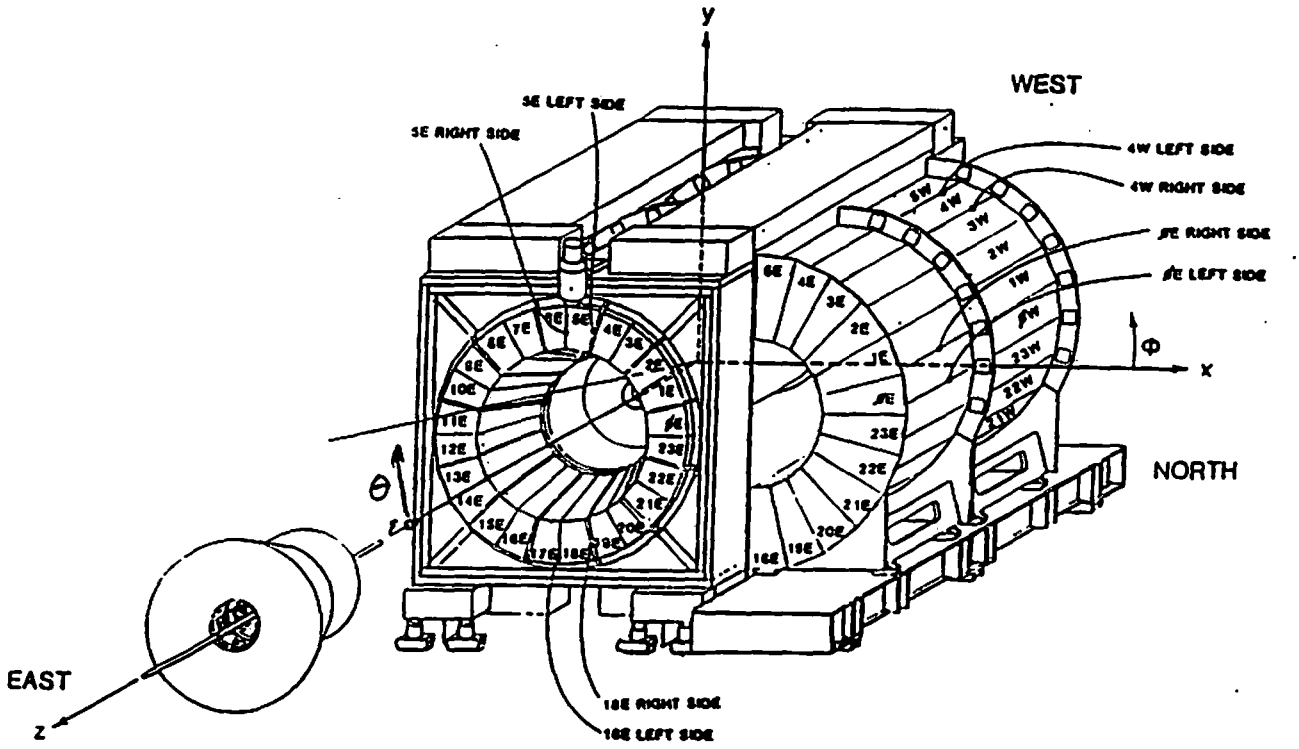

FIG 1.8 - CDF coordinate system.

$$\left(y = \log \frac{E + P_z}{E - P_z} \; ; \; \phi = \operatorname{arctg} \frac{P_y}{P_x} \; ; \; E_t = \sqrt{m^2 + P_x^2 + P_y^2} \right)$$

y is the 'rapidity' of the particle. It is Lorentz invariant for a boost in the z direction. It is additive, like the velocity at non relativistic energies. At energies large compared to the mass of the particles involved ($E \gg m \Rightarrow Pz = P\sin\theta \approx E\sin\theta$), a good approximation for the rapidity is the pseudorapidity η defined as :

$$\eta = -\log \tan\frac{\theta}{2}$$

Since η is directly related to θ, it is the variable normally used.

ϕ is the normal azimuthal angle defined in spherical and in cylindrical coordinates.

E_t is called the transverse energy. For energies much bigger than

the masses involved Et can be written as :

$$E_t = E \sin\theta$$

where θ is the polar angle of the position vector. The transverse energy is used because it is Lorentz invariant and because it is nearly equal to the 'transverse momentum' P_t. 'Transverse' means 'on the plane perpendicular to the beam pipe'. The transverse momentum is Lorentz invariant and it is globally conserved in the collision. The longitudinal momentum P_z is conserved, too. Nevertheless P_z is not a good variable first of all because the initial P_z is not 0, but it is an unknown quantity. In fact the center of mass of an elementary collision is not the laboratory system. The reason is that partons have a momentum fraction of the nucleon that is known just statistically (distribution function). The second problem is that some particles are diffracted at low angles and escape through the detector without being detected. Therefore P_z is not a useful variable.

2 LEPTOPHYSICS

2.1 - Introduction

Leptons are the final product of many of the fundamental processes discussed previously . With the exception of the τ-lepton, these particles have characteristic signatures, in our calorimeter, that allow their identification . Hard neutrinos (P_t>10GeV) can be identified using the asymmetry in the total transverse energy present in the calorimeter. In fact neutrinos escape the detector without any interaction . This leads to a momentum imbalance in the visible event .

Electrons are identified by their characteristic electromagetic shower.

Muons are identified as charged tracks passing through the calorimeter without interacting and leaving a track in the muon chamber (see 4.1 for a detailed description) .

In this chapter we will describe events yielding di-leptons as final products. In particular we will concentrate on dimuon events and on those processes that are detectable with our center of mass energy and our integrated luminosity.

2.2 - Drell-Yan events

A Drell-Yan [7] event (DY) consists in the annihilation of a quark-antiquark pair into a virtual (timelike) photon via an electromagnetic interaction. The photon can couple to a lepton pair (fig 2.1) . The differential cross section for the lowest order process, $p\bar{p} \rightarrow l^+l^-$, is :

$$\frac{d\sigma}{dQ^2} = \frac{4\pi}{3}\alpha^2\frac{1}{Q^4}F(\tau) .$$

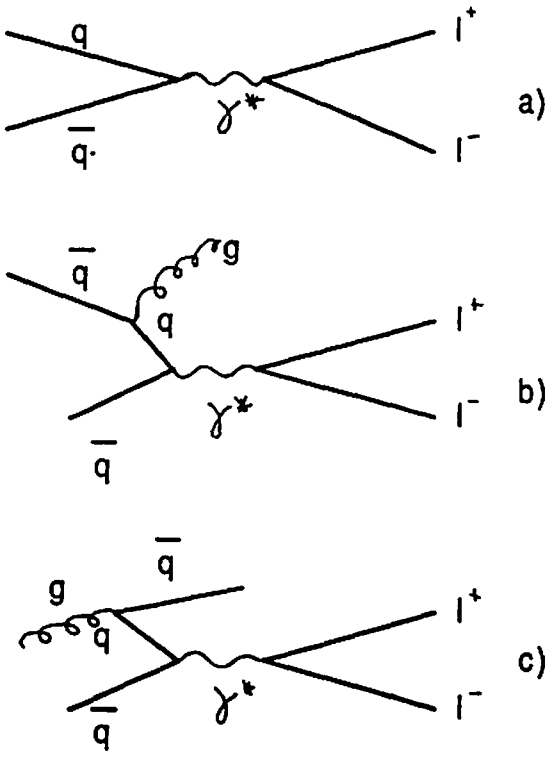

FIG 2.1 - Drell-Yan process and higher order corrections.

a) 'Standard' process

b) 'Annihilation' diagram

c) 'Compton' diagram

where :

α = fine structure constant = 1/137
Q^2 = total squared 4-momentum
$F(\tau)$ = scaling function
τ = Q^2/s

The scaling function $F(\tau)$ is simply the squared charge of every quark of the proton, weighted by its 'density' in the proton itself . Thus it can be parametrized as [8] :

$$F(\tau) = \sum_i e_i^2 \frac{1}{N_c} \int_0^1 x_i\, dx_i \int_0^1 \bar{x}_i\, d\bar{x}_i\; f_i(x_i)\, \bar{f}_i(\bar{x}_i)\; \delta(x_i \bar{x}_i - \tau) \quad .$$

where *i* runs over the flavours present in the proton; *e* is their charge; N_c is the number of colours; *x* is the fractional moment and *f(x)* is the structure function for quarks or antiquarks (these last

indicated with an overbar) . The δ-function assures the 4-momentum conservation of the process .

The squared 4-momentum exchanged between partons is equal to the mass of the intermediate photon and to the mass *m* of the lepton pair. Thus the differential cross section can be written as :

$$\frac{d\sigma}{dm} = \frac{8\pi}{3}\alpha^2 \frac{1}{m^3} F(\tau) \ .$$

If there are scaling violation effects $F(\tau)$ has to be replaced by $F(\tau,Q^2)$.

The signature for this process is a pair of isolated leptons, plus hadrons from the underlying event .

This simple picture has to be modified taking into account higher order QCD processes as shown in fig. 2.1b , 2.1c . These processes can yield additional (soft) jets in the event and they are responsible, at Tevatron energies, for ≈30% of the events tagged as Drell-Yan [9].

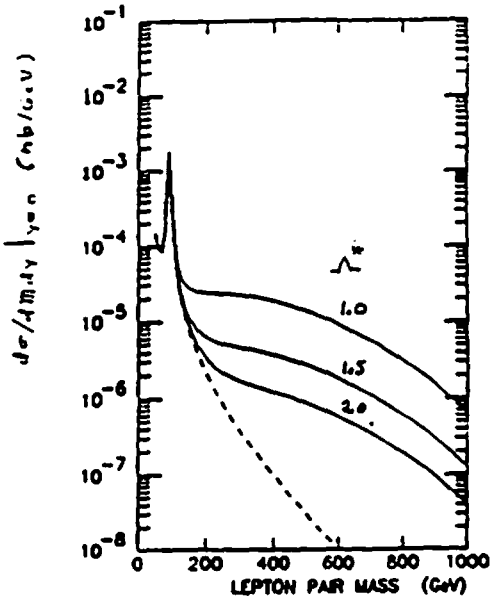

FIG 2.2 - Drell-Yan theoretical cross section. At high energies we start probing an (eventual) quark compositness. The values associated with every line are the lower limits we can set to the compositness energy scale, given experimental results consistent with the line itself.

Studying Drell-Yan events it is possible, also, to set limits on quark and lepton compositeness. In fact quark-antiquark cross section varies when we reach the energy scale at which we are probing an eventual compositeness. Fig 2.2 shows the theoretical cross section of Drell Yan events at high energies [10] . The different curves show the limits that we can set to the scale of energy at which quark compositness is probed. As we can see the integrated luminosity needed for seeing these effects is of the order of 10^3 inverse picobarns. Next run will provide 1 inverse picobarn of integrated luminosity, so such effects won't be visible.

2.3 - J/Ψ,Υ states

J/Ψ and Υ are resonant quark states formed by the heavy quarks charm (c) and beauty (b) . They were observed for the first time in 1974 and in 1977, respectively [11] .

As we already mentioned (cfr 1.1) quarks are spin=1/2 fermions. In analogy to positronium bound states of quark and antiquark are called *quarkonia* . At small distances (<1fm) the relative potential can be parametrized as a Coulomb like potential

$$V(r) \approx -\frac{\alpha}{r} . \quad (r < 1\text{fm})$$

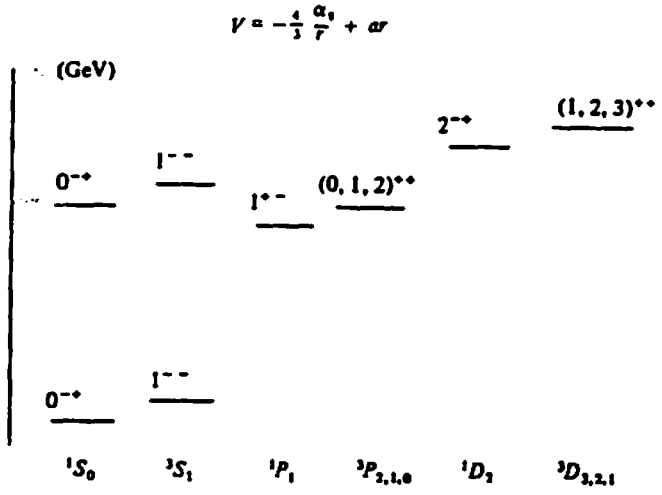

FIG 2.3 - $Q\bar{Q}$ levels assuming the Cornell potential (2.1) [15] . *W* is the energy of the level.

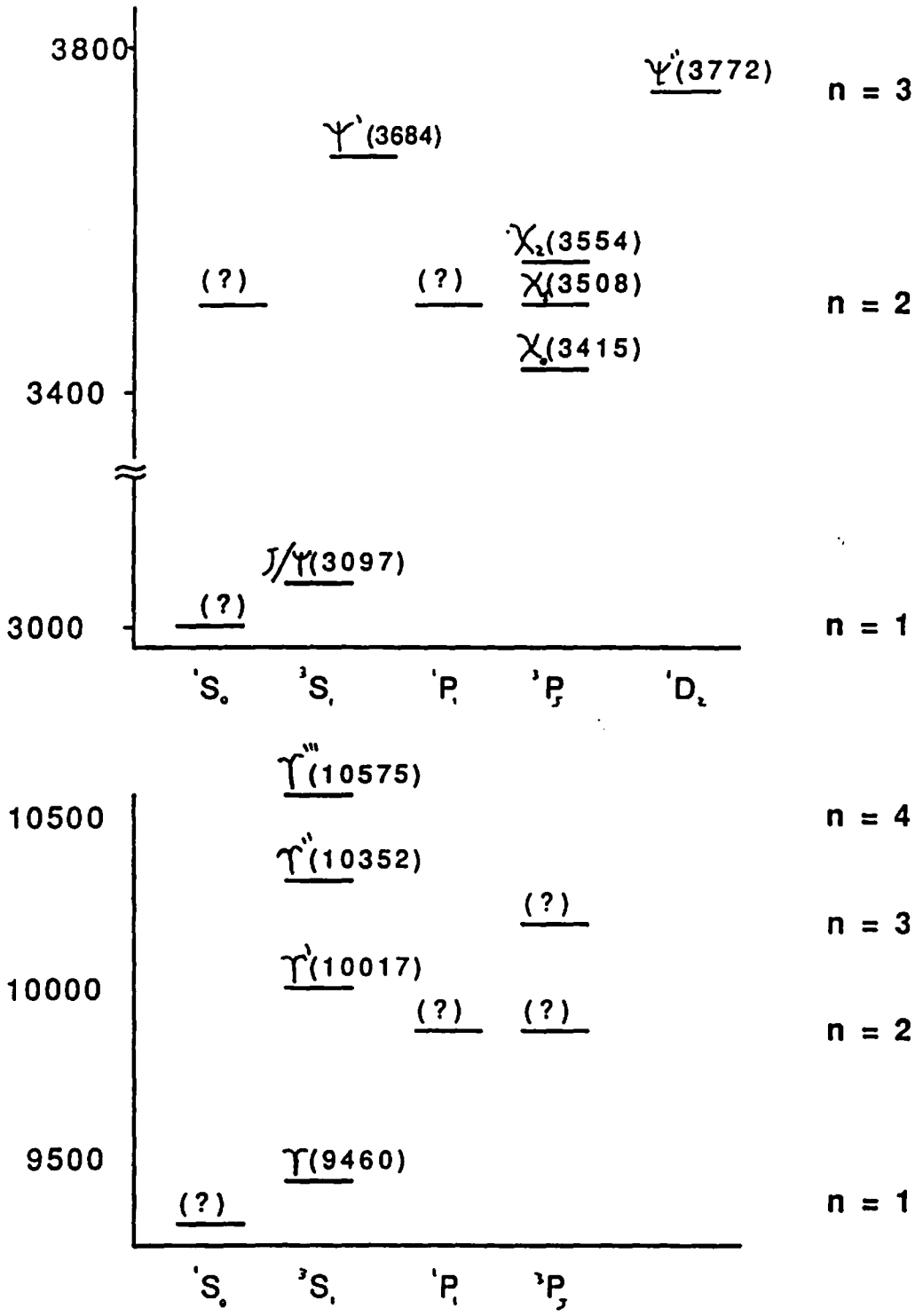

FIG 2.4 - Results of heavy flavour spectroscopy for charmonium and bottomium. The values are from [12] and [13] .

At large distances (>1fm) the potential is confining. For the 'long distance' potential there are several models [14], all well explaining the data at small distances where perturbation theory can be used . Using the 'Cornell potential' :

$$V(r) = \frac{4}{3}\frac{\alpha(Q^2)}{r} + ar \qquad (2.1)$$

the energy levels of $Q\bar{Q}$ states can be calculated. Fig 2.3 shows the theoretical values computed with (2.1) [15]. In fig 2.4 the observed states are represented . Theory is consistent with experiment.

The dimuon decay Branching Ratios (BR) for the $^3S_1$ states, the J/Ψ and the Υ family, are 7% and 3% respectively . Therefore J/Ψ and Υ states can be tagged by the observation of a muon pair. We can understand the topology of the di-lepton pairs by analysing J/Ψ production. There are two basically different kind of processes yielding J/Ψ states :

• *direct production of $c\bar{c}$ states* : A $q\bar{q}$ or qg or gg fusion can produce a $c\bar{c}$ state as shown in fig 2.5a . Generally the produced states are χ_i states that decay in a J/Ψ with a photon.

$$q\bar{q} \text{ or } gg \rightarrow g\chi_i \rightarrow g\,\gamma\,J/\Psi$$
$$qg \rightarrow q\chi_i \rightarrow q\,\gamma\,J/\Psi$$

χ_i is the $3P_i$ state of the charmonium. Direct J/Ψ production is suppressed by c-parity conservation. In fact both gluons and J/Ψ have **c**=-1. For this reason a J/Ψ needs to exchange an odd number of gluons with the initial state. But the exchange of one single gluon is forbidden because both the initial and final state are colourless. A three gluon exchange is needed.

The c parity of the $3P_i$ states is, on the contrary, **c**=+1, due to angular momentum. Therefore only two gluons are needed and the direct J/Ψ production is suppressed a factor α_s compared to direct χ production (the factor is given by the extra gluon) .

FIG 2.5 - Mechanisms for the J/ production :

A) Direct $c\bar{c}$ production

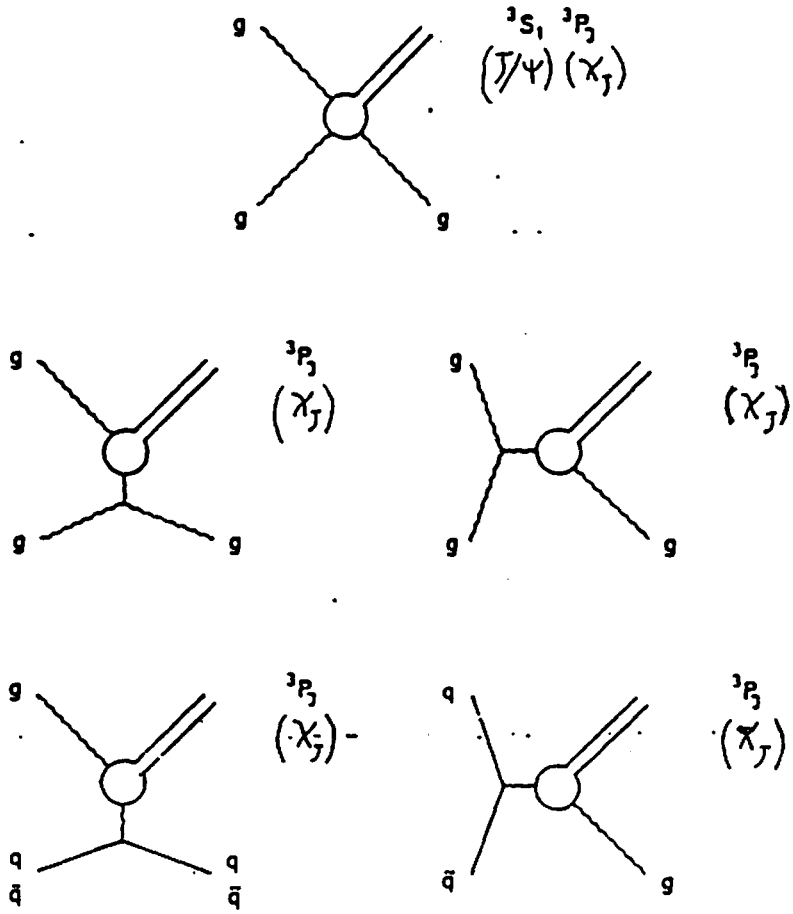

B) Indirect $c\bar{c}$ production

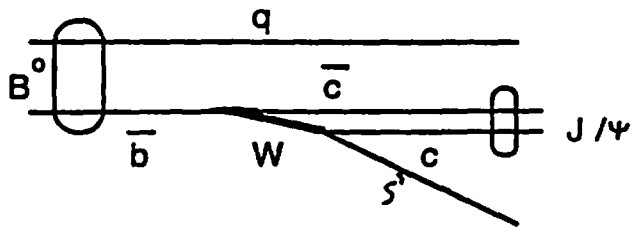

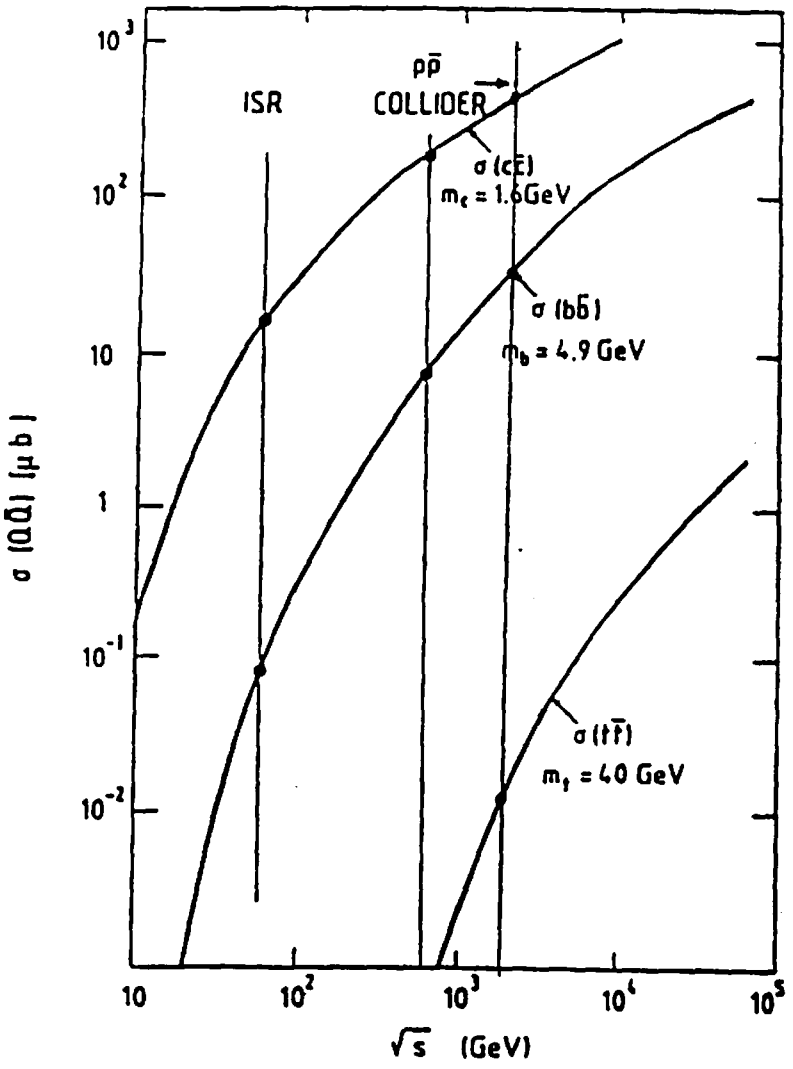

FIG 2.6 - Cross section for heavy flavour production. The three lines compare ISR, UA1 (UA2) and CDF center of mass energies.
Isajet results using lowest order contribution only (m_{top}= 40 GeV) [16] .

the dimuon channel. Such events can be sketched as follows :

$$p\bar{p} \rightarrow b\bar{b} \begin{cases} \rightarrow \bar{c}\,\mu^{+}\nu_{\mu} \\ \rightarrow c\,\mu^{-}\bar{\nu}_{\mu} \end{cases}$$

The c-quark produced in a b semileptonic decay can, in turn, undergo a semileptonic decay . Such a process will yield multimuon events. For example 3-muon events can be produced with a BR of 0.1 % . Like sign muons can also be produced. These cascade processes are shown in the 'fish bone' diagram of fig 2.7 .

From these diagrams, muons are expected to be at large relative angles, if they come from opposite 'branches' of the process, or at small relative angles, if they come from the same 'cascade'.

The topology of the event is a pair of isolated muons with a soft jet on the opposite side and, eventually, some electromagnetic activity generated by the photon.

• *indirect production* : a J/Ψ state can also be produced by a B-meson (BR = 1.2%) [24]. The B-meson's decay to a J/Ψ state is well described in the *spectator model* . In this model the b quark of the meson decays to a c quark emitting a virtual W. The W couples to a fermion doublet as shown in fig 2.5b . The model is called spectator model because the second quark of the meson doesn't take part to the reaction. Radiative corrections have to be taken into account to have the correct behaviour.

In the B° decay other hadrons are produced together with the J/Ψ. Mostly just a K (≈18%) or a Kπ pair(≈ 50%) is produced in the process. [24].

The cross section for quarkonium production can be calculated on the basis of the strong interaction potentials (cfr 1.2) . For example Barger and Martin [18] evaluated the cross section at √s=1800 GeV to be :

$$\sigma(p\bar{p}\to J/\Psi) * BR(J/\Psi\to\mu^+\mu^-) = 11\mu b * 0.07 = 770\ nb$$
$$\sigma(p\bar{p}\to \Upsilon) * BR(\Upsilon\to\mu^+\mu^-) = 2\mu b * 0.03 = 60\ nb$$

2.4 - Heavy flavour production

An important source of prompt dimuons is the associated production of a heavy quark and its anti quark (c, b, t(?)) by strong interactions, followed by semileptonic decay. The cross section for heavy flavour production is shown in fig 2.6 as a function of the center of mass energy √s . The BR for the semileptonic decay

$$Q \to q\mu\nu_\mu$$

is about 10% . Thus about 1% of the $b\bar{b}$ pair produced will decay in

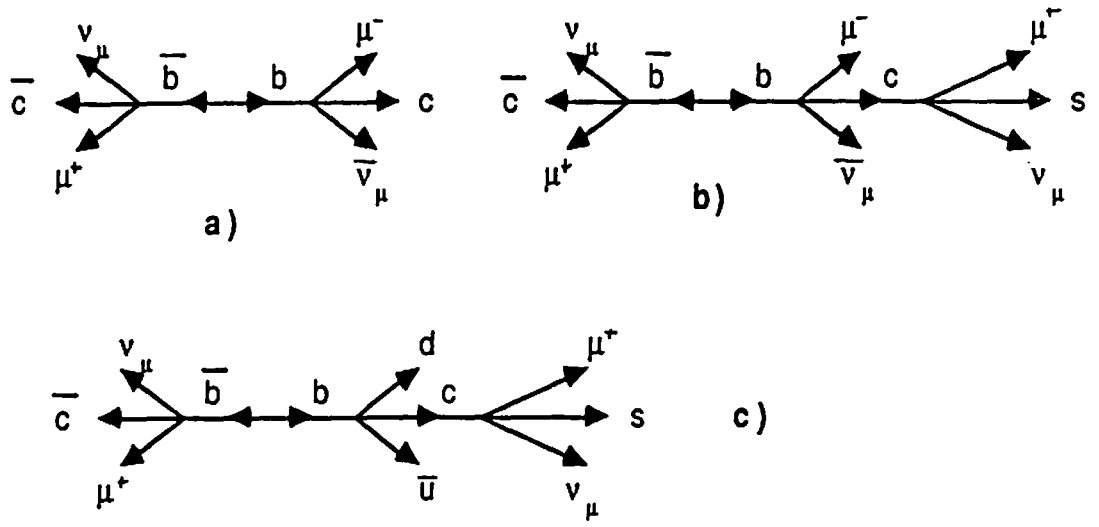

FIG 2.7 - Multimuon events from $b\bar{b}$ production :
a) unlike sign event
b) multimuon event
c) like sign event
In $c\bar{c}$ production, just diagram a) is possible.

This simple picture has to be modified taking into account higher order QCD processes. These processes contribute to the cross section and give rise to additional jets that can change the topology of the event. In fact these jets are generally far from the muons and from the fragments of the heavy quark. An example is shown in fig 2.8 ('gluon splitting') [16]. The heavy quark can thus acquire a large transverse momentum which forces the muons not to be back to back.

The cross section for the production of heavy quark pairs followed by di-muon decay can be estimated from fig 2.6 as [16] :

$$\sigma(p\bar{p} \rightarrow b\bar{b}\,X) * BR(b\bar{b} \rightarrow \mu^+\mu^-\,X) = 27\,\mu b * 1\% = 0.27\,\mu b$$

$$\sigma(p\bar{p} \rightarrow c\bar{c}\,X) * BR(c\bar{c} \rightarrow \mu^+\mu^-\,X) = 150\,\mu b * 1\% = 1.5\,\mu b$$

FIG 2.8 - Higher order corrections to heavy flavours production.
a) Fusion process plus initial state radiation
b) Splitting of an outgoing muon
The dashed boxes indicate the 2 -> 2 processes.

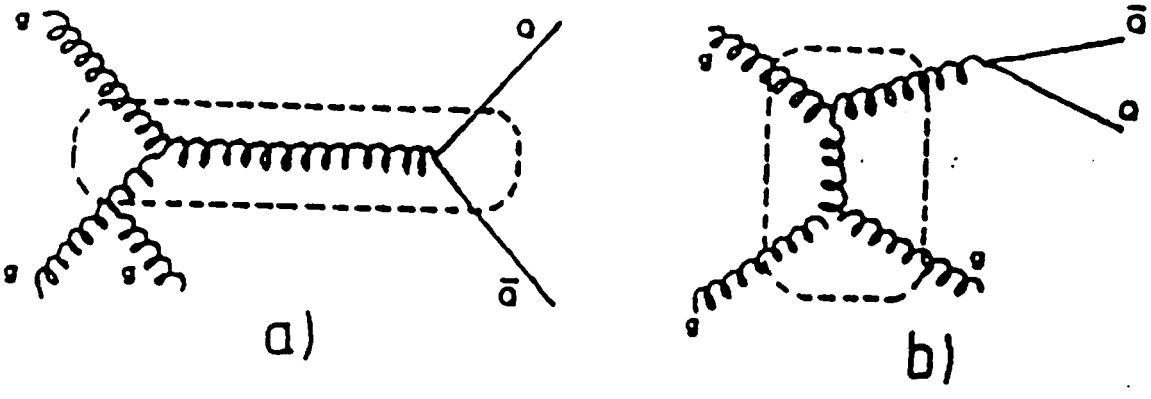

2.5 - B^0-$\bar{B}^0$ mixing

A B^0 meson can give, as a decay product, a muon by semileptonic decay of the b-quark. If a B^0 and a $\bar{B}^0$ are simultaneously produced both of them can decay semileptonically yielding dimuons as final states. The two muons produced in these processes will have different sign. If, for any reason, the B^0 meson oscillates into a $\bar{B}^0$, or viceversa, then the two final muons will have the same sign. If the rate of oscillation is comparable to the like sign muon production by second generation decay (see previous section), than the effect can be detected experimentally at our collider.

The reason for an oscillation between two B^0 states is that weak interactions need not conserve flavour quantum number. Therefore boxed diagrams like the one showed in fig 2.9 are possible.

Until now the only visible mixing has been the mixing between K^0 and $\bar{K}^0$. The reason is that the lifetime of the K-meson is

comparable to the oscillation period . On the other hand the decay of D° mesons is Cabibbo favoured, resulting in a short lifetime. Therefore no mixing has been observed in the D°-$\overline{D°}$ system. Recent measurements [17] show that the B°-mesons have a relatively long lifetime and that oscillations are possible.

Limits on B° oscillations have been set by e^+e^- experiments (CLEO [18] , ARGUS [17]) where B°$\overline{B°}$ pairs where obtained by the decay of the Y(4s) state. In $p\overline{p}$ colliders B°-mesons are obtained by the association of a b-quark with an s-quark (BR=40%) or a d-quark (BR=20%) [19]. The technique used to detect if there are oscillations between the two states is to look at the number of like sign muon pair produced. If this number is bigger than the value expected only taking into account second generation decays, than we observe the effect of a mixing between B-mesons . Using this technique UA1 has been able to set limits on the mixing between the two states [16] . With the results of 1988-1989 run this goal will be achievable also at CDF. The luminosity integrated in 1987 run is not high enough to allow for such an analysis.

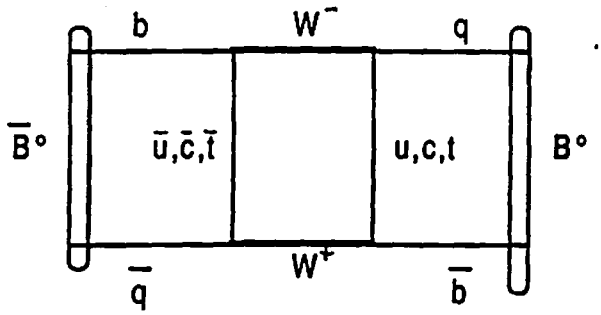

FIG 2.9 - Possible diagram for $\overline{B°}$-B° mixing. The top channel is favoured by K-M coupling.

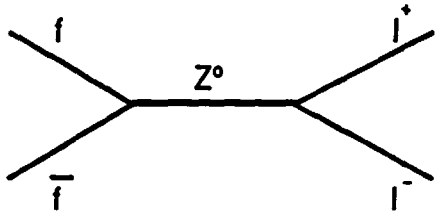

FIG 2.10 - Z° production and decay in a lepton pair. This process led to the discovery of the neutral boson [29] .

2.6 - Z° decays

As we already mentioned, Z° induces neutral currents. The part of the Lagrangian for Neutral Weak Leptonic Interactions is:

$$L_{nwli} = \sqrt{2} M_{Z^\circ} \left(\frac{G}{\sqrt{2}}\right) \Sigma_f \bar{f} \gamma_\mu (V_f - A_f \gamma_5) f \; Z^\mu \; .$$

where :

G = Fermi costant = $1.17 * 10^{-5}$ GeV^{-2}
f = fermion family (leptons or quarks)
V_f = vector coupling = $2 Q_f \sin^2 \theta_W - 1/2$
Q_f = absolute charge of the fermion 'f'
A_f = axial coupling = -1/2

We note that, for charged leptons, the vectorial coupling V_f is very small, being $Q_f = 1$ and $\sin^2 \theta_W = 0.23$. The decay width $\Gamma_{f\bar{f}}$ is proportional to the sum of the axial and vectorial coupling squared, that is :

$$\Gamma(f\bar{f}) \propto V_f^2 + A_f^2 \; .$$

For this reason the dilepton channel has the smallest BR among the possible Z° decay modes :

$$BR(Z^\circ \rightarrow e^+e^-) = BR(Z^\circ \rightarrow \mu^+\mu^-) = 3\%$$

On the other hand the signature for this decay mode is very clear (fig 2.10) : two opposite charged leptons, back to back in the r-ϕ plane and with very high momentum (Pt > 20 GeV for muons in the central region). The rest of the event is generally very quiet, just underlying event in which energies and momenta involved are small in comparison to the leptons . The theoretical cross section at Tevatron energies is :

$$\sigma(p\bar{p} \rightarrow Z^{\circ}) = 60\,nb$$

$$\sigma(p\bar{p} \rightarrow Z^{\circ} \rightarrow \mu^{+}\mu^{-}) = 3\% * 60\,nb = 0.18\,nb$$

The same cross section is expected in the electron channel. Most of the Z° will decay into hadrons, but this signal is overwhelmed by QCD background.

3 - THE EXPERIMENTAL SETUP .

3.1 - The detector

The collider detector at CDF is a 4π steradians detector built to study $p\bar{p}$ interactions at a center of mass energy of 1800 GeV and at a luminosity of 10^{30} $cm^{-2}sec^{-1}$. It consists of a central detector and a forward backward system. A perspective view is given in fig 3.1 .

The detector is composed of tracking chambers, surrounding the beam pipe, electromagnetic and hadronic calorimeters, segmented in towers pointing to the nominal vertex of interactions, and, in some regions, also muon coverage. The muon coverage is given by two separate sets of drift chambers covering the central ($50° < \theta < 140°$) and the forward region ($4° < \theta < 16°$, $164° < \theta < 176°$).

In this thesis we will use only the results of the Central Muon System because the Forward one had trigger problems and so it had to be severely prescaled. For this just a brief description of the backward-forward calorimeter will be given, while more emphasis will be put on the parts of the detector directly connected to the reconstruction or to the analysis of muon events.

CDF calorimetry uses both scintillators and gas chambers. Proportional chambers cover the polar angle $2°<\theta<30°$ – $150°<\theta<178°$, while scintillators are used to detect particles in the central region.

The central detector consists of a Central Tracking System located inside the superconducting solenoidal coil. The coil provides a magnetic field of 1.5 Tesla oriented along the incident beam direction. The return path for the magnetic field is provided by a steel yoke that is used also as support of the detector itself. The magnetic field is used by the Central Tracking Chamber to measure the transverse momentum P_t of every particle by its bending in

the*FIG 3.1* - General view of CDF detector.

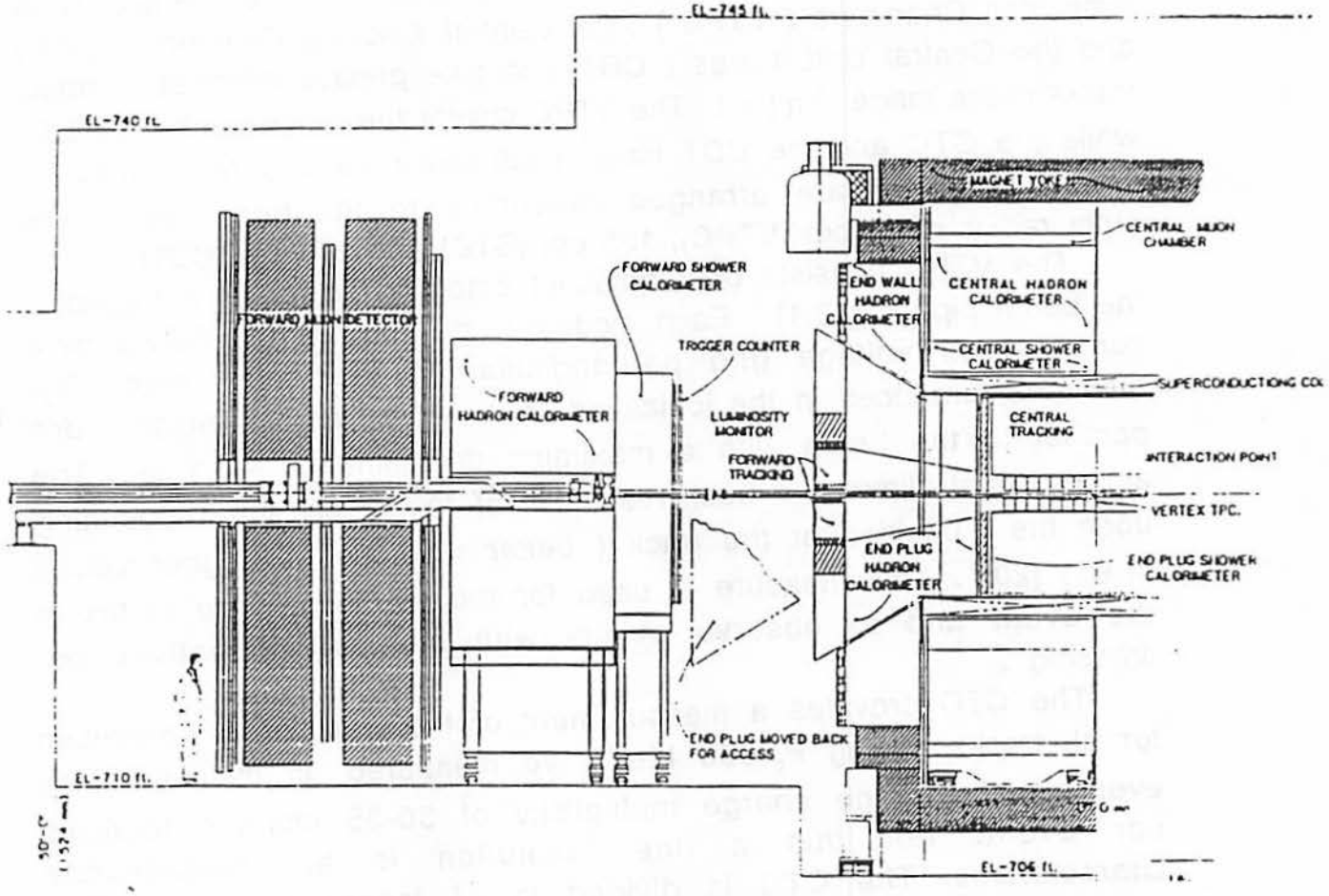

central region .

The parts of the detector used in our muon analysis are : the Central Tracking System, the Central Calorimetry and the Central Muon Chambers.

3.2 - The tracking system

The goals of the CDF tracking system are complementary to the calorimetry. While calorimetry integrates over particle energies the

tracking system gives information for every particle measuring its trajectory and its momentum by the bending in the 1.5 Tesla magnetic field. The CTC includes the work of the Vertex Time Projection Chambers (VTPC) , the Central Tracking Chamber (CTC) and the Central Drift Tubes (CDT) to give precise information about tracks in the range $|\eta| < 1$. The VTPC covers the range $-3.5 < \eta < 3.5$, while the CTC and the CDT have a full coverage only for $|\eta| < 1$. These detectors are arranged concentric to the beam pipe, with outer radius of 30 cm (VTPC), 135 cm (CTC) and 140 cm (CDT).

The VTPC consists of 8 adjacent octogonal modules surrounding the beam pipe (fig 3.1) . Each module is divided into two halves by a central high voltage grid perpendicular to the beam pipe. The electrons, produced in the ionization of the 50–50 argone ethane, drift parallel to the beam with a maximum drift time of ≈ 3.3 μs . The anode signal allows a z track resolution of 400 to 1000 μm depending upon the θ position of the track (better resolution at higher values of θ) [20] . This measure is used for reconstructing the vertex of the event and to observe events with multiple interactions per crossing .

The CTC provides a measurement of the transverse momentum for all tracks having P_t>300 MeV. We measured, in minimum bias events, an average charge multiplicity of 30-35 charged particles per event. For this a fine resolution is an indispensible characteristic. The CTC is divided in 84 layers of sense wires arranged in nine concentric 'superlayers' (fig 3.2) . The drift cells are tilted to form an angle of 45° with a radial line. This has two advantages: first of all cells can overlay, in the radial direction, so that every particle will cross at least two of them in every superlayer; secondly this arrangement, together with the effect of the Lorentz force, makes the trajectory approximately parallel to the cell.

Five of them have wires parallel to the beam giving a reconstruction of the track in the r-ϕ plane (perpendicular to the beam) . For reconstructing a track, adjacent hit points are fit to arcs of circumference, in the r-ϕ plane. The distances of the hits from the

FIG 3.2 - x-y section of the CTC. The nine concentric superlayers reconstruct a track both in the transverse plane (layers 1-3-5-7-9) and in the beam plane (layers 2-4-6-8). It is also visible the 45° bending of the drift cells studied to compensate the effect of the Lorentz force (see text).

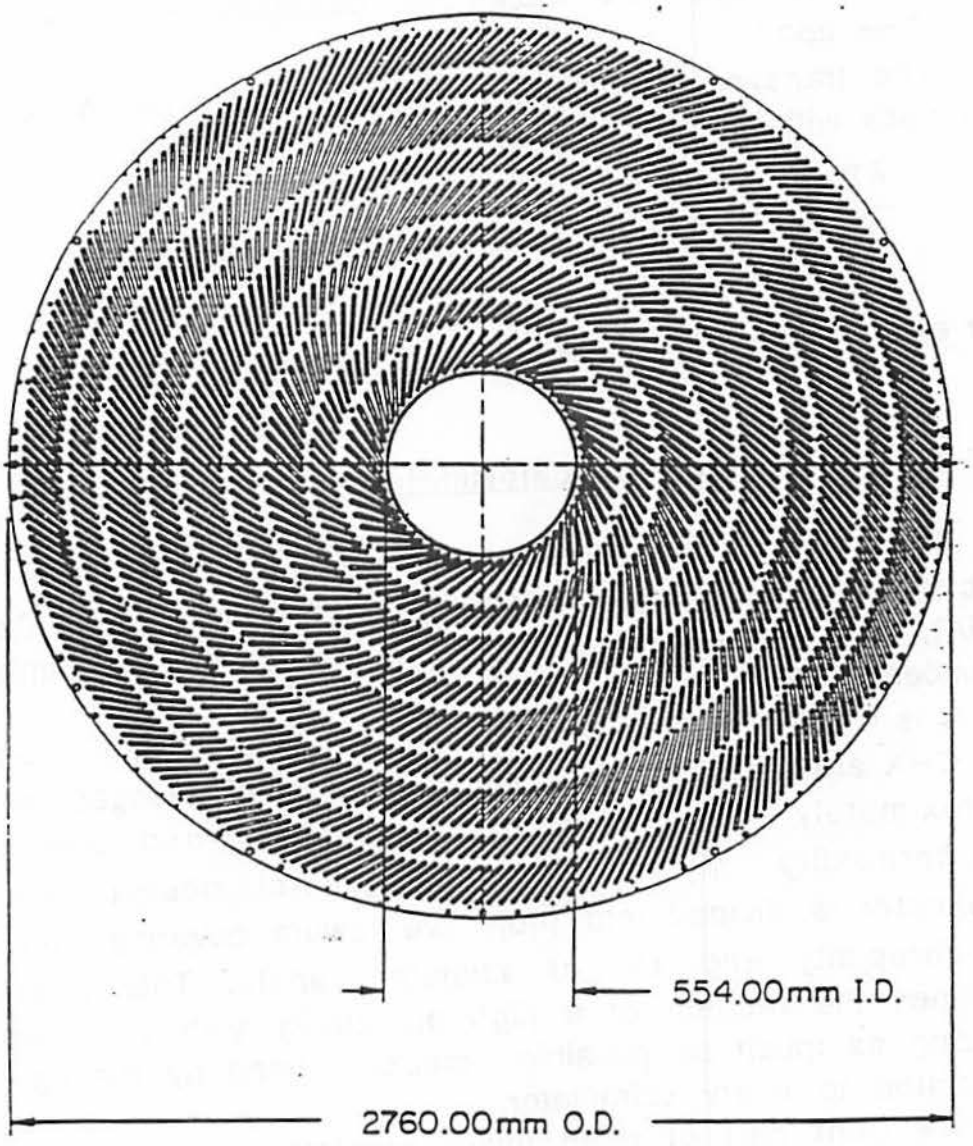

fitted arc are called 'residuals' . Apposite studies [21] show a gaussian distribution for these residuals having a FWHM of 440 μm . That is ≈ 65% of the hits are < 220 μm apart from the reconstructed track. The sense wires of the other four layers are inclined, with respect to the beam line, by +3° and −3° alternatively. The tracks are reconstructed in the r-z plane with a resolution of ±4mm .

In every layer two tracks are distinguished if they are more than 3mm apart.

The transverse momentum is calculated from the curvature of the track with a resolution :

$$\frac{\delta P_t}{P_t} = 0.003 * P_t \qquad (\text{in GeV})$$

For example a 40 GeV track is measured with a precision of ±4 GeV .

3.3 - The central calorimeter

The central calorimeter is composed of the Central Electromagnetic Calorimeter (CEM), the Central Hadron Calorimeter (CHA), the Wall Hadron Calorimeter (WHA) and the Central Muon Chambers (CMU) (fig 3.3) .

It is divided in two symmetric halves at the plane $z = 0$. CEM and CHA are organized into 24 modules, called 'Wedges', subtending approximately 15° of azimuthal angle ϕ and one unity of pseudorapidity η. Following the general design, the central calorimeter is divided into projective towers covering 0.1 units of pseudorapidity and 15° of azimuthal angle. This segmentation combines the request of a high granularity with the necessity of reducing as much as possible cracks caused by the light guides associated to every scintillator.

The front part of each tower consists of an electromagnetic calorimeter (CEM). In the CEM 32 planes of scintillators are alternated with ≈ 4 mm thick lead layers, giving a total of 20

radiation lengths. Electromagnetic showers are, thus, well segmented, in the direction perpendicular to the shower itself and well contained in the CEM. The energy resolution obtained in test beam measurements is measured at the testbeam as :

$$\frac{\sigma_E}{E} = \frac{13.5\ \%}{\sqrt{E \sin\theta}} \cdot$$

Additional information are given by Strip Chambers inserted in the CEM parallel to the scintillators and in the depth corresponding to the maximum shower development (≈ 6 radiation lenghts) . These chambers determine the position by the charge deposited on a net of ortogonal strips and wires . The resolution is momentum dependent varying from 3 mm at $P_t = 10$ GeV to 2 mm at $P_t = 50$ GeV .

The hadronic part is divided, by technical constraints, into Cenrtal Hadron Calorimeter (CHA) and End Wall Hadron Calorimeter (WHA). Their geometry is studied to fit with the projective tower design of CEM. One centimeter thick scintillators are alternated with 5 cm and 2.5 cm steel layers, in the CHA and in the WHA respectively, for a total depth of ≈ 5 absorbtion lenghts. The energy resolution is about :

$$\frac{\sigma_E}{E} = \frac{70\ \%}{\sqrt{E}} \cdot$$

where E is the energy expressed in GeV.

The central calorimeter provides an energy mapping for every event. The granularity is well matched for studying jets. The energy distribution inside a tower can be obtained by looking at the difference in the charge collected by the two phototubes set at the ϕ edge of every tower. In fig 3.4 the light guides and the phototubes position is showed for CHA. This information is used, in example, in the calculation of the centroid of jets.

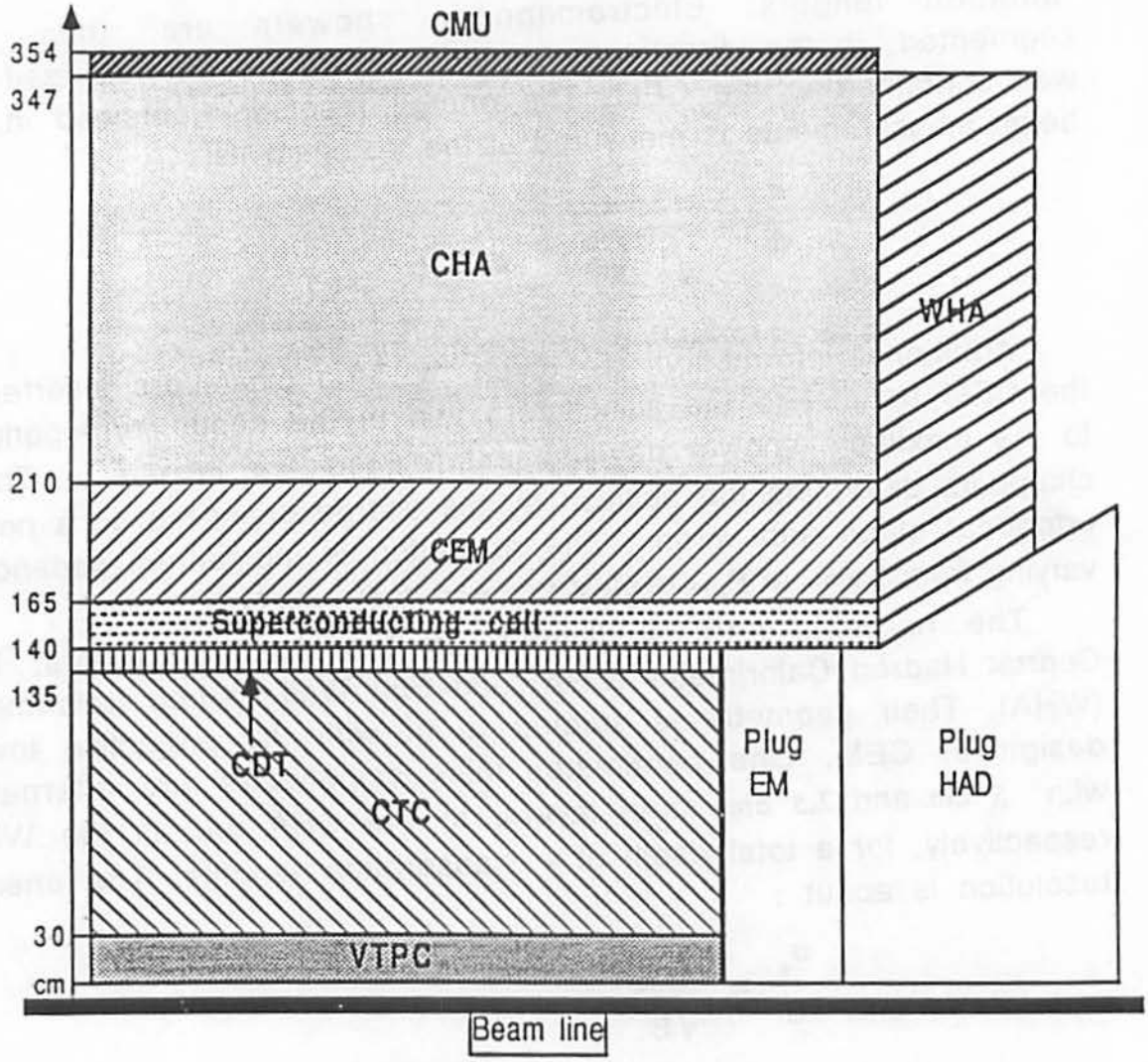

FIG 3.3 - View of the central calorimeter. The plug system use gas calorimeters and it's not considered part of the central.

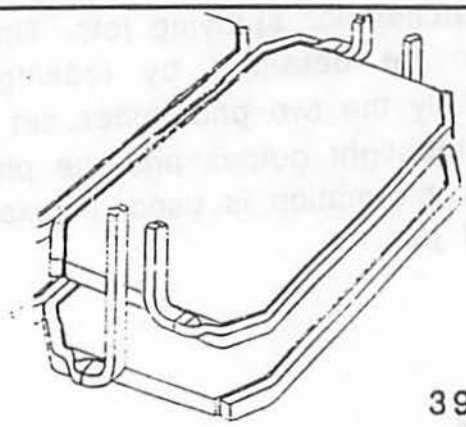

FIG 3.4 - Two layers of a Central Hadron tower. The lateral light guides allow a determination of the center of mass of the energy released in the tower.

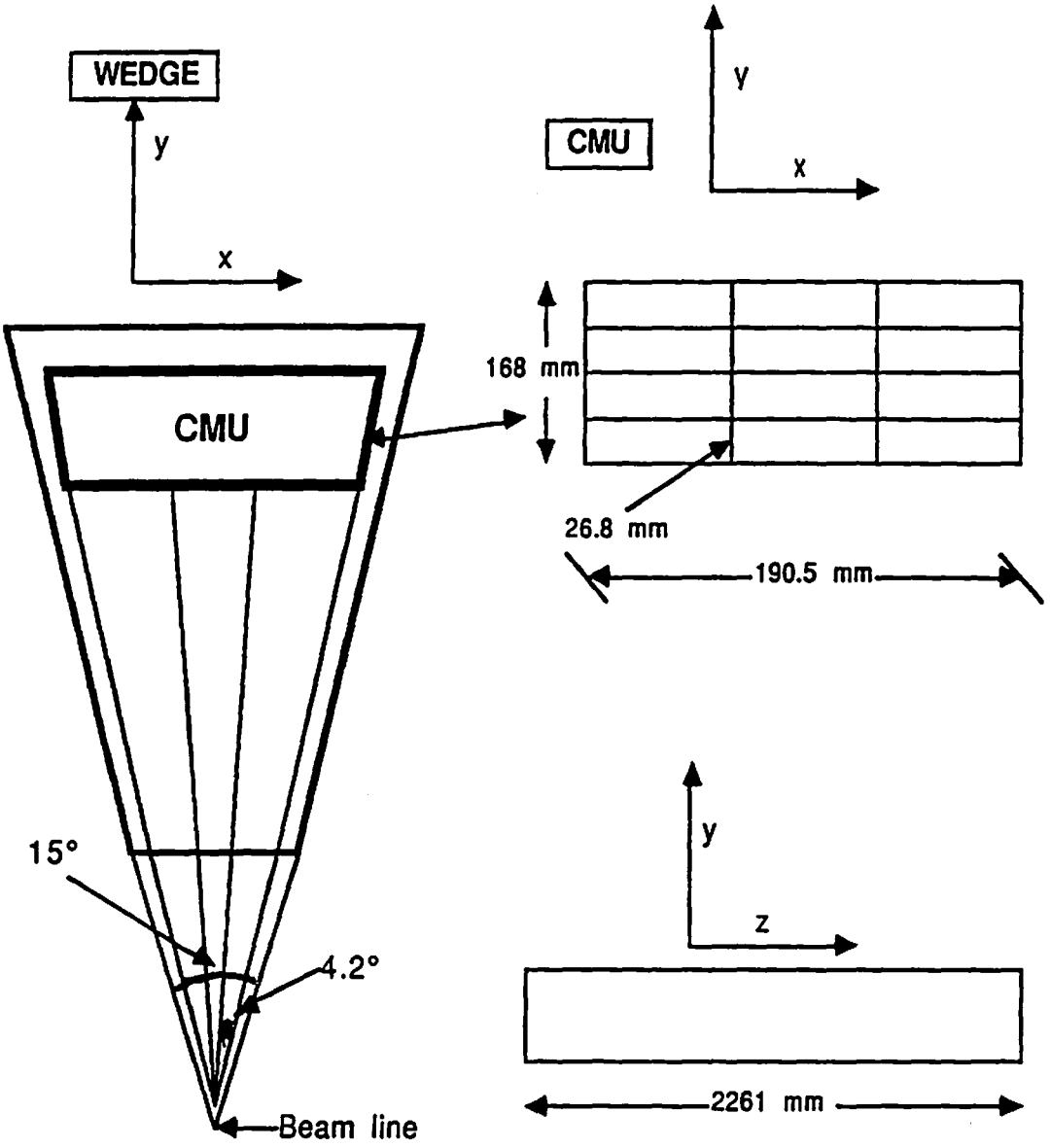

FIG 3.5 - Muon chambers located at the outer radius of the wedge. One tower covers 1.05° in phi and 0.65 in eta .

3.4 - The central muon detector .

The Central Muon Detector (CMU) is located at the outer radius of the central hadron detector. It is composed of detectors covering 12.6° in ϕ and 0.65 units in η . The muons detectors are located into the top of every wedge (fig 3.5) .

Every chamber is divided into three modules, each of them subtending 4.2° in ϕ . A module consists in 4 layers of 4 rectangular drift cells having 50 μm thick stainless steel sense wires parallel to the beam direction. The dimensions of a typical drift cell are : 63.5 mm wide × 26.8 mm high × 2261 mm long (fig 3.5) . For technical convenience the sense wires of two drift cells are connected together at the side with the smallest η . The first cell of a module is connected to the third the second to the fourth. Four sense wires, one from each layer, form a muon tower. Two of the four sense wires, from alternating layers, lie on a radial line. The other two are 2 mm far from a radial line. In this way the left right ambiguity is solved by looking at which pair of wires was hit first.

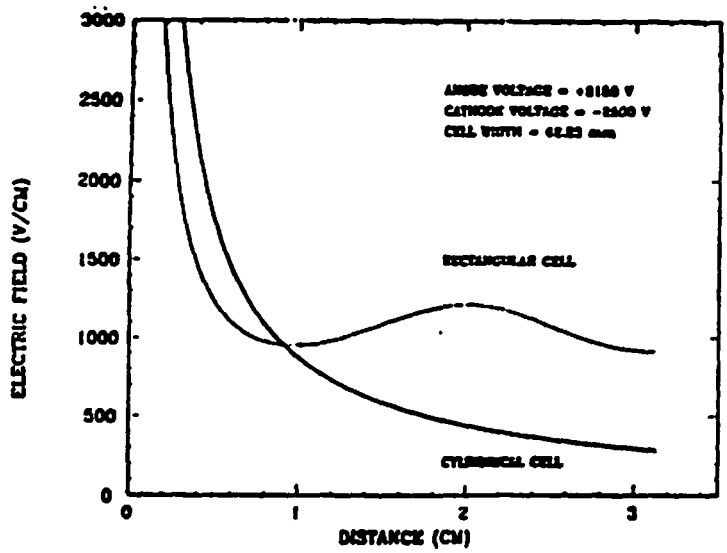

FIG 3.6 - Intensity of the electric field in function of the distance from the sense wire. The electric field is compared to that generated by a cell having perfect cylindrical symmetry.

The ϕ coordinate of the track is measured by the time needed by the electrons to drift in a 49.6% - 49.6% - 0.8% mixture of argon-ethane-ethanol . With a voltage of +3150 V on the sense wire and of -2500 V on the cathode pads, the electric field varies, as a function of the distance from the sense wire, as shown in fig 3.6 . We can see that it is approximately constant inside the cell. The accuracy reached in determining the ϕ position is :

$$R\,\delta\phi = 250\,\mu m$$

where R is the distance of the sense wire from the beam pipe .

The z position is measured by the charge deposited at each end of the sense wire . If L is the length of a drift cell, Q_0 is the charge released by a charged particle in a point of coordinate z in the cell 1, than the charge collected at the end of cells 1 and 3 is (fig 3.7) :

$$Q_1 = \frac{Q_0}{2}\left(1+\frac{z}{L}\right) \qquad (3.5.1)$$

$$Q_3 = \frac{Q_0}{2}\left(1-\frac{z}{L}\right)$$

Thus the ratio :

$$R = \frac{Q_1 - Q_3}{Q_1 + Q_3} = \frac{z}{L}$$

linearly depends upon the position z . Indeed we have to take into account the charge decay at the capacitors set at the end of the wire. If $\tau = C R_{wire}$ is the decay time and t is the time needed to collect the signal, than equation (3.5.1) has to be modified as :

$$Q_1 = \frac{Q_0}{2}\left(1+\frac{z}{L}e^{-t/\tau}\right)$$

$$Q_3 = \frac{Q_0}{2}\left(1-\frac{z}{L}e^{-t/\tau}\right)$$

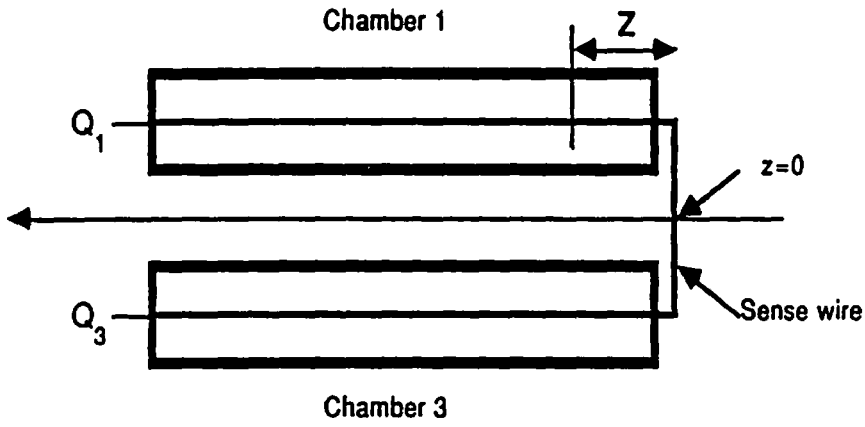

FIG 3.7 - A sense wire connects chamber 1 and 3 of a same layer. The position 'Z' of a charged track can be expressed in terms of the charge Q_1 and Q_3 measured by the cells.

The relation :

$$R = \frac{z}{L} \quad \Rightarrow \quad z = LR$$

still holds, but small differences in the value of the decay time τ, caused by differences in C or in the resistence R_{wire} between the two drift cells, change it into :

$$z = \alpha LR + \beta$$

with α and β to be determined empirically by a careful calibration of each module.

This method gives a measurement of *z* with a precision :

$$\delta z = 4\,\text{mm}$$

Four hits in a tower are then the signature that a charged particle crossed the central detector and traversed the muon chambers. If at least three hits are presents a segment called 'stub'

is reconstructed. If this stub corresonds to a track reconstructed by the CTC, then the track is labelled a 'muon' (cfr section 4.1 for a detailed description) .

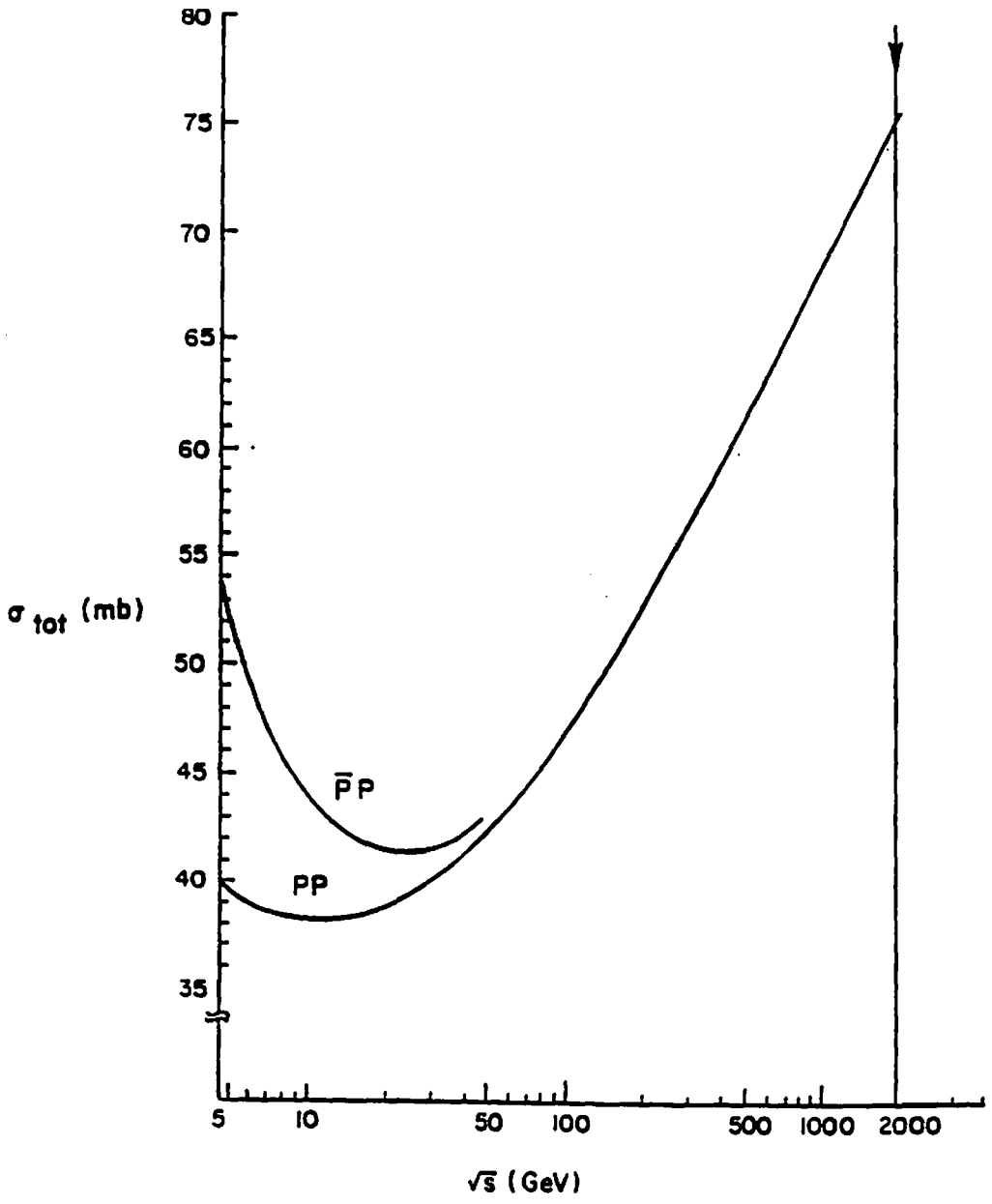

FIG 3.8 - Total hadronic cross section in function of the center of mass energy.

3.5 - The trigger

At $\sqrt{s}$=1800GeV the total hadronic cross section predicted for pp collisions is (fig 3.8) [22] :

$$\sigma = 80\,\text{mb}$$

Thus, at the present luminosity of :

$$L = 10^{30}\,\text{cm}^{-2}\,\text{sec}^{-1} = 1\ \mu\text{b}^{-1}\,\text{sec}^{-1}$$

the rate of events per second is of the order of :

$$N\left(\frac{ev}{sec}\right) = 80\,\text{mb} * 1\mu\text{b}^{-1}\text{sec}^{-1} = 80 * 10^{3}\,\text{sec}^{-1} = 80\ \text{Kh}$$

A typical event has a length of approximately 200–300 Kbytes. The rate of writing to tape events of such a length cannot exceed 1-2 hertz . Thus the trigger has to reduce the number of accepted events a factor of 80000 ! The rate of interesting physical events is, on the other hand, just a small fraction of the total rate. Therefore the trigger must be capable, in a very short time, of deciding what events have to be rejected with a high efficiency in accepting interesting events. It must be flexible, because of the many sources of physical events that can become more or less important depending upon the results of the experiment. For this reason the trigger is projected to work at different levels of decision with a different timing at each level.

In 1987 run only level 1 was operating.

• *Level 1* : level one trigger has a decision time of 7 μs , the time between one beam crossing and the following. The trigger is segmented in an uniform 24×42 array in the ϕ–η plane. Each section corresponds to 15° in ϕ and 0.2 units in η . Therefore two towers in the central or six towers in the gas calorimeter make up a trigger tower. The transverse energy measured by every trigger tower is compared to a 1 GeV E_t threshold. Then the towers of every

calorimeter are summed together and accepted if they reach a fixed value. There are four independent Summing Circuits (*summers*) which can operate with different single tower thesholds and total thresholds . Summer 1 triggers on the total transverse energy; summer 2 and 3 on the electromagnetic energy for central and plug+forward calorimeters, respectively.

Summer 4 collects Minimum Bias events. These events are triggered by the coincidence of two *Beam-Beam Counters* , one east and one west. The Beam-Beam counters are scintillators placed in front of the forward calorimeter. In fig 3.1 they are nominated *trigger counters* .

Besides these triggers there are muon triggers for the Forward and for the Central Muon Chambers. As already said Forward Muon calorimeters had severe trigger problems, that caused a prescaling of a factor of 100.

The Central Muon trigger will be described in next section.

3.6 - The Central Muon trigger

A central muon is reconstructed combining the information given by the Central Tracking Chamber (CTC) and the Central Muon Chamber (CMU).

A segment, or *stub* , is reconstructed by the CMU whenever three out of four layers in a tower have hits. Information about hits are sent to the *muon matchbox* . It compares the hits with some fixed *roads* , or hit patterns, and it decides whether or not to accept the stub.

In the CTC the Central Fast Tracking (CFT) makes a fast reconstruction of tracks above a P_t of 2.5 GeV.

The CFT is a hardware module built for allowing a quick ($\approx 1\mu s$) connection of the hits detected by the CTC into two dimensional tracks. The CFT uses the r-ϕ information given by the axial wires of the CTC. At each beam crossing a coincidence is applied to the fast out data ot the axial sense wires. The fast out data are *time over threshold* signals. A coincidence defines a prompt hit. Whenever a

prompt hit is detected in the outer layer, the CFT looks for hit patterns. In fact a particle of a fixed momentum will describe a fixed trajectory. In the CFT 32 trajectories are memorized, starting from each sense wire of the outer layer and reaching the sense wires of the inner layer .

Fig 3.9 shows a typical road that the hardware will recognize as a high P_t track. After each beam crossing a list with all the found tracks is transmitted to the muon matchbox. Whenever a stub is found either in the wedge the track pointed at, or in one of the two adjacent wedges, a muon trigger is set.

No di-muon trigger was present in 1987 run.

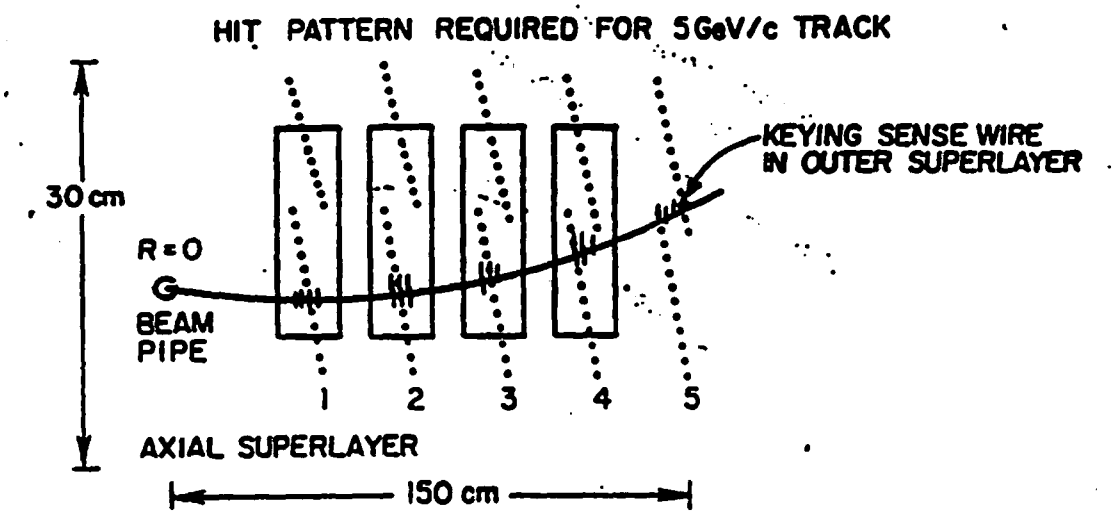

FIG 3.9 - Hit pattern recognized by the CFT as a track. The scale is set to show the track curvature.

4 - DATA PROCESSING

4.1 - Offline reconstruction

In the offline processing more time is available, for this a full track reconstruction and a more accurate track-stub matching are possible. In this chapter we analyse the steps done to arrive at our final sample.

CTC tracks are reconstructed fitting arcs of helicies to the hits detected by the drift cells. If a charged particle has a transverse momentum smaller than 350 MeV it will not reach the calorimeter, because it gets curled up in the magnetic field. If a particle having $P_t > 350$ MeV does not interact in the central calorimeter, the particle will follow the path sketched in fig 4.1a . The angle α between the trajectory and a radial line depends upon the bending angle of the magnetic field β as follows :

$$D \sin\alpha = L \sin(\beta/2) \qquad 4.1.1$$

β, on its turn, depends upon the particle momentum in the r-ϕ plane, P_t, in the following way :

$$\sin(\beta/2) = \frac{eLB}{2cP_t} \qquad 4.1.2$$

Combining equations 4.1.1 and 4.1.2 we obtain α in function of P_t :

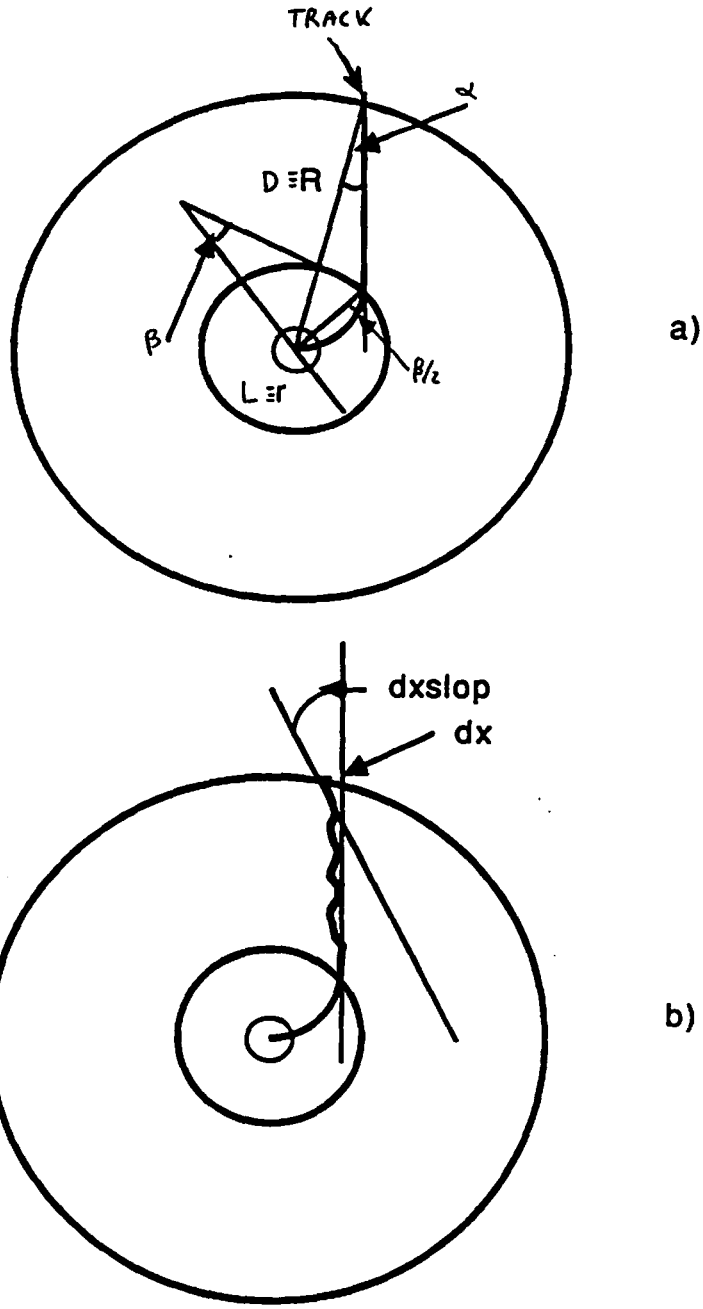

FIG 4.1 - Projection on the x-y plane of the path followed by a charged particle without (a) and with (b) multiple scattering . The bending in the magnetic field is accentuated.

$$\alpha \approx \sin\alpha = \frac{L}{D}\sin(\beta/2) = \frac{eL^2B}{2cDP_t}$$

The value of α obtained has to be corrected by the residual magnetic field present inside the calorimeter. In fig 4.2 the equipotential lines of CDF central magnetic field are represented [23] . The magnetic field varies radially and it has a mean value of 1 KGauss . The muon algorithm uses, for calculating the correction on the value of α, a constant magnetic field of 1 KGauss. Extrapolating in this way we obtain a value of the position P and the slope α at the face of the muon chambers for the r-ϕ plane. An analog procedure, made easier by the absence of the magnetic field, is carried on in the r-z plane. At the end we are left with four variables: position and slope of the extrapolated track in the r-ϕ and in the r-z plane.

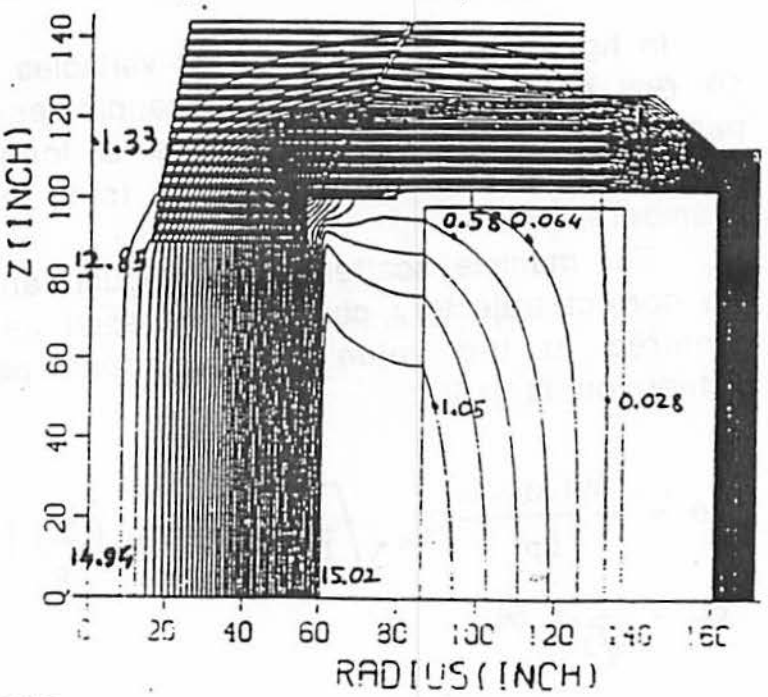

FIG 4.2 - Equipotential lines of the magnetic field. The residual field inside the calorimeter has an average intensity of 1 KGauss.

4.2 - Matching cuts

A real particle does not follow the ideal path we have sketched. Hadrons are predominantly contained in the ≈ 5 absorbtion lengths of the calorimeter (cfr ch.5) . τ mesons decay within a few millimeters,

generally into hadrons. Electrons are contained inside the electromagnetic calorimeter. Muons, on the contrary, are very penetrating particles and punch through the central detector, emerging at the muon chambers. However they undergo multiple scattering. So the path followed is irregular and the muon will emerge from the calorimeter in a different position and with a different slope with respect to the extrapolation of the CTC track (see fig 4.1b) . We can define the following *matching variables* :

- *dx* = difference in the r-ϕ plane ($\equiv$ x-y plane) between the CTC extrapolated track and the muon stub
- *dz* = same quantity measured in the r-z plane
- *dxslop* = difference between the slope of the CTC track ('α' in fig 4.2a) and the slope of the muon stub in the transverse plane
- *dzslop* = same quantity measured in the r-z plane

In fig 4.3a-d these matching variables are plotted for one of the six raw tapes containing muon candidates. All the distributions are peaked at zero and they have a long tail owing to random coincidences between a central track and a hit in the muon chambers.

For multiple scattering the angular and spatial deviations from the correct trajectory can be expressed as a Gaussian distribution, centered at the value of the 'ideal' path. The width of this distribution is [15] :

$$\delta\theta = \frac{14.1\ \mathrm{MeV/c}}{\beta p} Z_{inc} \sqrt{\frac{L}{L_R}} \left[1 + \frac{1}{9} \log_{10}\left(\frac{L}{L_R}\right) \right] \quad \text{(Radians)}$$

$$\delta L = \frac{1}{\sqrt{3}} L\ \delta\theta$$

where :

p = particle momentum

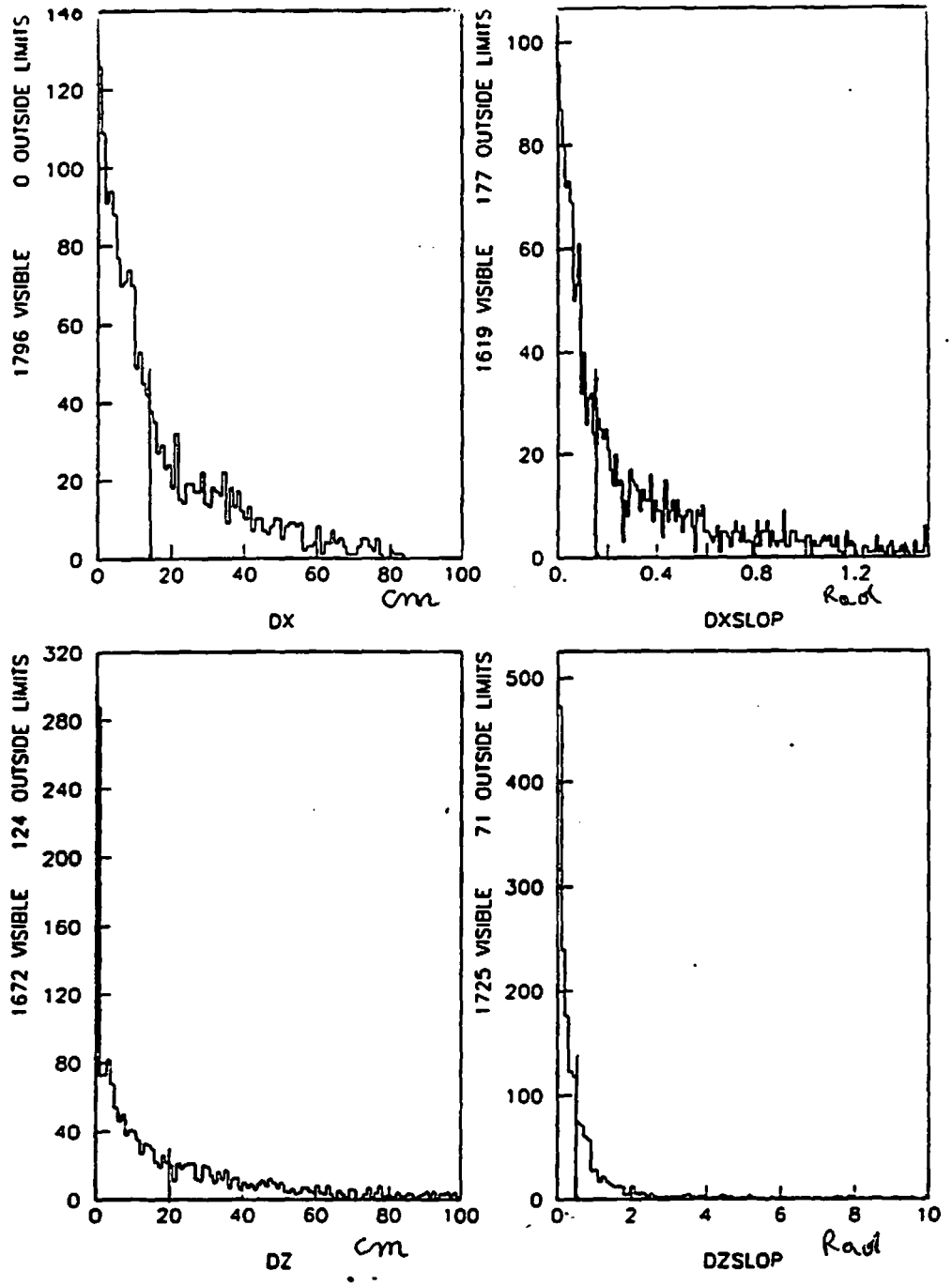

FIG 4.3 - Matching variables between CMU stubs and CTC tracks extrapolated without any interaction in the detector. a) and b) represent distance and angle between stub and track in r-f plane. c) and d) are the same variables in the r-z plane. The peaks at 0 in c) and d) are due to tracks not reconstructed by the stereo layers of the CTC .

Z_{inc} = charge of the incident particle in units of 'e'
L = length of the crossed material
L_R = radation length of the crossed material

The central detector consists of 20 radiation lenghts in the electromagnetic calorimeter and 85 radiation lengths in the hadron calorimeter. Substituting these values we obtain :

$$\delta\theta = \frac{0.17}{p} \text{ rad}$$

$$\delta L = \frac{21}{p} \text{ cm}$$

Dividing by $\sqrt{2}$ we have the average deviations in the r-ϕ and in the r-z plane :

$$\delta\theta_{r\phi} = \delta\theta_{rz} = \frac{0.12}{p} \text{ rad}$$

$$\delta L_{r\phi} = \delta L_{rz} = \frac{15}{p} \text{ cm}$$

We, thus, apply a cut at the following values :

dx $\leq$ 15 cm
dxslop $\leq$ 0.12 rad
dz $\leq$ 20 cm
dzslop $\leq$ 0.5 rad

Our cut on muon P_t is at 1.5 GeV (see later). This means that we are cutting, in the worst case, at 1.5 σ of the matching variables in the r-ϕ plane. In the r-z plane our cut is looser because of the low precision both in the CTC and in the CMU measurement of the z coordinate. Fig 4.3 show the cuts we have applied.

In the 4500 multi-stub events selected by the raw data there are 9462 candidate muons. Applying the matching cuts we reject 7430 of them. We, then, accept events having at least two muon

candidates and we are left with :

275 Dimuon events
3 Trimuon events

In fig 4.4 we can see how the muon candidates from these events are distributed in the $\eta-\phi$ plane. The limits of the CMU chambers ($|\eta| \leq 0.7$) are cleary visible. There is also a band at $\phi \approx 90°$ having less hits. The reason for this is that the upper chambers of the muon detector had to work at low voltage because of problems caused by the Main Ring. The Main Ring, in fact, goes through the detector a few meters above the Tevatron. Energy coming from the Main Ring caused a continuous tripping of the chambers.

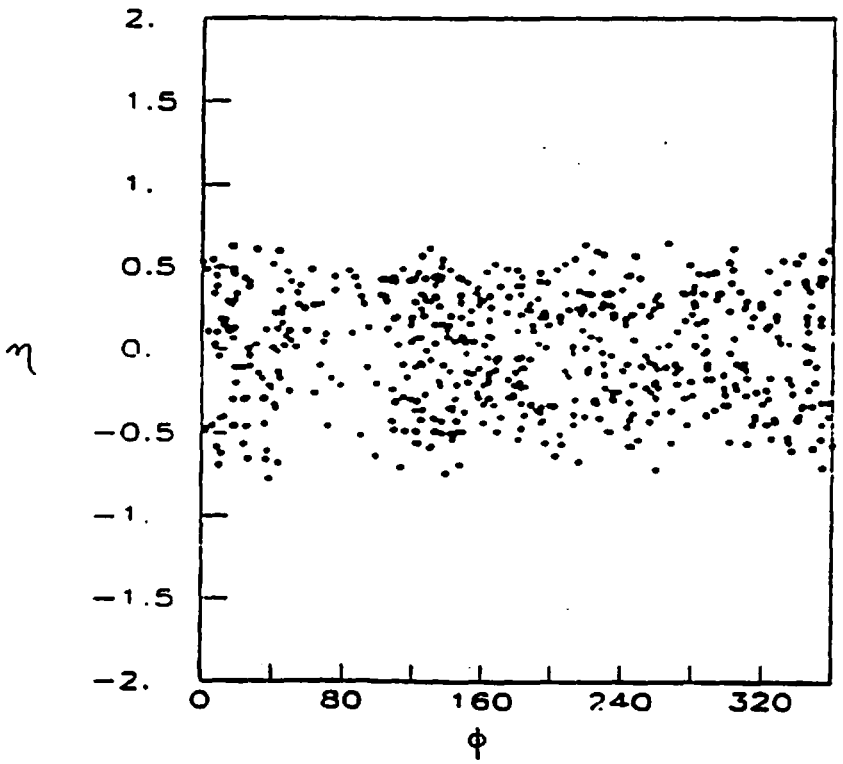

FIG 4.4 - $\eta-\phi$ distribution of our dimuon candidates. The muon chambers cover the polar region $|\eta| < 0.7$ units of rapidity. The empty band at $\phi = 90°$ is due to Main Ring problems (see text).

FIG 4.5 - Pt distribution of muons in dimuon events passing the matching cuts specified in the text.

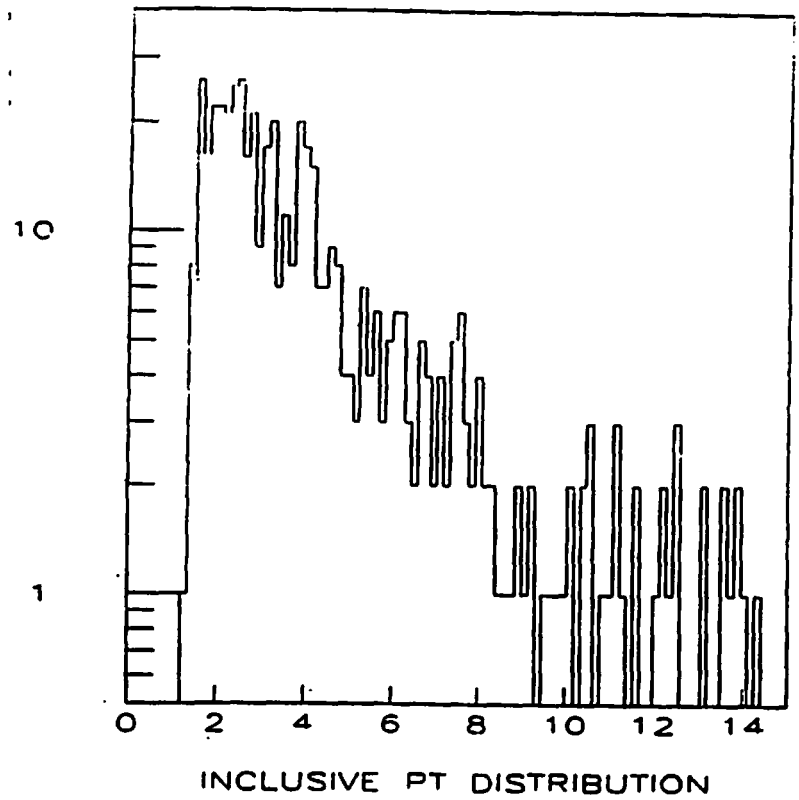

The P_t distribution of these muons is shown in fig 4.5 . It falls exponentially with increasing P_t . At high P_t ($P_t > 10$ GeV) the distribution flattens out. Muons having energy less than ≈ 1.5 GeV loose all their energy inside the calorimeter and don't often reach the muon chambers. Appropriate studies have been made on the amount of energy lost by muons in the calorimeter during the second calibration (*Testbeam*) of the detector, after the 1987 run. In Appendix-A the setup for this testbeam is sketched more in detail. Parts of the detectors were carried to a fixed target experimental area. Therein a pion or an electron beam was shot into the calorimeter tower to calibrate its response. It was possible to study

muons because a muon contamination of about 10% was present in the pion beam. Muons were tagged by a scintillator situated behind two meters of concrete placed behind the detector itself (fig 4.6) . The efficiency of the muon trigger was estimated as [23] :

$$\varepsilon = 95.2\% \pm 1.6\%$$

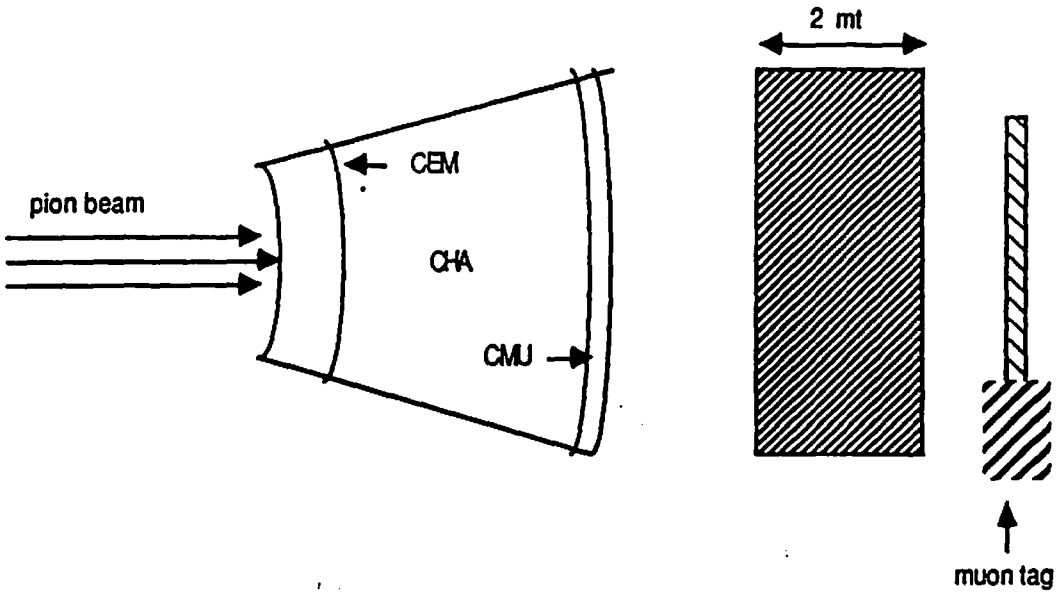

FIG 4.6 - Sketch of testbeam setup. Two wedges have been carried to M6, a fixed target area.

The inefficiency is due both to multiple scattering and to an inefficiency of the scintillator phototube.. An apposite run was made to study calorimeter response to muons. During this test run 3436 muons were tagged, at an energy of 57.1 GeV. The amount of energy released by the muons inside the electromagnetic calorimeter, the hadron calorimeter and the whole wedge is shown in fig 4.7a-c . The distribution of the energy lost follows the shape of a Landau distribution with a maximum around 2 GeV. As it is visible from the

FIG 4.7a -Energy deposited by the muon in the CEM (GeV)

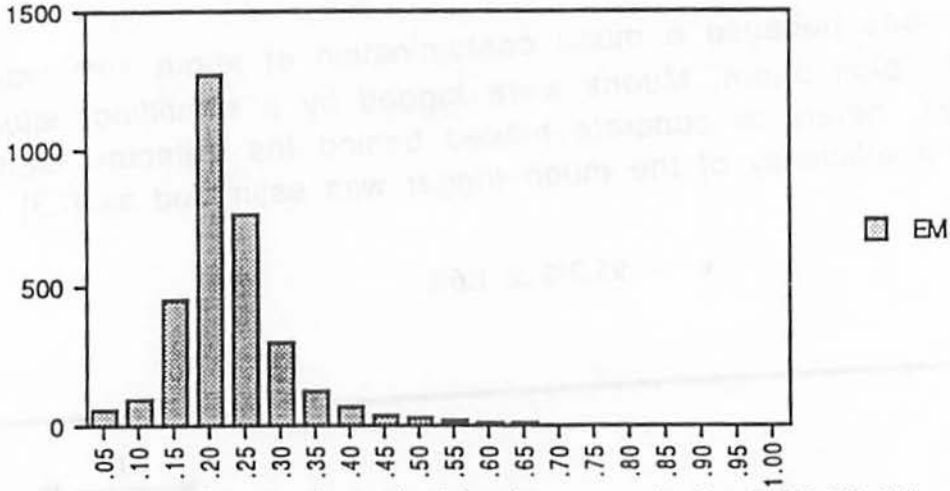

FIG 4.7b - Energy deposited by the muon in the CHA (GeV)

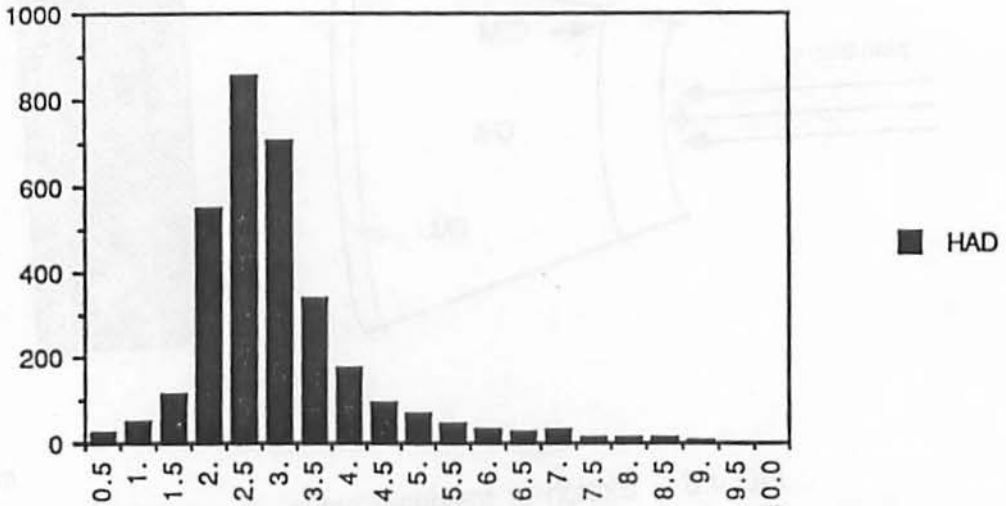

FIG 4.7c - Energy deposited by the muon CEM+CHA (GeV)

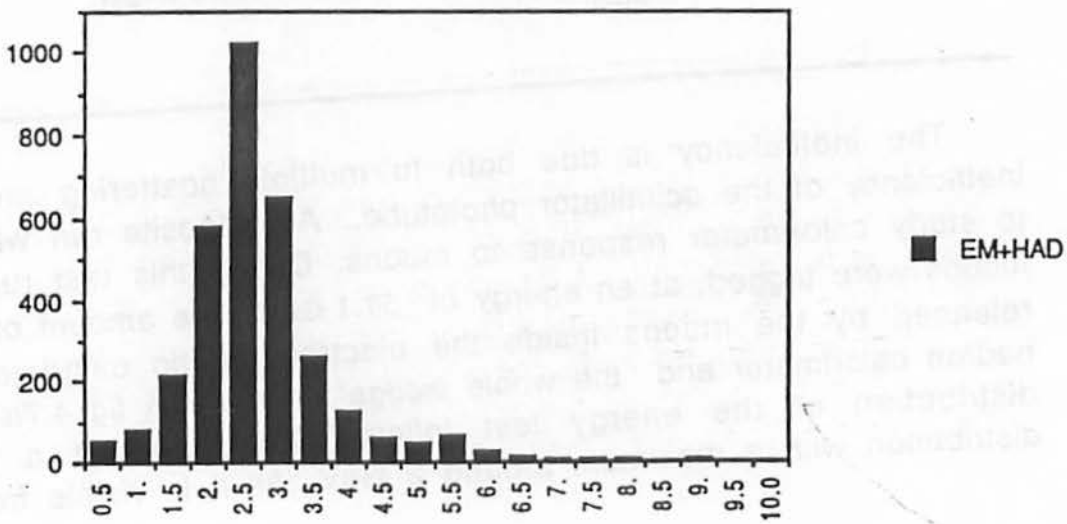

energy scale of figure 4.7, most of this energy is released inside the hadronic compartment of the central calorimeter. Because of this effect, the efficiency for finding μ's at low P_t is small.

Therefore we apply a momentum cut at Pt = 1.5 GeV . This cut reduces our sample to :

266 Dimuons
3 Trimuons

In our analysis we have not used yet the information about the correlation between *dx* and *dxslop* . As already said we expect, on average, to have :

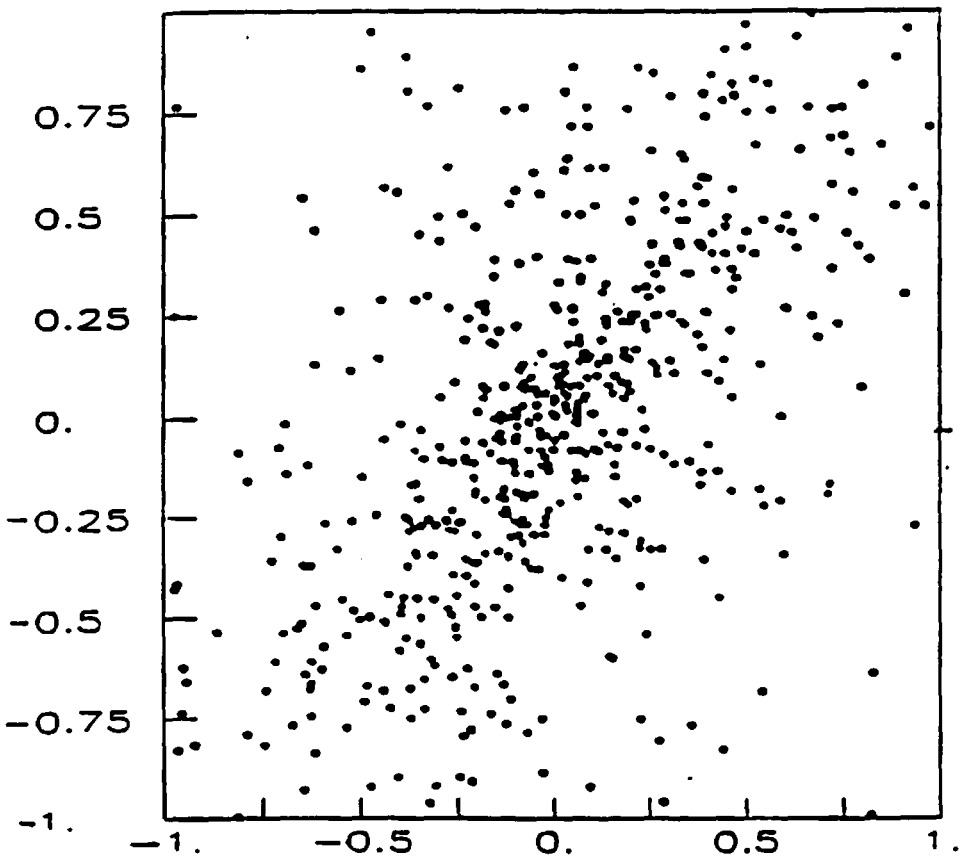

FIG 4.8 - dx versus dxslop. The plot shows a correlation that confirms the theoretical-phenomenological expression given in the text (arbitrary units) .

$$\langle dx \rangle = \frac{1}{\sqrt{3}} L \langle dxslop \rangle \qquad 4.3$$

In fig 4.8 we plot dx versus dxslop . The scales are chosen so that the straight line of equation 4.3 becomes the bisecant. The events are actually grouped around the line x=y . We, thus, cut events having :

$$X > y+1 \quad \text{or} \quad x < y-1$$

This cut leaves a final sample of :

248 DIMUONS
2 MULTIMUONS

In chapter 5 we will investigate the quality of these 'dimuon' events with a background analysis. In chapter 6 we will try to separate the different physical sources discussed in chapter 2 .

-TABLE 4.1 - Dimuon algorithm

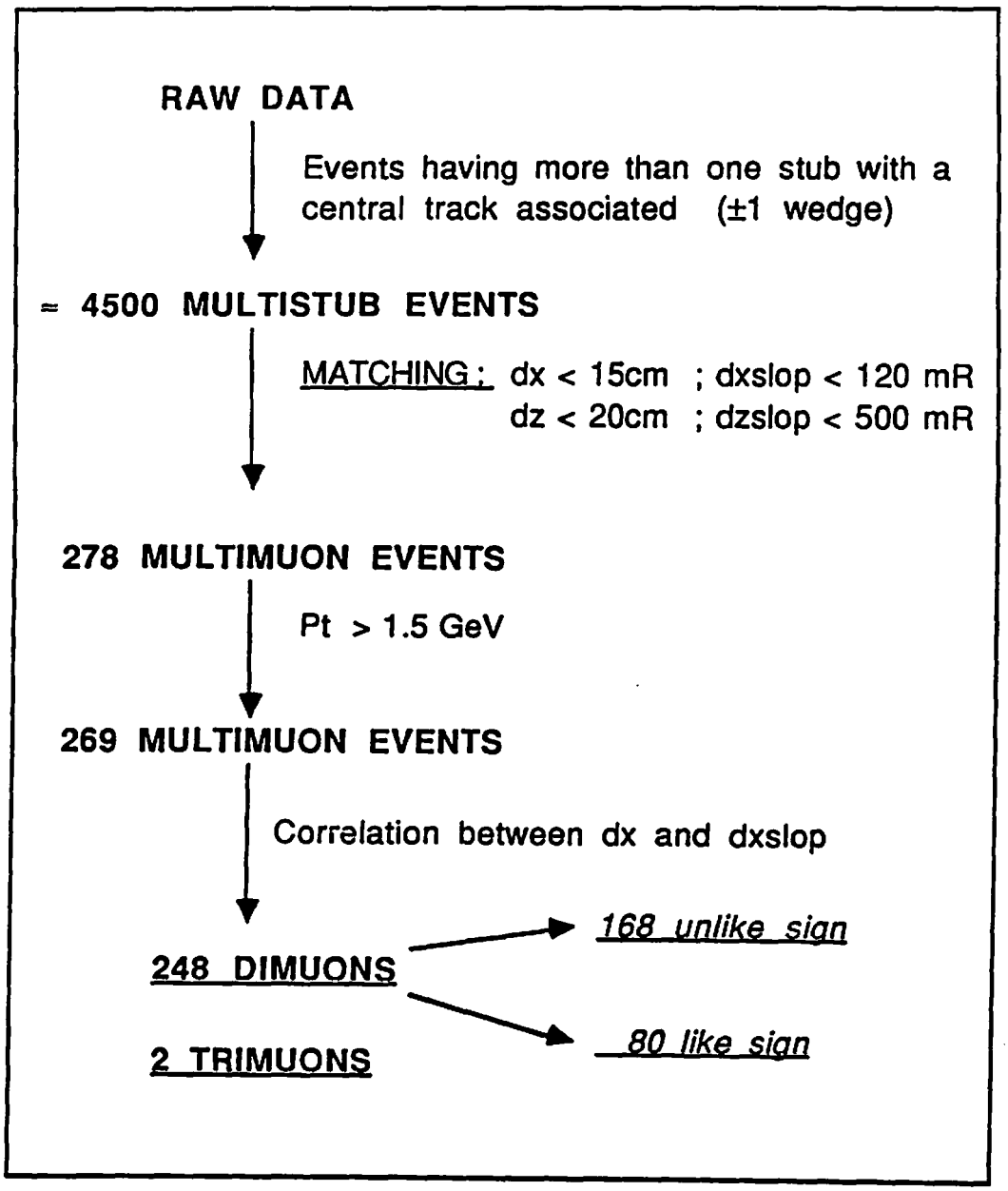

5 - BACKGROUND ANALYSIS

5.1 - Background sources

The events which have been selected as dimuons are certainly not all due to prompt muons from the physics sources discussed in chapter 2 . The sample is contaminated by some background : misidentified hadrons, muons coming from pion or kaon decays and so on. In this chapter we investigate the possible sources of background and we show an empirical approach based on a comparison with single muon data that will allow us to set an upper limit to the background contamination of our sample.

The main sources of background in dimuon events are:

- non-interacting punchthrough
- decays in flights
- leakage of hadronic showers

Other events that can give a signal in the muon chambers are cosmic rays and 'main ring splashes', shown in fig 5.1 . A cosmic ray can occur in coincidence with a beam crossing. A 'main ring splash' is an event caused by energy coming from the main ring, which is situated a few meters above the tevatron. The software filter can identify these events with an efficiency close to 100% .

5.2 - Non interacting punchthrough

Hadrons, mainly pions and kaons, have some probability of passing through the calorimeter without showering and reach the muon chambers. If this happens they are indistinguishable from

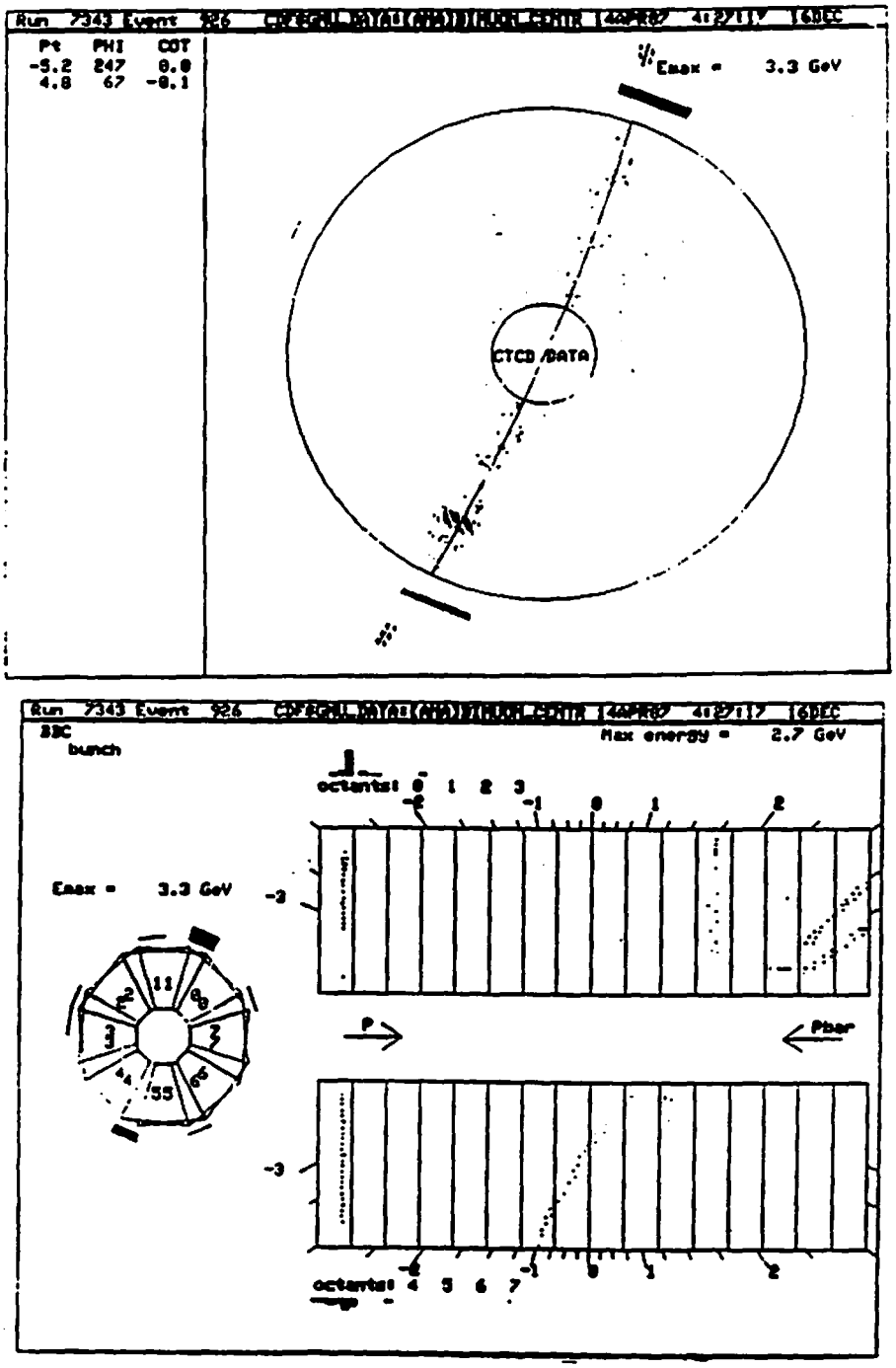

FIG 5.1 - Example of a cosmic ray in time with a beam crossing. The upper figure represents the CTC reconstruction. The lower figure is the vertex reconstruction. We can see the cosmic ray at the very left of the lower picture, while at the very right the soft event that fired the beam-beam counter trigger. The offline software recognize these events with a high efficiency (> 99%) .

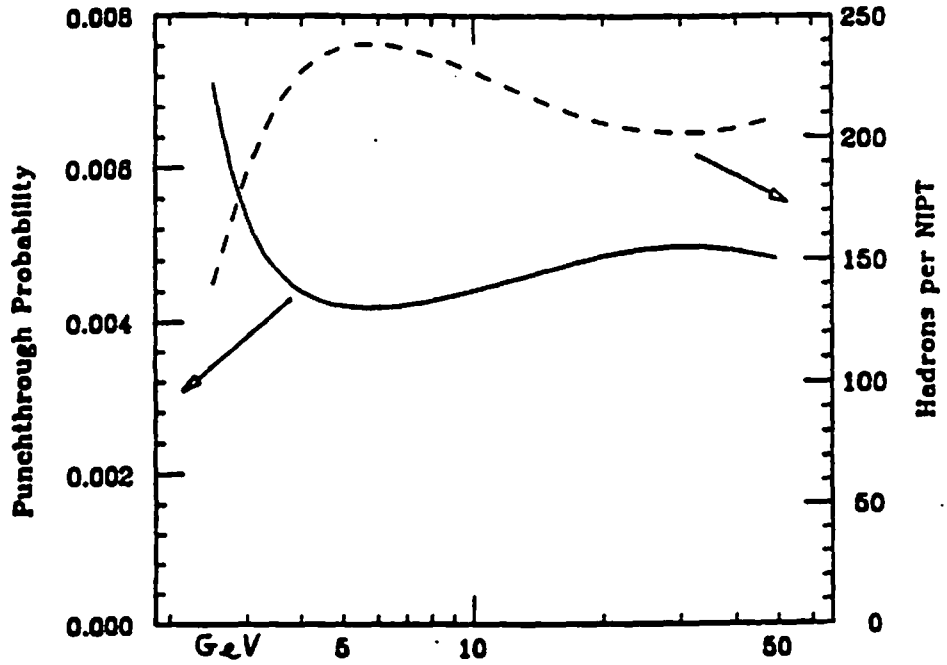

FIG 5.2 - Weighted sum of all the hadrons' punchthrough probability. The weights are $\pi : k : p = 50 : 23 : 20$ (UA5 results [25])

muons. The probability is related to the number of absorbtion lengths of the central calorimeter as follows :

$$P = e^{-\Lambda} = e^{-x/\lambda_{abs}}$$

The absorbtion length is, on its turn, related to the absorbtion cross section σ_{abs} between hadrons and the nucleons of the steel or of the other material forming the detector . The detailed calculation of σ_{abs} is discussed in appendix B. The resulting plot is shown in fig 5.2 [23]. In the plot it's reported the punchthrough probability of the hadrons present in the event assuming a ratio :

$$\pi : k : p = 50 : 23 : 20 \qquad \text{(UA5 results [25])}$$

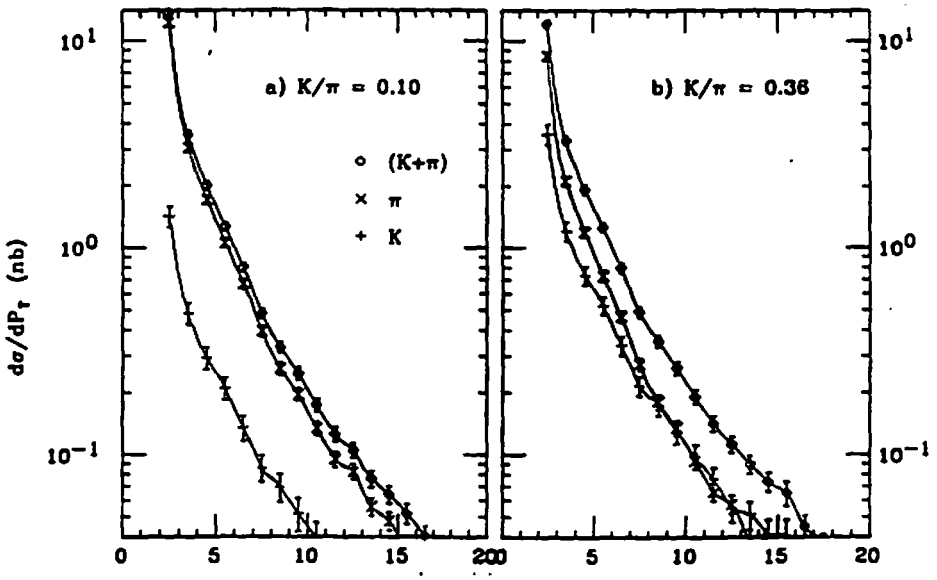

FIG 5.3 - Pt distribution of muons from hadron decay given, as an input, the spectrum of charged particles inside jets

5.3 - Decays in flight

Hadrons produced in a collision can also decay inside the calorimeter and give a muon as decay product. This process can be studied with a detector simulation. In appendix B the algorhythm used to evaluate the number of expected decays in flight is sketched in some detail [26]. In fig 5.3 we show the output distribution of secondary muons assuming, as input, the spectrum of charged particles inside jets.

5.4 - Leakage out of the calorimeter

When jets are present inside the calorimeter, there is the possibility that particles in a jet having late interactions shower in the last layers of the calorimeter and the hadronic cascade is not completely contained inside the calorimeter. High energy jets can

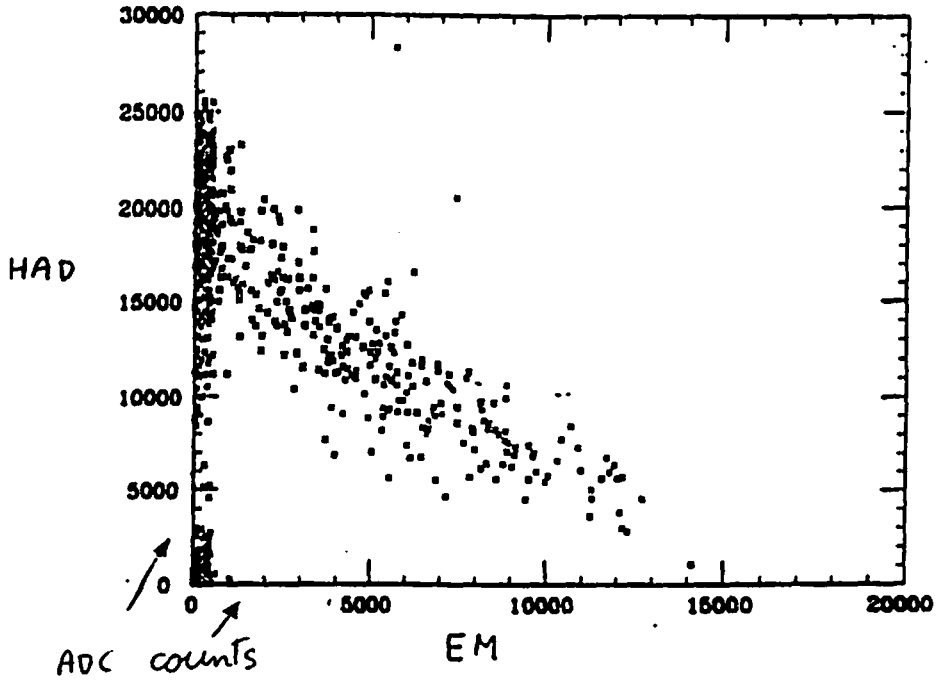

FIG 5.4 - Energy released in the electromagnetic calorimeter versus energy released in the hadronic one for those particles of a 50 GeV pion beam having at least one hit in the muon chambers.

reach the muon chambers. A study of this background was done analysing calorimeter response to known input beams [27]. At the Test Beam (see the appendix for a detailed description) a pion beam, with energy ranging from 15 GeV to 50 GeV was directed into a central calorimeter tower.

Fig 5.4 represents the energy deposited in the electromagnetic calorimeter versus the energy deposited in the hadronic one for particles that produced at least two hits in the muon chambers, in a 50 GeV pion beam. Events close to the origin are either real muons present in the pion beam or non interacting mesons. If we remove all these particles we can plot the ratio : (number of events showing hits in the muon chambers)/(total number of pion candidates) . Fig 5.5 shows this ratio for beam energies varying from 15 GeV to 50 GeV.

FIG 5.5 - (Number of interacting punchthrough particles)/(number of pions) for beams of different energies.

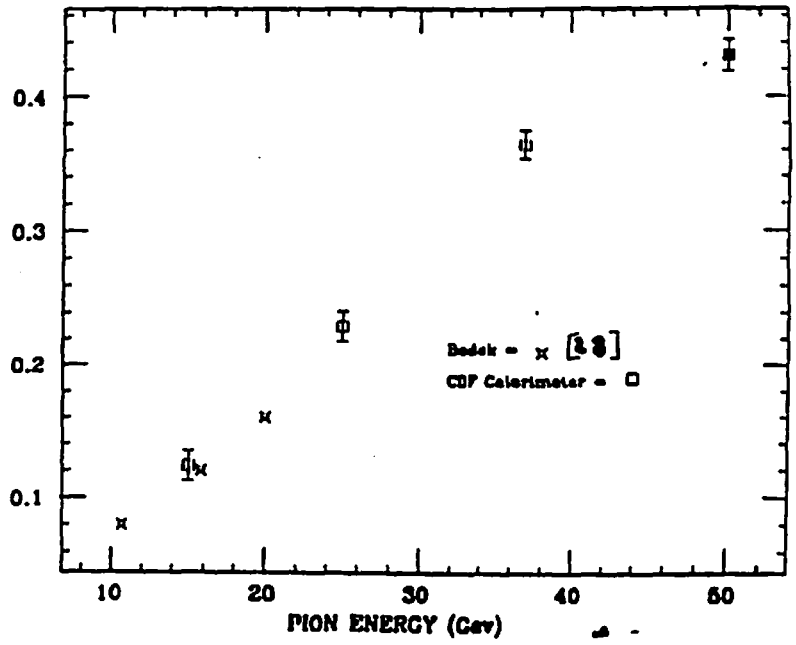

5.5 - Comparing with single muon events

An alternative approach to the background estimation in dimuon events is a comparison with single muon events.

The physical processes discussed in chapter 2, mostly lead to pairs of unlike sign muons. Only second order events, like second generation decays or B^0-$\overline{B^0}$ mixing or other exotic processes, yield pairs of muons having the same charge. On the other hand, all the background sources, discussed in the previous sections, *should* have the same probability of producing like or unlike muon pairs. Our dimuon sample of 248 events has :

168 unlike sign events
80 like sign events

So, provided background dimuons are as well like as unlike sign, a clear physical signal is present in our dimuon sampe.

To check our ansatz on background events distribution, a comparison with single muon events is used. A sample of 400 single

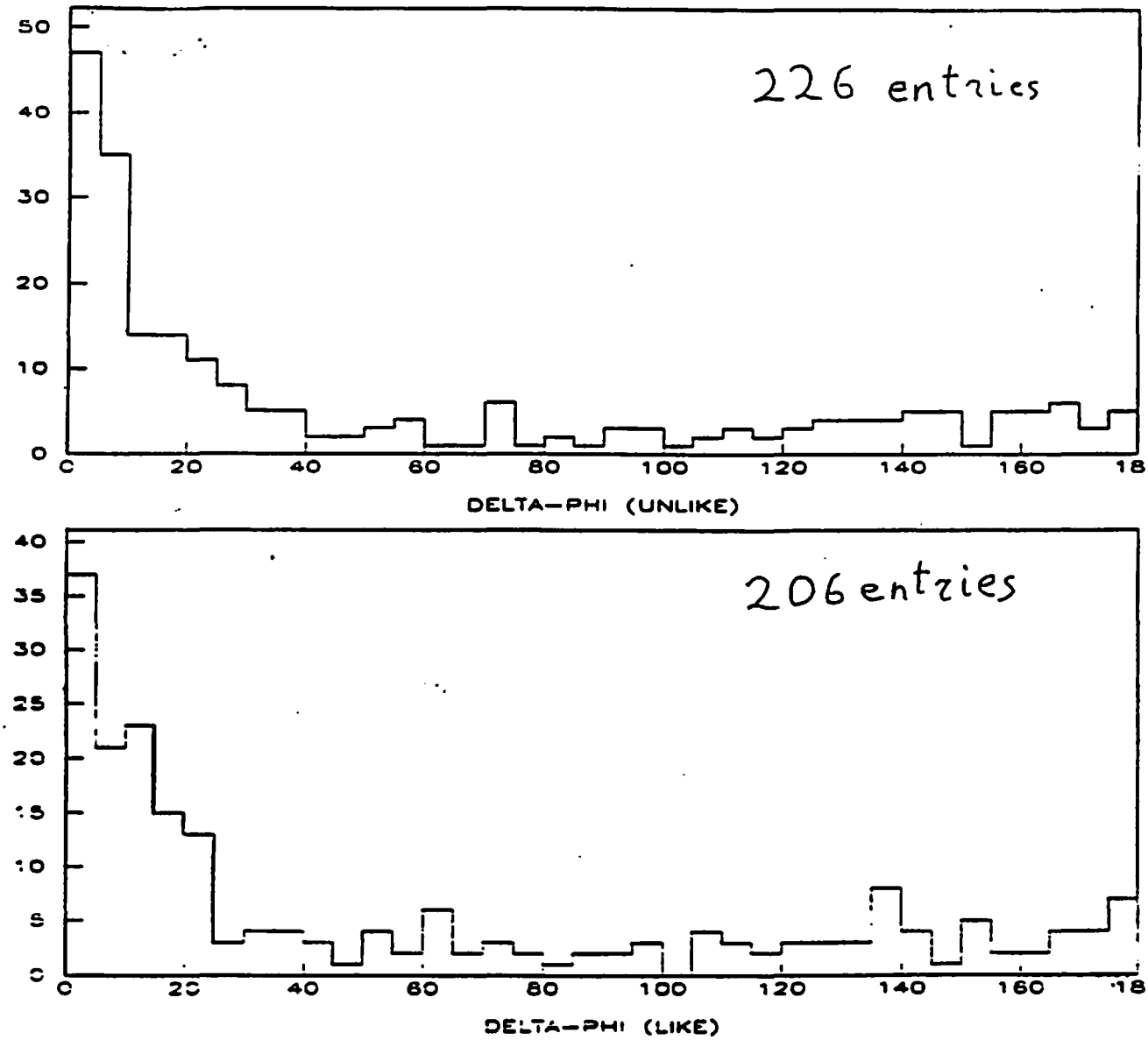

FIG 5.6 - Angle between the muon track and all the other charged tracks in the event satisfying the requests described in the text. The sample is from single muon events. In plot a) the muon and the track have opposite sign ('unlike sign event') ; in plot b) the muon and the track have the same sign ('like sign event') .

muon events was collected. The sample was unbiased. The only requests are :

$P_t > 2$ GeV
dx > 20 cm
dz > 20 cm
dxslop > 0.15 rad
dzslop > 1 rad

In the events chosen with these criteria, we consider all the charged tracks, besides the muon, having the following characteristics :

$P_t > 2$ GeV
3-D tracks (3-dimensional reconstruction)
$|\eta| < 0.7$ (pointing to the region covered by the muon chambers)

We then consider, for every event, all pairs of muon+charged track. We separate these pairs into two classes depending upon the charge of the muon and of the track: like sign event, if muon and track have the same sign; unlike sign event in the oposite situation. In fig 5.6 the relative angle in the r-ϕ plane for all these pairs is represented. Like sign and unike sign events behave approximately in the same way. To make this statement more quantitative we divide the plot in 3 bins :

$0° < \theta < 60°$ small angle zone
$60° < \theta < 120°$ intermediate angle zone
$120° < \theta < 180°$ wide angle zone

In these bins we calculate the ratio : (number of unlike sign events)/ (number of like sign events) . The result is plotted in fig 5.7 . We can compare these results with the dimuon sample. We plot, in fig 5.8, the angle between the two muons in the transverse plane for like and unlike sign pairs.

FIG 5.7 - (#unilke)/(#like) for single muon events

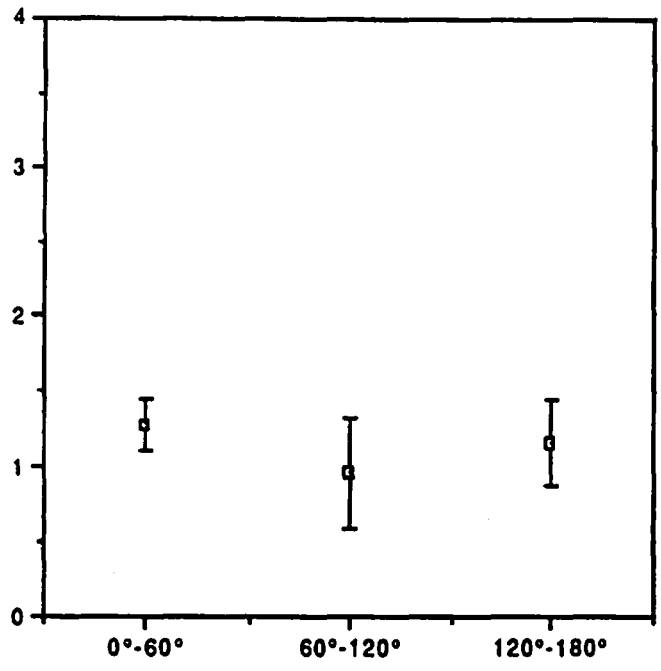

Again we divide the plot in three bins and we calculate, for every bin, the ratio (# unlike)/(# like) . The relative plot is shown in fig 5.9 . Fig 5.10 summarizes the results for single muons and for dimuons.

Using the information provided by these plots an upper limit to the background contamination of our sample can be set. We consider *all* like sign dimuon events as background and we call D_L their number. We define S_L and S_U as the number of like and unlike sign events collected from the single muon sample. The number of background events in the unlike sign sample, X_U, is given by the following proportion :

$$X_U : D_L = S_U : S_L \quad \Rightarrow \quad X_U = \frac{D_L * S_U}{S_L}$$

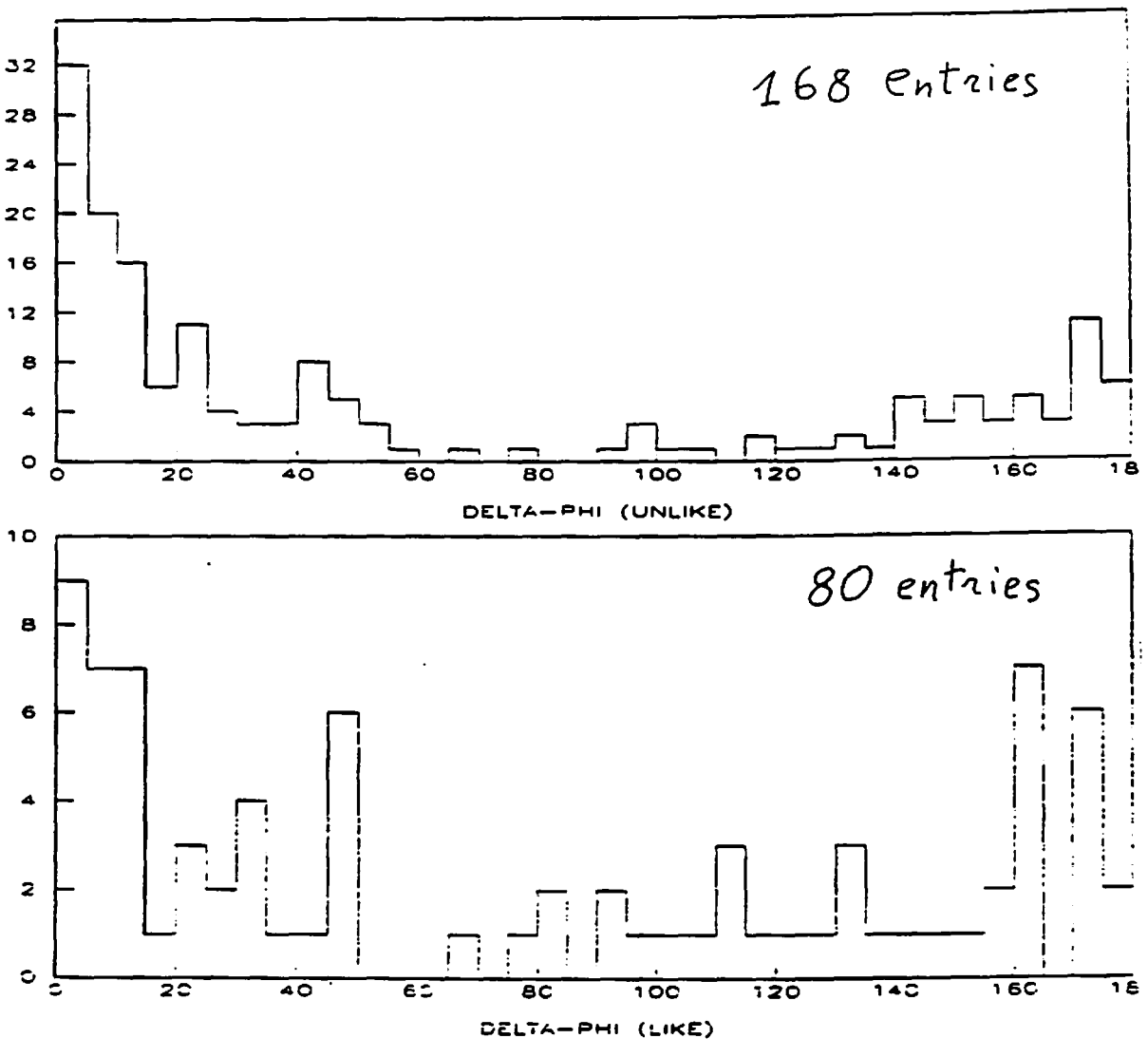

FIG 5.8 - $\Delta\phi$ between muon pairs. We can note a difference between the two distributions that we didn't note in the single muon sample (fig. 5.6) .

FIG 5.9 - (#unlike)/(#like) for dimuon events

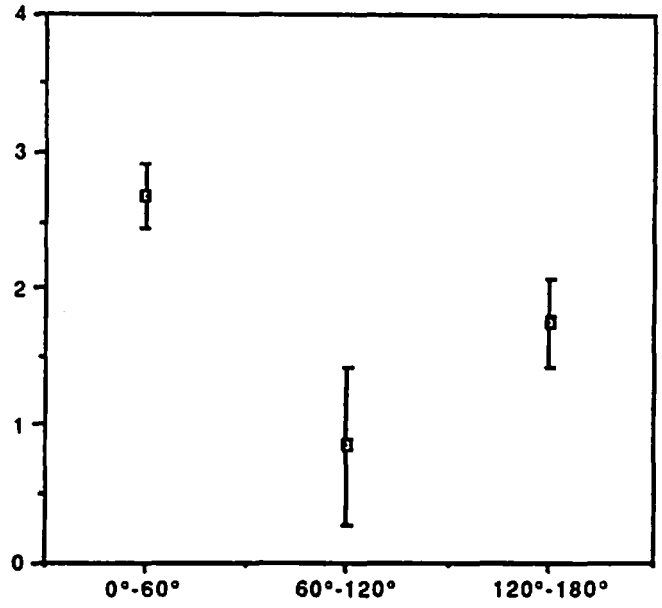

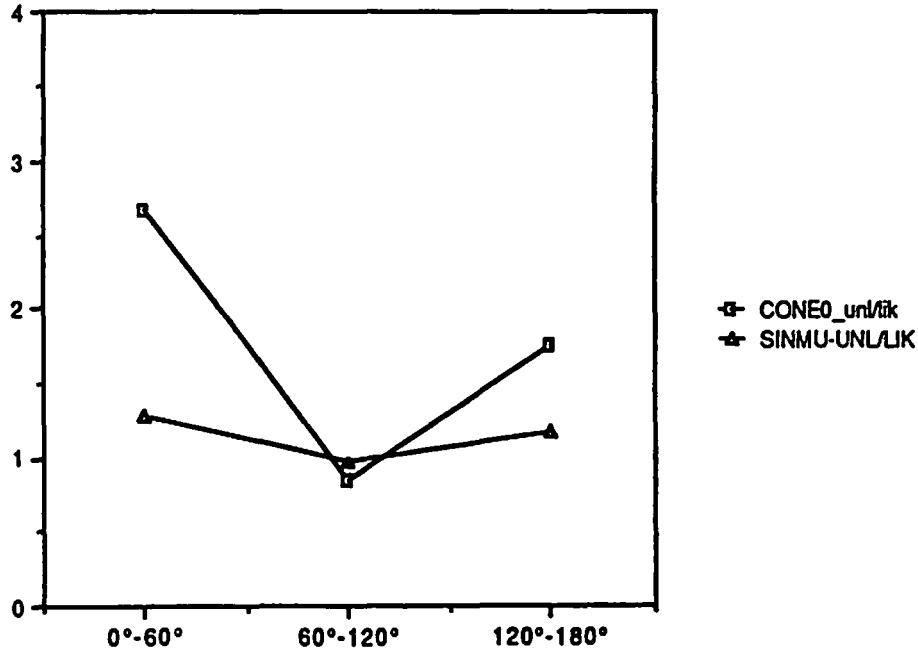

FIG 5.10 - Comparison betwenn fig 5.7 and fig 5.9

If D_U is the total number of *observed* unlike sign dimuon events, than the background contamination is :

$$B < 100 * \frac{X_U}{D_U} \%$$

Carrying on this calculation in the three angular regions gives :

$0° < \theta < 60°$ $\quad B < 48 \pm 10 \%$

$120° < \theta < 180°$ $\quad B < 67 \pm 29 \%$

Unlike sign dimuon events having $60° < \theta < 120°$ are consistent with background.

These are the upper limits to the background contamination of the dimuon sample collected at CDF in 1987 run as calculated comparing the behaviour of single and dimuon events.

6 - EVENT CLASSIFICATION

6.1 - The sample

The final number of events selected with our criteria is : 248 dimuon and 2 trimuon events. In fig 6.1 we can see the triggers that selected our sample. We remember that no dimuon trigger was present in 1987 run. Most of the events (74%) fired the muon trigger.

FIG 6.1 - Trigger status of the dimuon sample

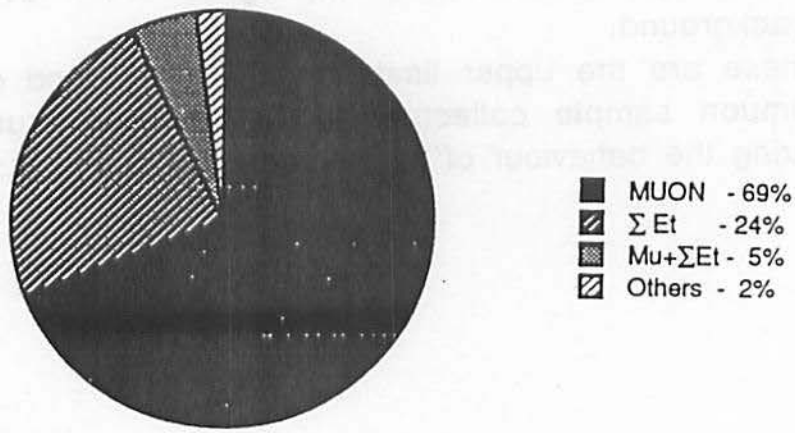

An estimation of the efficiency of the trigger is shown in fig 6.2 for the two thresholds used in 1987 run. This plot is the result of a calculation that takes into account both the multiple scattering of the particle into the detector and the finite size of the muon cell. As it is shown in fig 6.3, the angle β between a track and a radial line is direct_ly connected to the P_t of the particle (cfr equation 4.1.2). The angle β is measured by the difference in the time for detecting a particle by two cells in a tower (fig 6.4). If a particle scatters into the detector it reaches the Muon Chambers with a

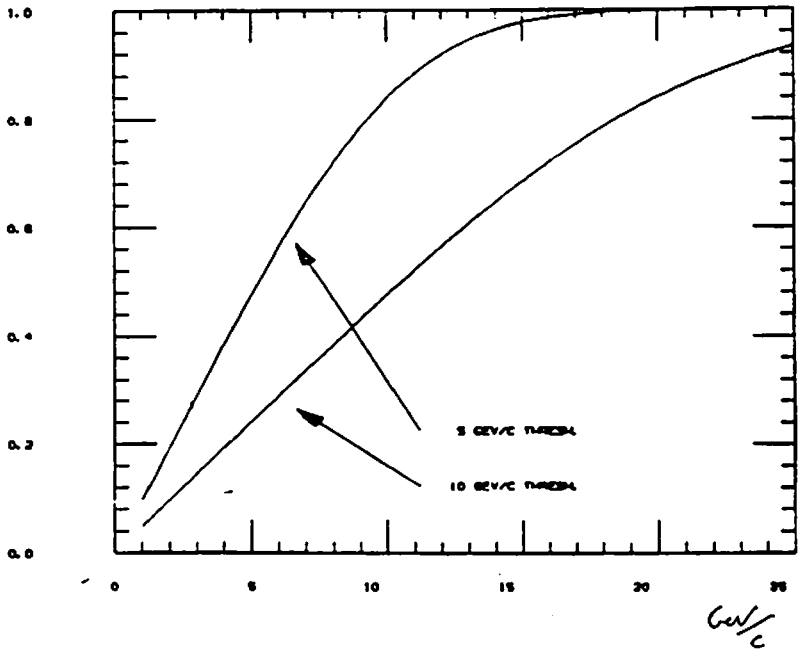

FIG 6.2 - Trigger efficiency for the thresholds used during the run.

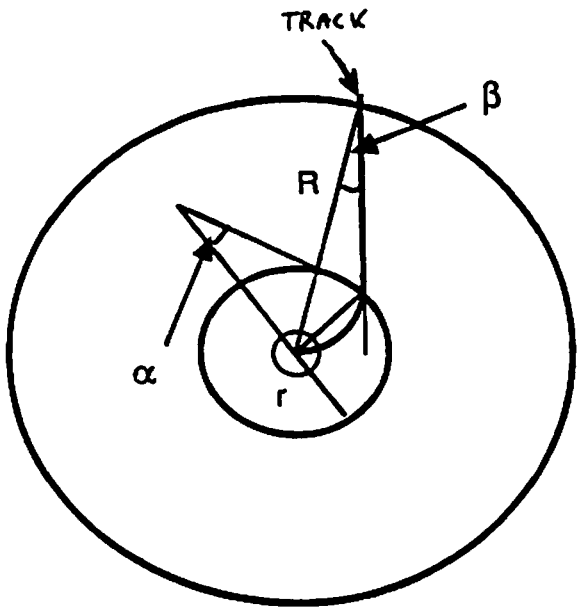

FIG 6.3 - Track path without multiple scattering into the detector. The bending angle β is connected to the particle momentum by equation 4.1.2 .

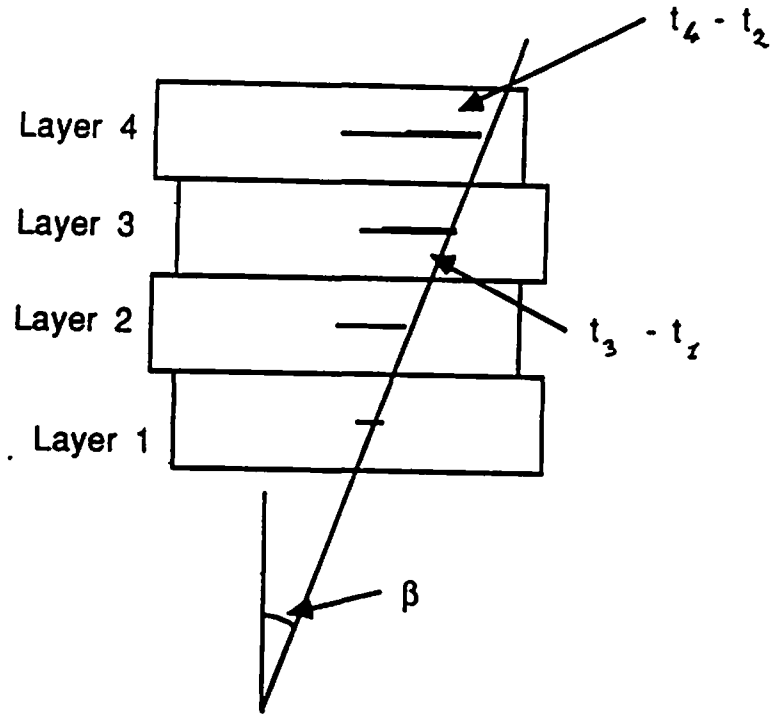

6.4 - Muon tower. The angle β is related to the particle momentum and it can be measured by the different time needed by the ℓ^- to reach the sense wire in two alternating layers. If the bending is too big the track can miss one or more layers and not being accepted.

different angle with respect to the β shown in fig 6.3 (see also the discussion in section 4.2) . In this way a low energy particle can fake a high energy one and viceversa. The finite size of the cell contributes to the error. In fact if a particle enters the cell close to the board of the cell itself and it has a wide angle β, then it can be rejected because not detected by the upper cells of the tower. In fig 6.2 the inefficiencies caused by multiple scattering and by the finite width of the cell are added in quadrature. Also the CTC measures the momentum with a certain error. This error is negligible compared to multiple scattering and to the Muon Chamber acceptance.

29% of the events fired the ΣE_t trigger (the sum of the two triggers is bigger than 100% because they overlap, as shown in fig 6.1) . That is to say the transverse energy in the event has to be bigger than 20, 30, 40 or 45 GeV depending upon the luminosity of the run.

Among the other events 3 were triggered by the electron trigger and 1 by the Minimum Bias trigger.

We can have a rough value estimation of muon trigger efficiency as follows :

$$\varepsilon_{TR} = \frac{(\#\text{events triggered by Muon}+\Sigma E_t)}{(\#\text{events triggered by } \Sigma E_t)} = 17\%$$

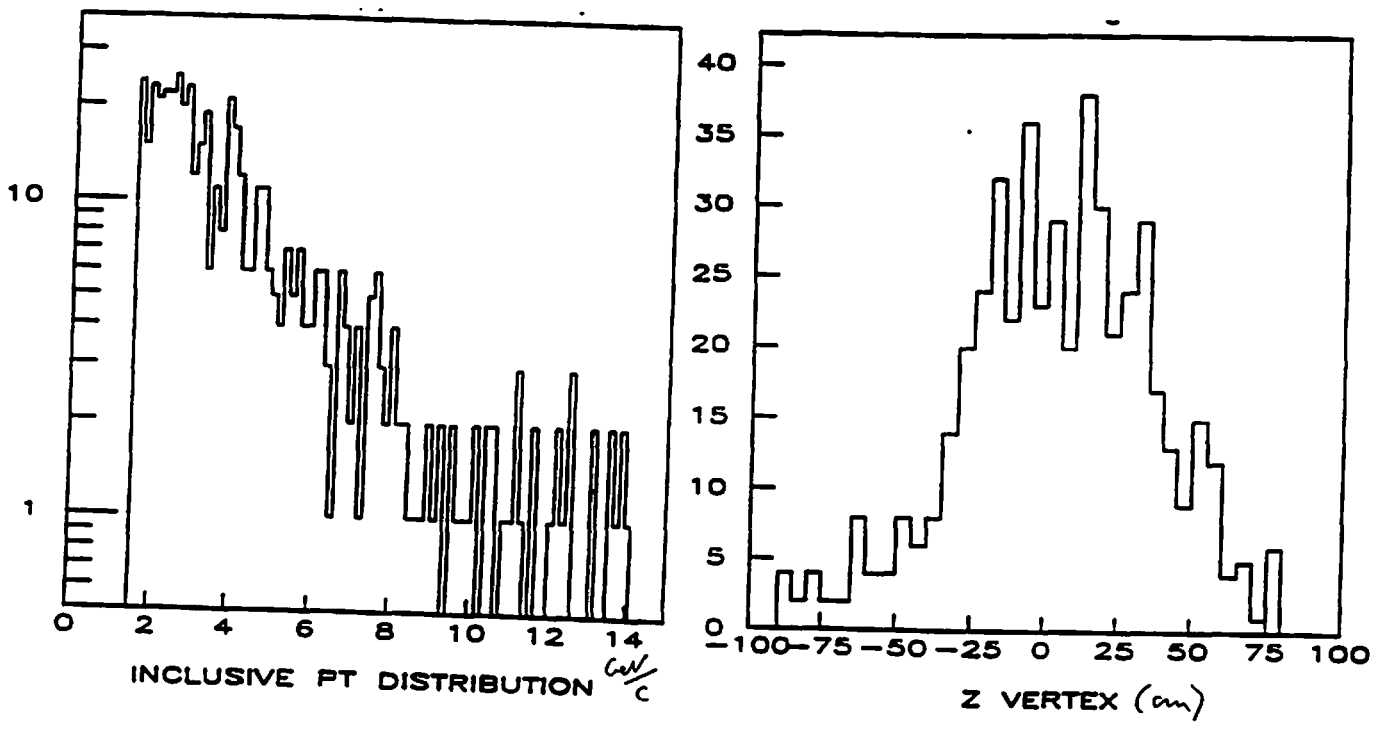

FIG 6.5- Final P_t distribution (left) and position of the vertex along the beam line (right) for the final dimuon sample.

If the ΣE_t trigger is fully efficient this ratio gives the fraction of times the muon trigger finds a muon. The value of 17% is consistent with the calculation represented in fig 6.2 if we consider an average P_t of 4 GeV (fig 6.5). The trigger efficiency is not well measured as a function of Pt and therefore it is the dominant error in our measurements.

In fig 6.5 we show the inclusive Pt distribution and the vertex position of the final sample. In fig 6.6 the invariant mass spectra are represented for unlike and like sign events respectively. The bin width for the upper plots is 500 MeV/channel to show the behaviour of the mass spectrum at high masses. The detector resolution can be derived by the expression of the invariant mass in function of the momenta of the outgoing muons. A calculation based on the momenta of the observed muons gives ≈100 MeV as the detector invariant mass resolution at low masses ($m_{\mu\mu} < 4$ GeV) increasing to 300 MeV for $m_{\mu\mu} \approx$ 10GeV . The lower plots of fig 6.6 show the invariant mass spectrum for $M\mu\mu < 15$ GeV taking a bin width of 100 MeV/channel.

In these events all the physical sources discussed in chapter 2 and all the background sources described in chapter 5 are contained. In the present chapter we will try, when possible, to separate different physical sources. The main tools that will be used are :

- sign of the pair
- muon isolation

The first criterion has already been discussed during our background analysis : physics processes mainly yield unlike sign dimuon events. This criterion is straightforward to apply. The sign of the muon is determined by the bending in the 1.5 tesla central magnetic field. Only very high Pt tracks (Pt > 100 GeV) can have a mismeasured sign.

The second criterion, muon isolation, is used to suppress background, as discussed in chapter 5, and to separate heavy flavour semileptonic decays from Drell-Yan events, decays of resonant quark states and Z° decays.

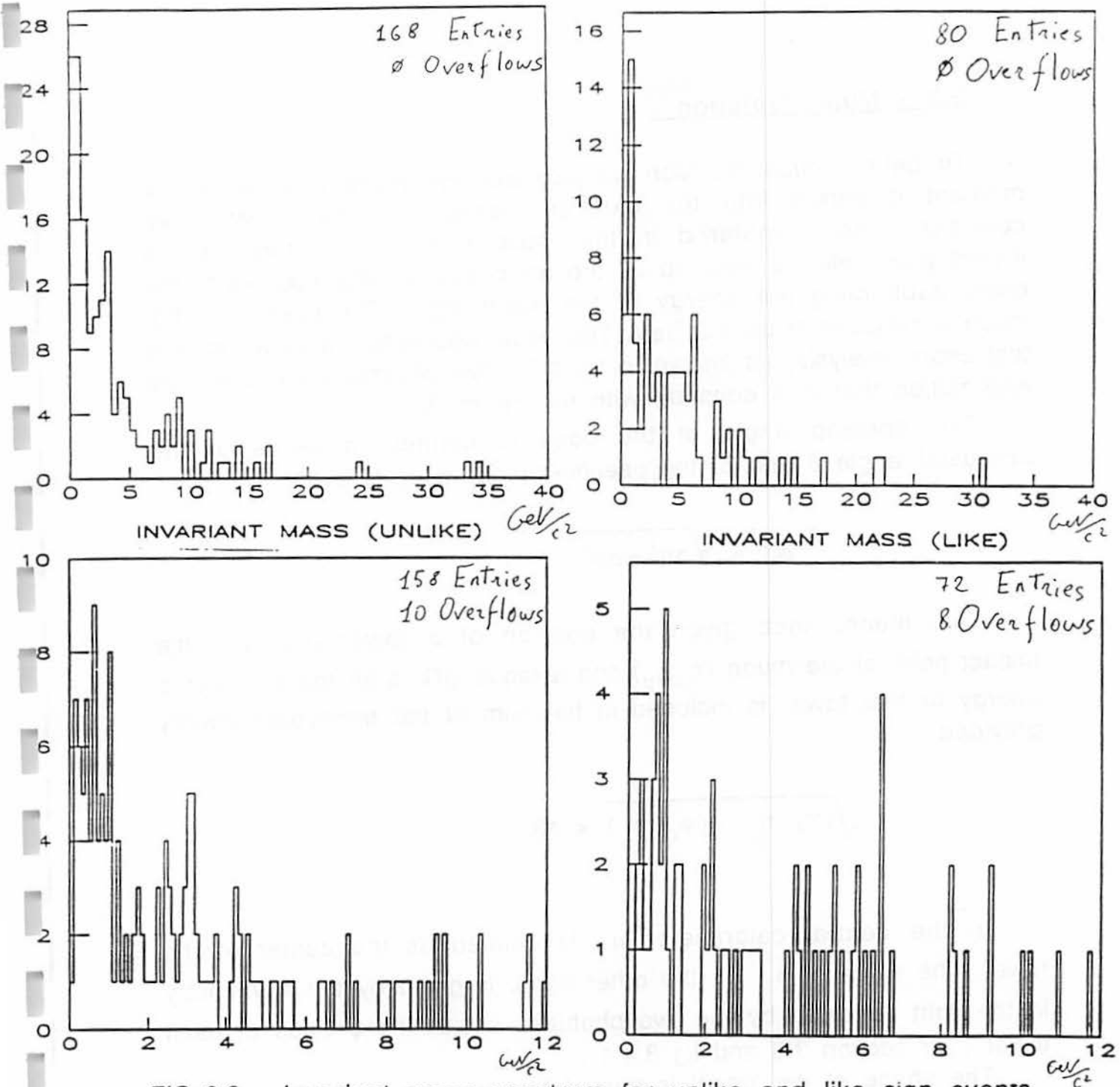

FIG 6.6 - Invariant mass spectrum for unlike and like sign events taking a bin width of 500 MeV/channel (upper plot) and of 100 MeV/channel (lower plot) .

6.2 - Muon isolation .

To define muon isolation we consider the muon position at the moment it enters into the electromagnetic calorimeter. We then consider a cone centered in the radial line passing through the impact point and we sum up all the transverse energy present in the cone, subtracting the energy of the muon itself. The energy fo the muon is chosen to be 2.2 GeV. This value was obtained as a result of test beam analysis, as shown in fig 4.7 . We will make the simplified assumption that it is constant with the muon P_t.

The opening angle of the cone is defined in terms of the azimuthal angle θ and of the pseudo-rapidity η as follows :

$$\Delta R = \sqrt{\Delta\eta^2 + \Delta\phi^2}$$

This means that, given the position of a tower (η_T,ϕ_T) , the impact point of the muon (η_μ,ϕ_μ) and a radius ΔR, than the transverse energy of that tower is included in the sum of the transverse energy provided :

$$\sqrt{(\eta_T-\eta_\mu)+(\phi_T-\phi_\mu)} < \Delta R$$

In the central calorimeter η_T is defined as the center of the tower. The value of ϕ_T, on the other hand, is given by the asymmetry in the light collected by the two photubes set at the ϕ ends of each tower (cfr section 3.3 and fig 3.4) .

The shape of the 'cone' is thus determined by the 'granularity' of the detector, that is by the dimensions of a tower. In fig 6.7 the (η,ϕ) plane is represented. Every square represents a projective tower

(the finer granularity of the plug can be noted). If we take (η_T,ϕ_T) as the center of the tower, then fig 6.7 represents different areas delimited by ΔR = cost .

The variable defining the isolation of a dimuon event is :

$$I_{\mu\mu} = \sqrt{(\Sigma E_t)_1^2 + (\Sigma E_t)_2^2}$$

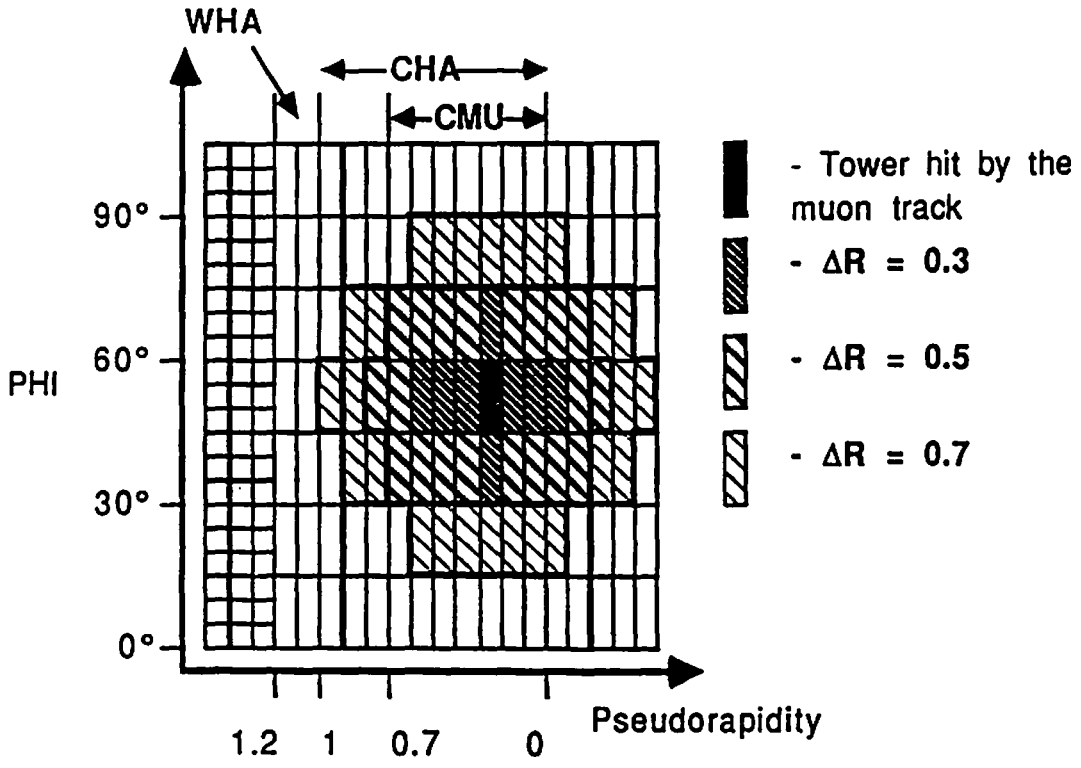

FIG 6.7 - Eta-Phi view of part of CDF detector. For central and wall detector the dimensions are 0.1 unit of rapidity and 15° (≈ 0.3 radians) in Phi. The plug has a finer azimuthal segmentation (5° ≈ 0.3 rad) . Shaded areas are surrounded by lines ΔR=const .

FIG 6.8a - Number of events in function of the cone width

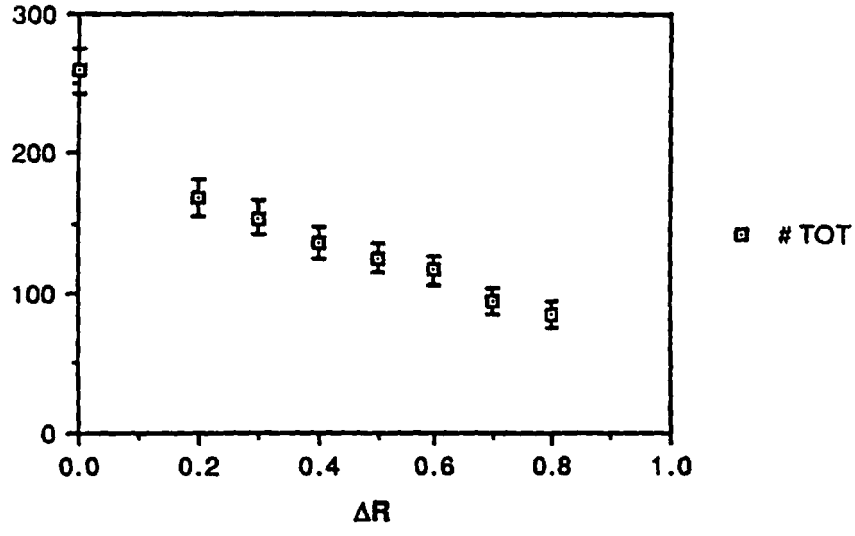

FIG 6.8b - (#unlike)/(#like) in function of the cone width

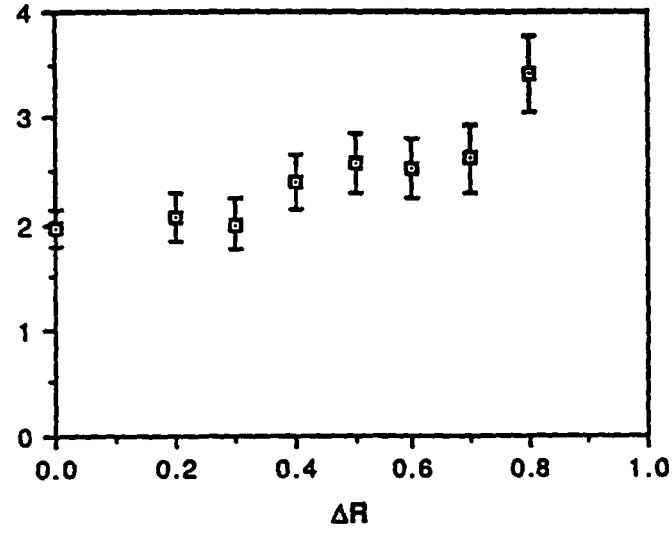

The points at $\Delta R = 0$ represent the whole sample with no isolation cut .

The two terms $(\sum E_t)_i$ represent the transverse energy inside the cones centered around the two muons.

In fig 6.8a we plot the number of dimuon events having $I_{\mu\mu} < 5$ GeV in a cone of radius ΔR in function of ΔR . The value of 5 GeV is consistent with the energy released in the underlying event as measured in minimum bias events. Fig 6.8b shows the ratio (#unlike)/(#like) for the different values of ΔR . As we can see the ratio increases with the increasing of the radius confirming that cutting on muon isolation actually suppresses background events.

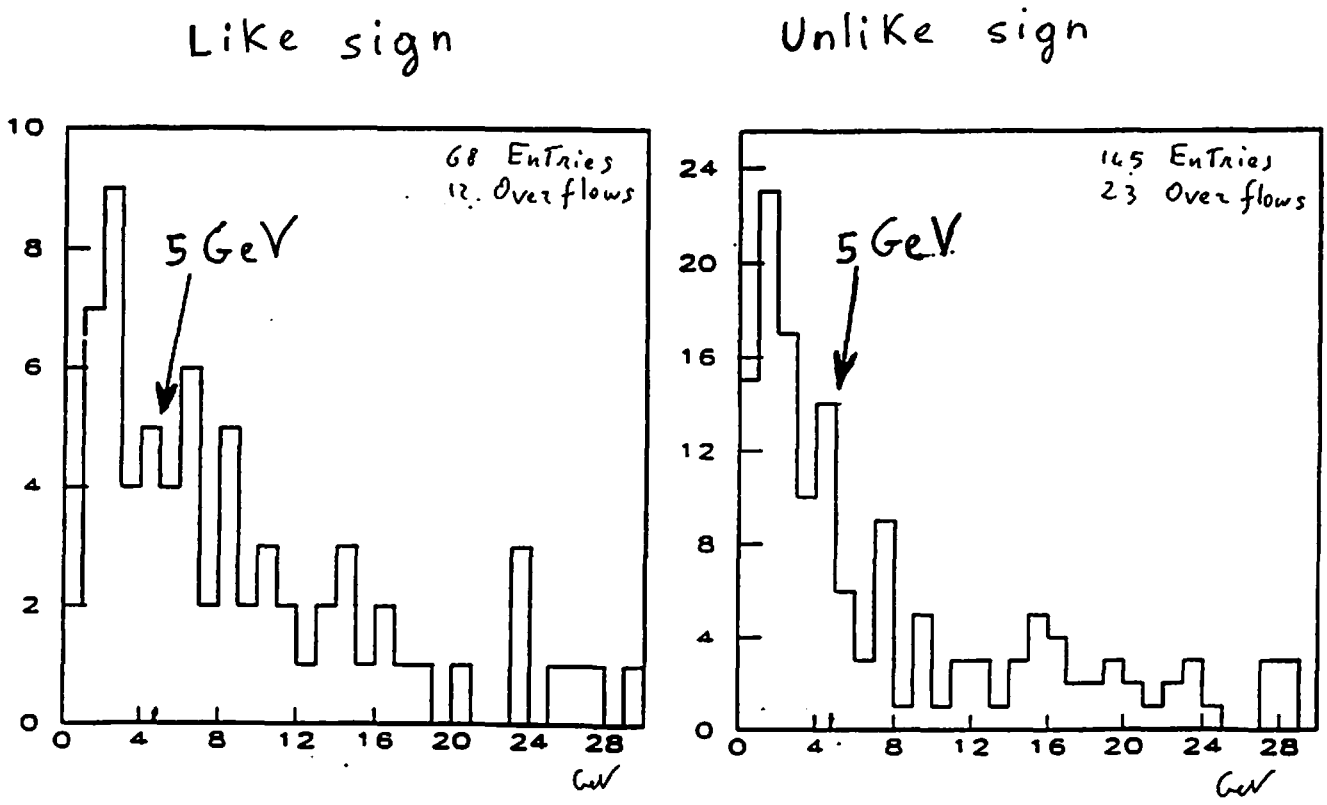

FIG 6.9 - Distribution of the variable $I_{\mu\mu}$ (see text) for a cone width of 0.6 for like sign (left) and unlike sign events (right) .

6.3 - Heavy quark resonant states

The decay of a resonant state results in an excess of events, in the invariant mass spectrum, in the bins corresponding to the mass of the particle. In fig 6.6 we can note, in the unlike sign spectrum, an excess of events corresponding to an invariant mass of 3 GeV . This excess has no correspondence in the like sign sample. This result is consistent with a physical signal coming from decays of J/Ψ state. At an invariant mass of 10 GeV we see a less significant excess of events.

To understand the significance of such "peaks" we apply an isolation cut. Isolation suppresses background events and events generated by heavy flavour semileptonic decays.

We choose a cone width of 0.6 , similar to the one used for defining jet events. We have repeated the fit of our data using different values of ΔR (0.5,0.7) and the results are the same within error. Fig 6.9 shows the spectrum of the isolation variable $I_{\mu\mu}$. If we cut at 5 GeV we obtain the invariant mass spectra shown in fig 6.10. The observed excess of events corresponding to the J/Ψ and Υ mass is still present.

To fit the mass distribution we assume that, with our isolation cut, we suppress *all* events deriving from heavy flavour semileptonic decays. In this way like sign dimouns are generated by the background sources discussed in chapter 5. Unlike sign events are generated by background, Drell-Yan processes and resonant state decays. Therefore we fit simultaneously the functions :

$$\begin{cases} F_{li}(m) = Ae^{-Bm} \\ F_{un}(m) = Ae^{-Bm} + \dfrac{C}{m^3} + \dfrac{D\Gamma_{J/\Psi}}{(m-m_{J/\Psi})^2+\Gamma_{J/\Psi}^2} + \dfrac{E\Gamma_{\Upsilon}}{(m-m_{\Upsilon})^2+\Gamma_{\Upsilon}^2} \end{cases}$$

F_{li} and F_{un} refer to like sign and to unlike sign events, respectively. It has to be noted that we use the same function, with

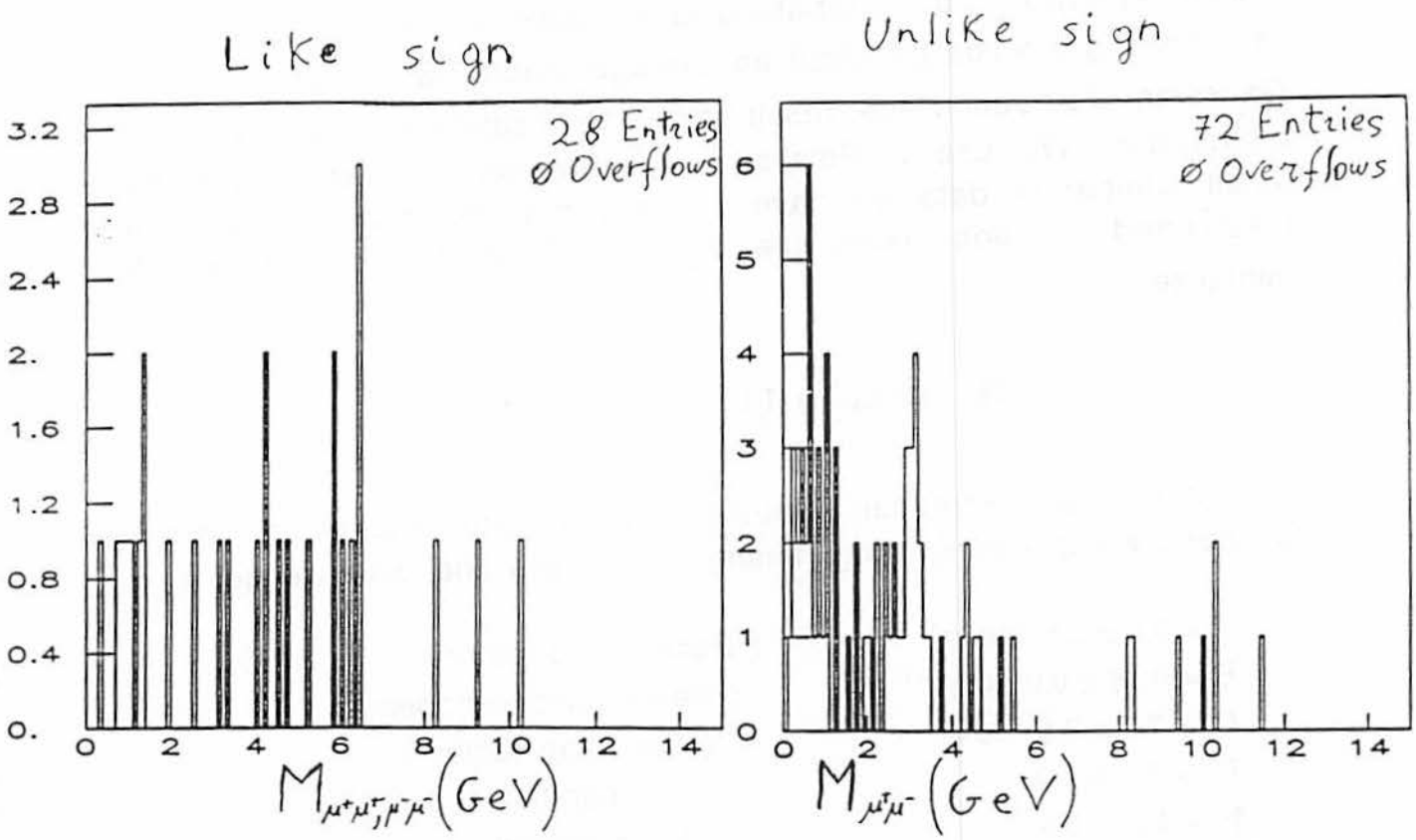

FIG 6.10 - Invariant mass distribution for events having $l_{\mu\mu} < 5$GeV in a cone having radius $\Delta R = 0.6$.

the same parameters, both for like and for unlike background distribution. In the unlike sign sample we have added the m^{-3} contribution of Drell-Yan events and two Lorentzian distributions, centered at the mass values of the resonant states. $m_{J/\Psi}$ was bounded by 2 and 4 GeV ; m_Υ by 9 and 11 GeV.

We fit the data minimizing the likelihood function. The likelihood function is defined as :

$$L = -2 \prod_i \log F(m_i, \mu_i)$$

where $F(m_i,\mu_i)$ is the probability distribution, in every mass bin i, of observing a value m_i given an average theoretical value μ_i. Using a Gaussian distribution the result is a minimization of the normal χ^2 distribution. We use a Poisson distribution, consistent with the small number of data we have in every bin. We then minimize the Likelihood function using the F_{un} and F_{li} at the same time. We minimize :

$$L = -2 \Pi_i \ln F(m_i,\mu_i^{un}) \Pi_j \ln F(m_j,\mu_j^{li})$$

where the theoretical values μ^{un} and μ^{li} are determined by the functions we are minimizing. Fitting in this way the data we get :

$A = 9.0 \pm 2.6$ GeV^{-1}	(Background factor)
$B = 0.28 \pm 0.05$ GeV^{-1}	(Background exponent)
$C = 7.0 \pm 2.6$ GeV^2	(Drell-Yan factor)
$D = 5.9 \pm 2.0$	(J/Ψ coefficient)
$E = 1.3 \pm 0.8$	(Υ coefficient)

The values we obtain for J/Ψ and Υ masses and widths are :

$m_{J/\Psi} = 3064 \pm 72$ MeV
$\Gamma_{J/\Psi} = 178 \pm 98$ MeV
$m_{\Upsilon} = 10221 \pm 286$ MeV
$\Gamma_{\Upsilon} = 500 \pm 250$ MeV

Fig 6.11 represents the fitted functions. The values obtained for the widths and the masses of the resonant states are consistent with the literature and with the detector mass resolution.

From the output values of our fit we can estimate a 3σ significance for the J/Ψ peak and a 1.5σ significance for the Υ 'peak'.

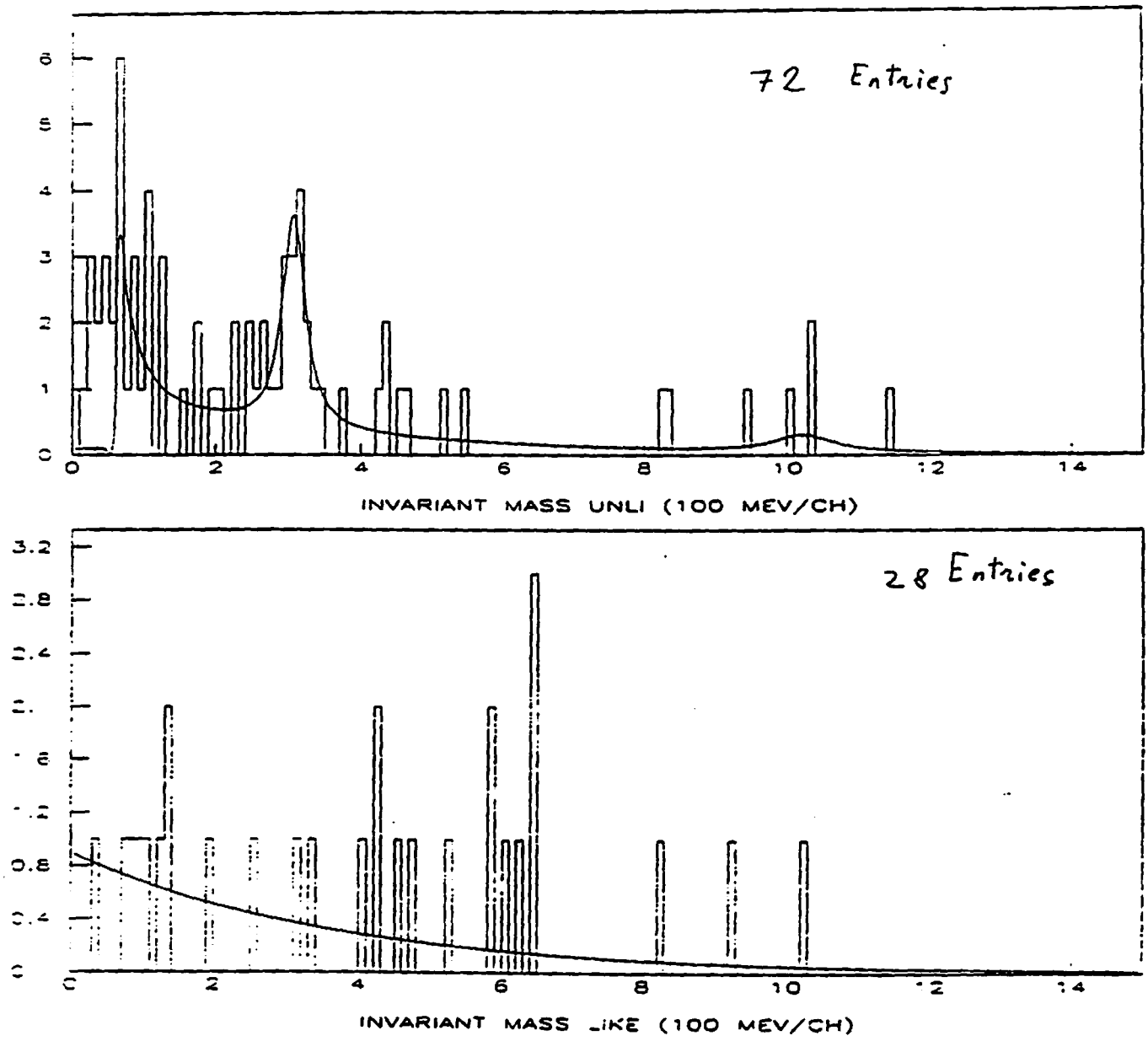

FIG 6.11 - Fit of the data plotted in fig 6.10 done with the likelihood method described in the test. The first 5 bins (500 MeV) were not used because of the effects of the detector that, especially in the low mass range, changes the expressions of the mass distributions.

The number of dimuon events expected in the unlike sample from background and Drell-Yan production is :

$$N_{B+DY}(\,2.8 < m < 3.3\,) = 2.00 \pm 0.87$$

$$N_{B+DY}(\,9.0 < m < 11.0\,) = 1.08 \pm 0.86$$

We observe 13 events having $2.8 < m < 3.3$, and 3 events having $9.0 < m < 11.0$. Therefore we estimate the number of observed resonant states as (11 ± 3.3) J/Ψ and (2 ± 1.4) Υ .

We can give an estimation of the J/Ψ cross section and an upper limit for Υ production.

To do this we need an estimation of the efficiency. For understanding the detector efficiency at the J/Ψ mass 6000 J/Ψ events were generated by Isajet and run through the full detector simulation. The number of events observed in the Central and in the Forward Muon system is 163, with a P_t cut at 2 GeV and loose matching cuts. Isolation cut was not made. If we assume a flat η distribution, for the outgoing muons, than the geometrical acceptance and the efficiency of our cuts is :

$$\varepsilon_{cut+geo} = \frac{163 \pm 12.8}{3*6000} = (\,0.9 \pm 0.1\,)\,\%$$

The factor of three is given by the absence of the Forward Muon System in 1987 run.

The trigger efficiency can be estimated by fig 6.5 . Muons from J/Ψ have an average Pt of 2.5 GeV, therefore we estimate :

$$\varepsilon_{trig} = (\,15 \pm 9\,)\,\%$$

The trigger efficiency has a large error because there was no precise method of determining it. No dimuon trigger was

implemented in 1987 run. The total efficiency is :

$$\varepsilon_{TOT} = (0.14 \pm 0.07)\,\%$$

Therefore an estimation of the cross section for J/Ψ production is :

$$\sigma_{J/\Psi} * BR\,(J/\Psi \rightarrow \mu^+\mu^-) = \frac{11 \pm 3.3}{(0.0014 \pm 0.0007)(27 \pm 5)\,nb^{-1}} =$$

$$= 291 \pm 87 \pm 199\ nb$$

In fig 6.12 it is shown one of the J/Ψ candidates.

In a similar way we can give an upper limit for Υ cross section at a 90% confidence level. With an analysis similar to the one done for J/Ψ we estimate the efficiency for the Υ detection to be :

$$\varepsilon_{TOT} = (0.56 \pm 0.32)\,\%$$

The number of observed Υ, (2.0 ± 1.4) , can fluctuate up to (2.0 + 1.4*1.64) = 4.3 ± 2.1 with a 90% confidence level. Therefore a limit on Υ production is :

$$\sigma_{\Upsilon} * BR\,(\Upsilon \rightarrow \mu^+\mu^-) < \frac{4.3 \pm 2.1}{(0.0056 \pm 0.0038)(27 \pm 5)\,nb^{-1}} =$$

$$= 28 \pm 14 \pm 18\ nb$$

6.4 - Drell-Yan events .

The mass spectrum for Drell-Yan events is obtained by the fit done on the events selected with our isolation cut. Using the results

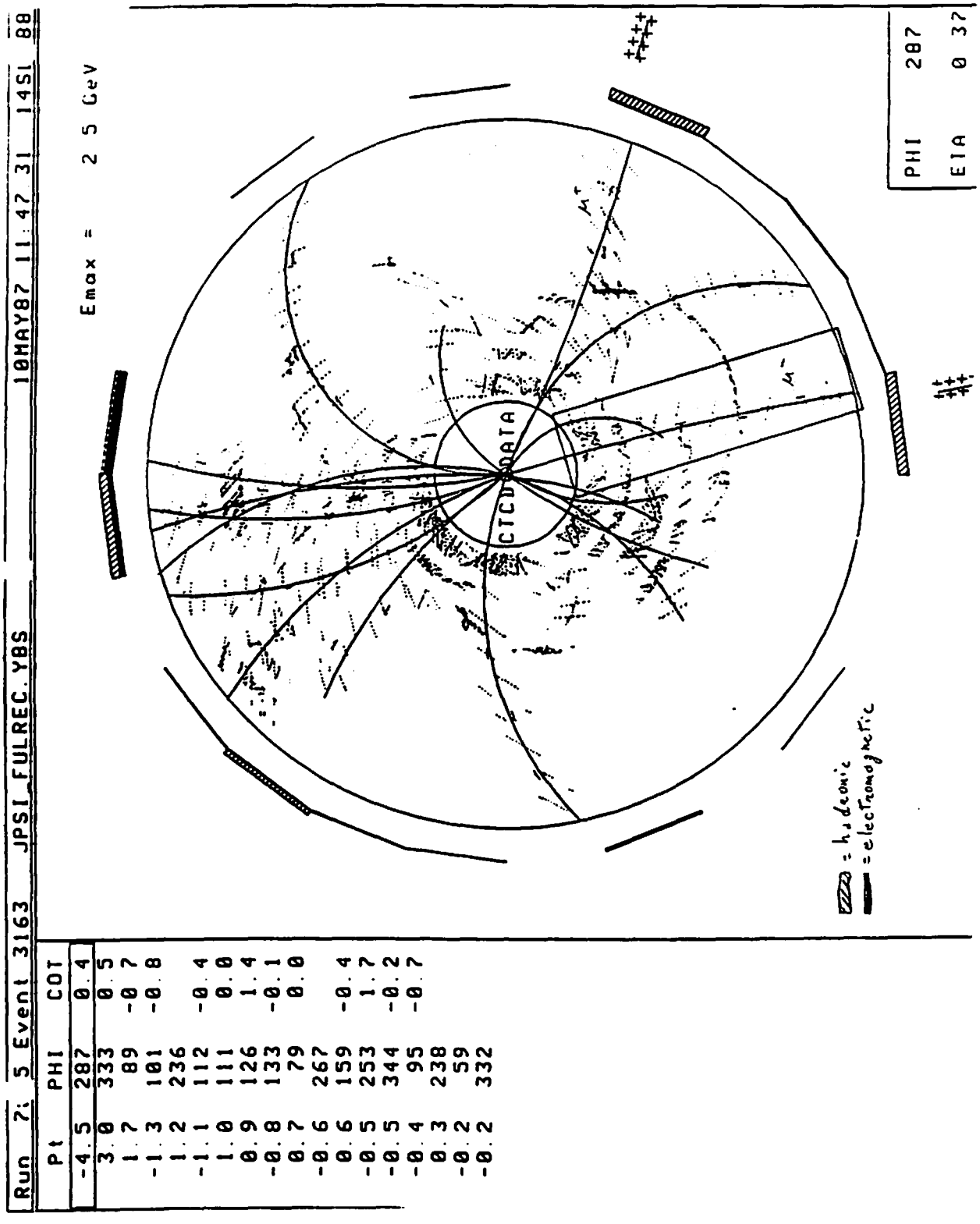

FIG 6.12 - CTC reconstruction of one of the J/Ψ candidates.

obtained in the previous section the differential cross section for D-Y events is proportional to:

$$\frac{dN_{DY}}{dm} = \frac{7.0 \pm 2.6}{m^3} GeV^{-1}$$

The value C(0.6) = 7.0 ± 2.7 obtained with a cone having ΔR = 0.6 doesn't depend upon the cone width. In fact using other values for the cone width ΔR, the value of the D-Y factor becomes :

C(0.4) = 7.7 ± 2.6
C(0.5) = 7.6 ± 2.9
C(0.7) = 7.6 ± 2.6

In chapter 2 we saw that :

$$\frac{d\sigma}{dm}(m) = \frac{8\pi}{3}\alpha^2 \frac{1}{m^3} F(\tau) \quad .$$

where :

$$\tau = \frac{m^2}{s}$$

We can consider τ constant for our interval of mass. In fact the invariant mass spectrum falls rapidly to 0 and $\sqrt{s} \gg m$. Therefore we can compare with other experiments the scaling differential cross section :

$$m^3 \frac{d\sigma}{dm} = m^3 \frac{d}{dm}\left(\frac{N_{DY}}{\varepsilon L}\right) = m^3 \frac{1}{\varepsilon L}\frac{dN_{DY}}{dm} = m^3 \frac{1}{\varepsilon L}\frac{7.0 \pm 2.6}{m^3} = \frac{7.0 \pm 2.6}{\varepsilon L}$$

where ε is the detector efficiency and L is the integrated luminosity. The detector efficiency was calculated generating 1500 events and looking at the number of accepted ones. Assuming a flat eta distribution and a (10 ± 5) % trigger efficiency, then the global efficiency turns out to be :

$$\varepsilon_{TOT} = (0.10 \pm 0.07)\,\%$$

Taking the theoretical calculation done by Altarelli et al. [59] , the fraction of Drell-Yan events at a rapidity y =0 is 0.2 of the total number of Drell-Yan decays . Therefore :

$$m^3 \frac{d^2\sigma}{dm\,dy}\Big|_{y=0} = \frac{0.2 * (7.0 \pm 2.6)\,GeV^2}{(0.001 \pm 0.0007)(27 \pm 5)\,nb^{-1}} =$$

$$= 52 \pm 19 \pm 46 \;\; nb\,GeV^2$$

In fig 6.13 we compare our results with the results of other experiments.

6.5 - Z° decays

Another source of (unlike sign) dimuon events is the decay of the neutral boson Z°. These events are characterized by the high invariant mass of the pair, peaked at 90 GeV, well above the masses of the processes described in the previous sections. As we can see from the invariant mass spectrum of the unlike sign sample of fig 6.3, no dimuon events have invariant mass above 40 GeV. This result is not inconsistent with expectations. The Z° cross section at $\sqrt{s}$ = 1800 GeV , calculated taking m_{top} = 40 GeV , is :

$$\sigma_Z * B(Z \to \mu^+\mu^-) = 0.18 \pm 0.06\,nb$$

The detector and trigger efficiency at the Z° mass calculated by Isajet simulation is :

$$\varepsilon = 16.9\,\%$$

Therefore the number of Z° events expected in the dimuon channel is :

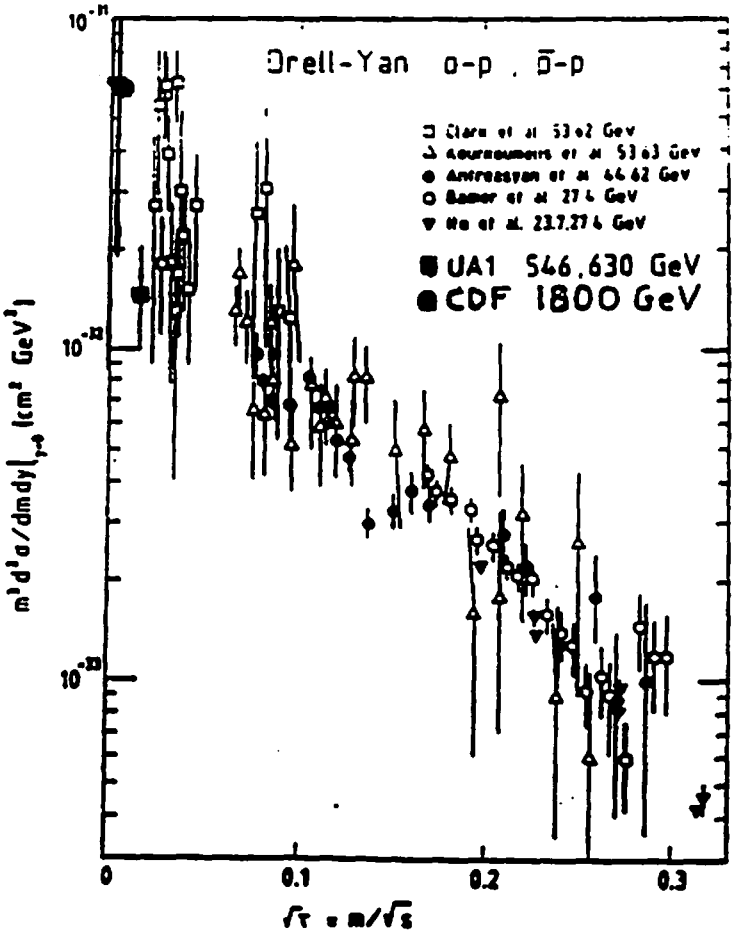

FIG 6.13 - CDF cross-section for Drell-Yan events compared to lower energy *pp* and $p\bar{p}$ experiments [16] . The substial agreement shows that the simple scaling prediction still holds at small $\sqrt{\tau}$ values .

$$N_{Z^0} = (0.18 \pm 0.06)\text{nb} * 27.2\ \text{nb}^{-1} * 0.169 = 2 \pm 0.6$$

Given a Poisson distribution of events with mean μ=2, the possibility of seeing no events is :

$$P(0,2) = e^{-2}\frac{2^0}{0!} = 13.5\ \%$$

Therefore our observations are not inconsistent with expectations. Other possibilities for explaining the lack of observed Z° decays are that the MonteCarlo simulation overestimated the efficiency or that the cross section is slightly different from the calculated value. For answering this question more events are needed.

6.6 - Heavy flavour semileptonic decay

Muons produced by heavy flavour semileptonic decays are not isolated. Therefore their mass spectrum is represented by the spectrum of events that don't satisfy the isolation criterium used previously. In fig 6.14 the mass spectrum of the 148 non isolated events (88 unlike sign ; 60 like sign) is reported. The P_t spectrum of these events is shown in fig 6.15 .

To check the consistency of our data with the expectations a sample of 100,000 $b\bar{b}$ were generated. Applying the same cuts used to select our sample, the number of events accepted by the simulated offline reconstruction was 400. The $b\bar{b}$ expected cross section at $\sqrt{s}$ = 1800GeV is (cfr 2.4) :

$$\sigma = 0.27\ \mu b$$

Given a total efficiency of 0.4 %, the number of expected events is :

$N = 270\ nb^{-1} * 27\ nb * 0.004 = \underline{29}$

The contribution of $c\bar{c}$ decays turns out to be suppresed a factor of 10 because of the cut on muon P_t (see, for example, [16] page14). If

FIG 6.14 - Invariant mass distribution for non isolated events

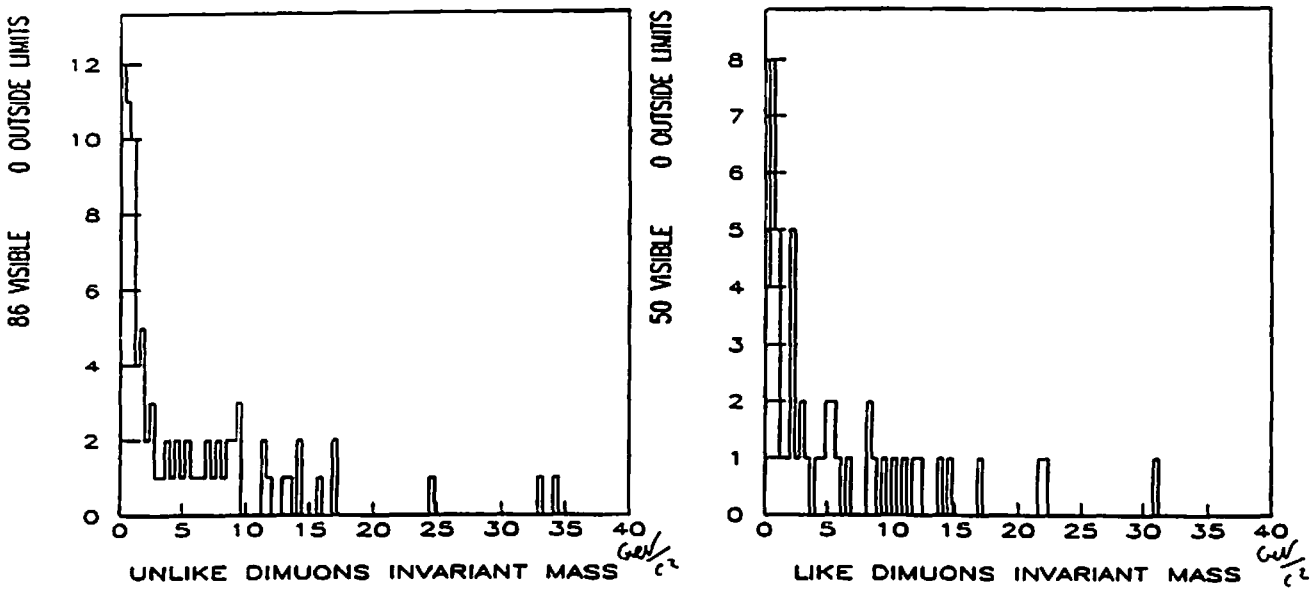

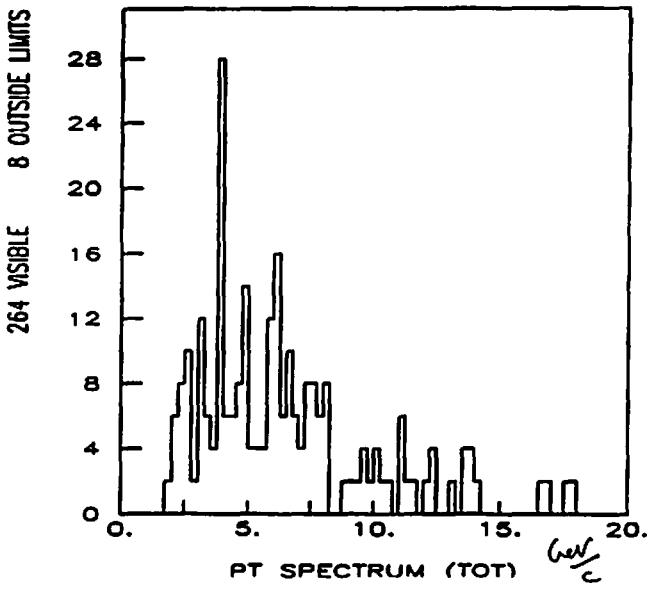

FIG 6.15 - P_t distribution of non isolated events

FIG 6.16 - CTC reconstruction of the 2 trimuon events.

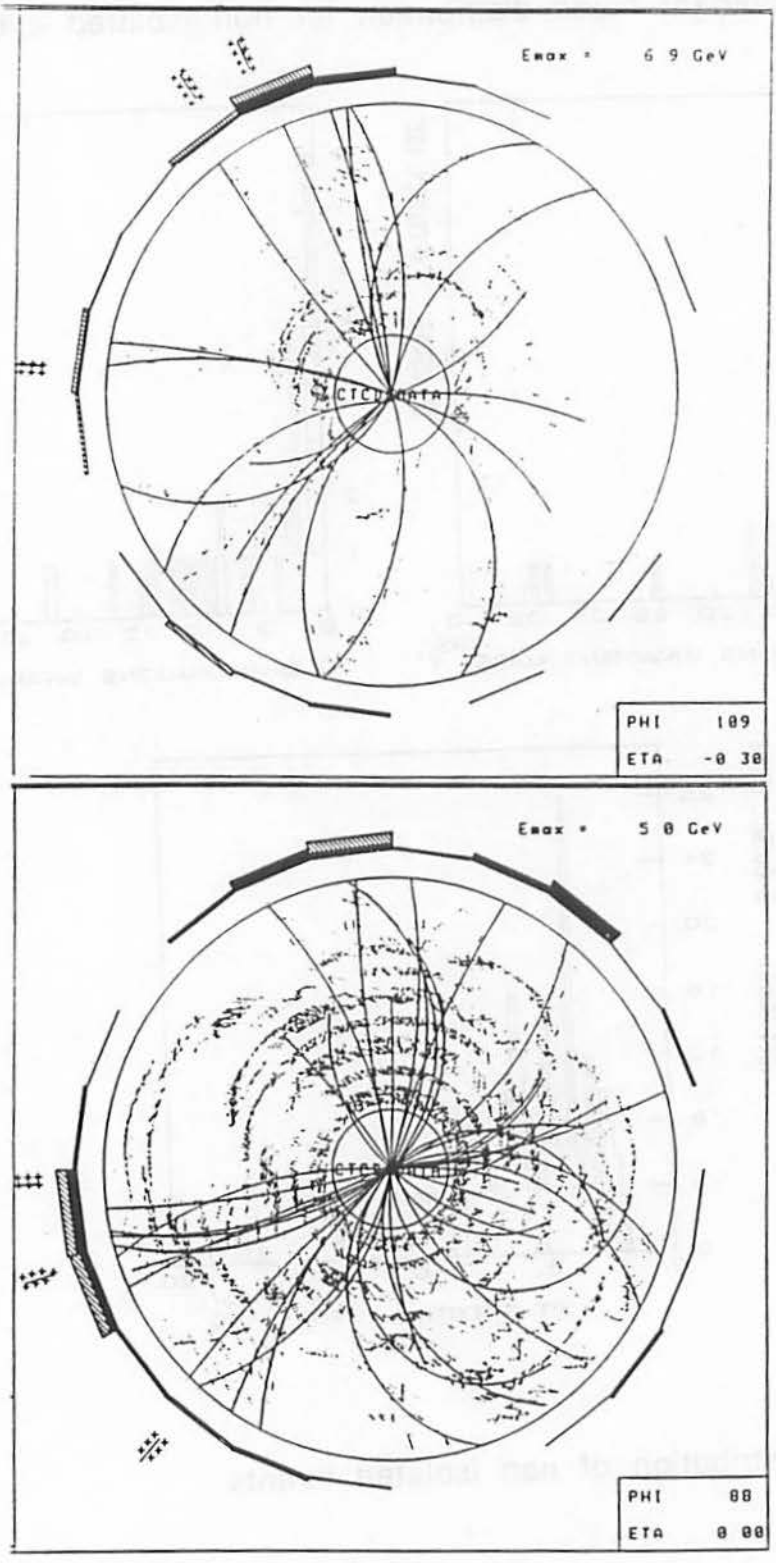

we simply subtract the number of like sign events from the number of unlike sign events, we are left with 36 events. This value is not inconsistent with the number of non isolated events expected. Non isolated events are more contaminated by background than isolated events. Therefore to study the physics of heavy flavours we need a bigger sample of events.

6.7 Multimuon events

The two events having three muons are displayed in fig 6.16. On an event per event basis it is not possible to say if these events are consistent with a heavy flavour semileptonic decay cascade. Naively one would expect muons from such processes to have wider relative angles. The upper event represented in fig 6.16 is atypical also because of the very good isolation of all the three muons : $\Sigma E_t < 2GeV$ in a cone of radius $\Delta R = 0.6$. With the luminosity integrated in 1987 run no conclusions can be drawn from this sample.

7 - SUMMARY AND CONCLUSION

In this thesis we have shown an analysis of dimuon events from the sample of data collected in 1987 run with an integrated luminosity of 27 nb^{-1}. The momentum cut and the matching cuts, discussed in chapter 4 and shown in table 4.1 (pag 60), selected a sample of 248 dimuons and 2 trimuon events.

Comparing the dimuon sample to single muon events we have shown that a physical signal is present in our sample.

Applying an isolation cut we separate heavy flavour semileptonic decay from Drell-Yan and quarkonia decays. Fitting our data we estimate the cross section for J/Ψ production to be :

$$\sigma_{J/\Psi} * BR\,(J/\Psi \rightarrow \mu^+\mu^-) = 291 \pm 87_{stat} \pm 199_{syst}\ nb$$

From our fit we have also a measurement of the J/Ψ mass and of its width :

$m_{J/\Psi} = 3064 \pm 72$ MeV

$\Gamma_{J/\Psi} = 178 \pm 98$ MeV

We set also a limit on Υ cross section° with a 90% confidence level :

$$\sigma_{\Upsilon} * BR\,(\Upsilon \rightarrow \mu^+\mu^-) < 28 \pm 14_{stat} \pm 18_{syst}\ nb$$

For the Drell-Yan cross section we find that :

$$m^3 \left.\frac{d^2\sigma}{dm\,dy}\right|_{y=0} = 52 \pm 19_{stat} \pm 46_{syst}\ \ nb\,GeV^2$$

This value is consistent with previous measurements, as shown in fig 6.13 .

The goal of the research carried on at Fermilab, by the analysis of 1987 data, was Threefold : to study some interesting physics, as discussed in this thesis; to understand the limits of muon reconstruction and, eventually, to improve them; to prepare and to test a set of analysis modules that will make easier and faster the analysis of new data.

In this thesis we discuss the first part, but some important results have been achieved also in the understanding and the improvement of the muon detector, of the trigger and of the reconstruction process followed in muon algorithm. These results gave already some very preliminary results in the analysis of the present run.

As mentioned in the first chapters, the new run started in July of this year . The run will last until May of 1989. The minimal goal for the integrated luminosity is 1 pb^{-1} . This goal seems to be possible to be reached thanks to the improvements both in the accelerator and in the detector performances.

The peak luminosity in 1987 run had been $4*10^{29}\,cm^{-2}s^{-1}$. This value is normally supplied, this year, and the peak luminosity has been an order of magnitude bigger. Besides the number of bunches now accelerated is six, instead of three.

Because of these improvements in accelerator performances the rate of events increased a factor of ten. The problem of the high rate was solved with the introduction of higher trigger levels :

• *Level 2* : This is a hardware level, similar to level 1. It sums up the transverse energy of adjacent towers, provided it is above a fixed threshold. In this way 'clusters' of energy are formed. The trigger select events on the basis of the number and the energy of these clusters. Another possible operation is the calculation of the 'missing E_t' of the event. A high imbalance in the total E_t of the event (>20GeV) is the indication of a hard neutrino. In this level the matching between muon stub and extrapolated CTC track is done.

• *Level 3* : differently from the other two, this one is a software trigger. Clean up modules and reconstruction modules are run to the output data of level 2. Additive cuts push the rate down to

≈ 1-2 hertz, that is the rate for writing on tape.

Concerning muon reconstruction in 1988/1989 run is present a dimuon trigger. This will enhance the trigger efficiency for the processes discussed in the thesis. The Forward Muon System is working adding 2/3 to muon geometrical acceptance. It is still prescaled (a factor of four the last week of october) and it has a high P_t threshold (Pt>10GeV). Nevertheless the basic problems are understood and there is work in progress for fixing them.

In conclusion our analysis has shown that a huge variety of physics can be studied analysing dimuon events. With more luminosity and with an apposite trigger, all the physical sources discussed in Chapter 2 will be possible to be studied at CDF Collider.

APPENDIX A - Testbeam setup

Starting October 1987 Meson Test (MT) beam line was dedicated to testing the CDF calorimeter performance. In fig A.1 we can see a schematic view of the MT beam line. CDF detector was placed at the MT6 station.

The 900 GeV proton beam hits a fixed target (MT2TGT0) producing a pion beam that is bended by two sets of dipoles magnets (MW2xxx , MT2xxx) 47 mrad (see fig B.2) . Additional targets can be inserted between the magnets of the first set (MT2TGTx) . These targets attenuate the beam energy. In stations three and four some quadrupole magnets (MTnQx) and some collimators (MTnCxx) concentrate the beam in a smaller transverse area. An extra bending of 6 mrad is given by other two dipole magnets (MT3WU). At this level an electron beam can also be produced by inserting the target located in station 3 (MTGT3). This target produces a spread beam of particles, mainly π^0's and charged π's . A 'sweeper' (MT3SW) sweeps out charged particles from the beam by a dipole magnetic field. In this just neutral pions are left. The pions decay in two γ's that are converted to electrons in the converter.

A Cerenkov counter (MT4CC) and a Synchroton Radiation Detector (MT5SRD) gave information about the quantity of electrons present in the beam. In station 5 a final bending was given the beam. From station 3 on Proportional Wire Chambers (MTnPWC) , Single Wire Drift Chambers (MTnSWDC), and Scintillator Counters (MTnSC) were used to monitor the beam intensity and it's shape.

At station 6 a coincidence between Scintillator Counters of different size defined a beam crossing. A Veto Counter (MT6SCV) vetoed on halo particles. It was simply a scintillator with a hole set in anti-coincidence with the other scintillators. Behind CDF detector a concrete wall and a scintillator were used to tag muons (MT6BS,MT6SCMU) . At the end several meters of concrete dumped the beam (MTDMP).

Only two wedges were carried to this calibration area. They were mounted on a pivot that could rotate, so that the beam could be directed in a fixed point of the wedge to calibrate the detector response tower by tower. The electronic and the trigger setup was exactly the same than the one used in the collision hall. The only difference was the presence of a master clock that gave the timing every 7 ms used by the trigger.

The response of muon chambers could be studied because of a muon contamination of the pion beam. Muon contamination depends upon the energy of the beam varying from 15%, for 40 GeV pion beams, to 1.4% for 100 GeV pion beams.

A thorough discussion of test beam aspects can be found in [28].

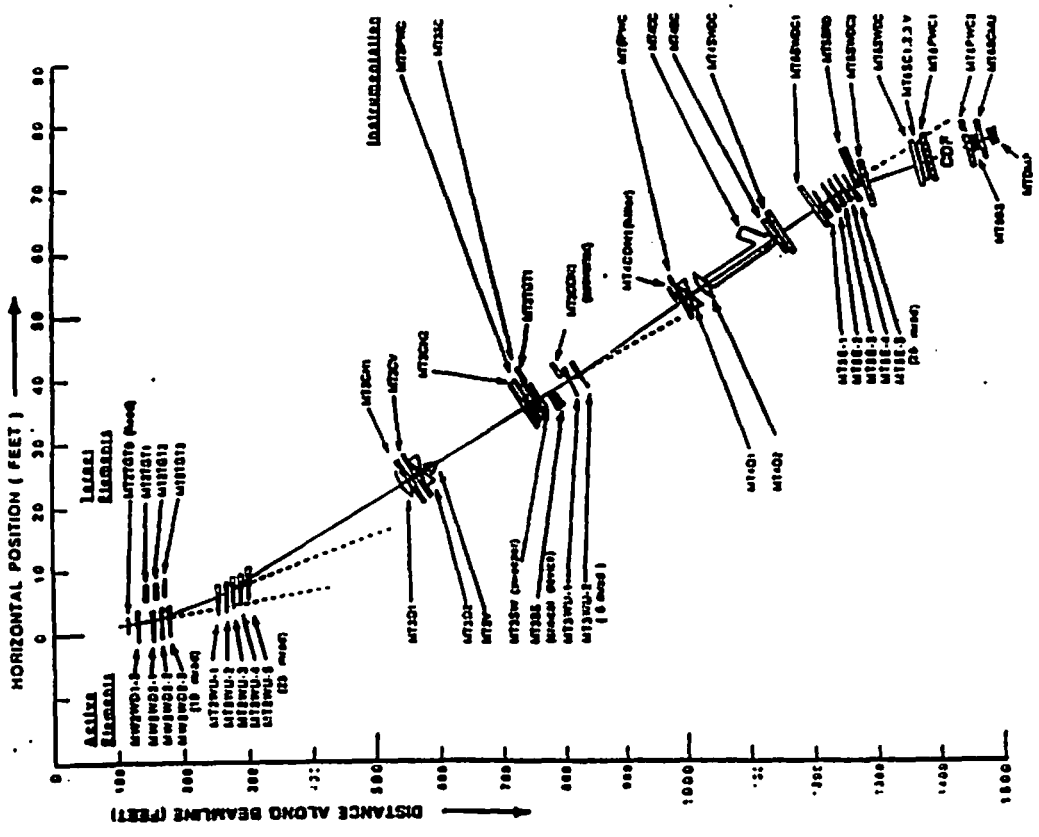

FIG A.1 - Meson beam line. In the figure is represented the setup used for CDF test beam run. The detector is located in the station MT6 .

APPENDIX B - Background sources

B.1 - Non interacting punchthrough

One of the main sources of background muons are hadrons, generally pions but also kaons, that reach the muon chambers without interacting inside the calorimeter. The probability for this to happen is, as already mentioned in the text, equal to :

The absorbtion length λ_{abs} can be expressed in terms of the absorbtion cross section as :

$$\lambda_{abs} = \frac{A}{N\rho\sigma_{abs}}$$

where :

A = atomic number
N = Avogadro's number
r = density of the material
σ_{abs} = absorbtion cross section

In our calorimeter the average value is :

$$\Lambda = 5.10 \quad \Rightarrow \quad P = \frac{1}{165}$$

This is just an approximation in what the cross section for strong interactions varies with the hadron P_t. The reason why we need a precise value of the cross section is that a small error on Λ has a big effect on P . In fact:

$$\frac{\delta P}{P} = \left(\frac{\delta \Lambda}{\Lambda}\right) * \Lambda$$

So a 10% error on Λ results in an error on the rate of non interacting punchthrough equal to :

$$\frac{\delta P}{P} = 10\% * 5.1 = 51\%$$

	σ_0 (mb)	α
K^+	20.37±0.80	0.791±.01
K^-	22.65±0.90	0.779±.01
π^+	25.64±1.00	0.764±.01
π^-	25.86±1.00	0.762±.01
p	37.99±1.48	0.719±.01
$\bar{p}$	43.50±1.73	0.698±.01

- TABLE 5.1 -

Parameters for the power-law fit to the A-dependence of the absorbtion cross-section for 60 GeV hadrons. [Carrol]

The uncertainty in the value of Λ is given by the uncertainties in σ_{abs} . Values reported in the Particle Data Booklet [15] regard hadrons colliding on protons. For heavier targets the cross section obeys a power law :

$$\sigma_{abs} = \sigma_0 A^{\alpha}$$

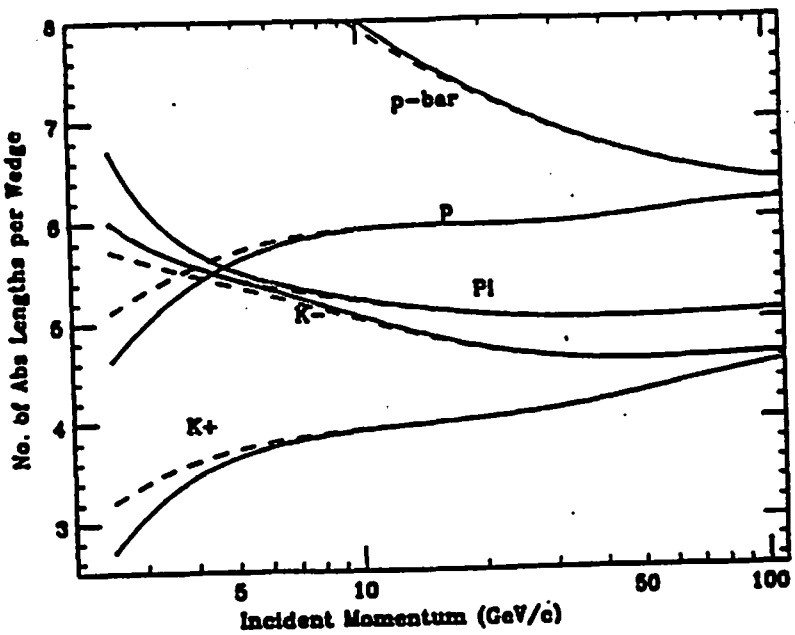

FIG B.1 - Number of absorbtion lengths (Λ) per wedge in function of the particle P_t. Dashed lines are derived from Carrol et al [24] scaling at low energies. Solid lines are corrections taking into account dE/dx released in the calorimeter.

FIG B.2 - Non-interacting punchthrough probability for different hadrons. a) Hadrons per punchthrough (e.g. at Pt=50 GeV 1 K+ every 100 punches through). b) Probability function.

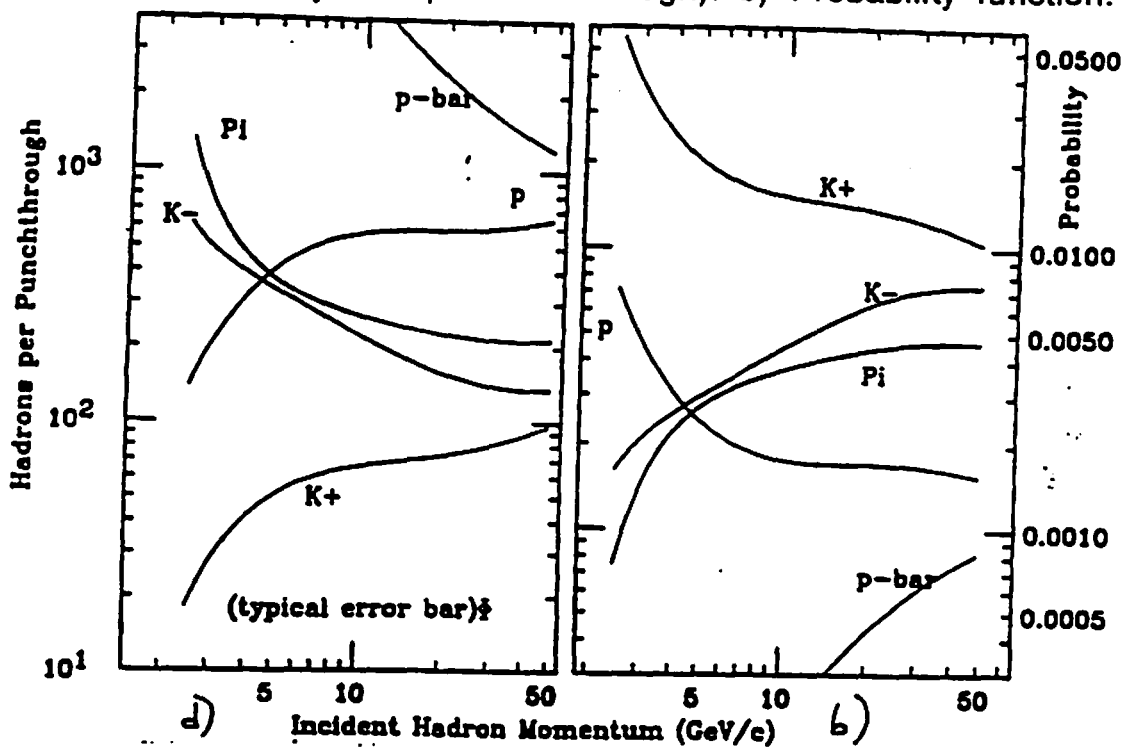

Table B.1 summarizes the values of σ_0 and α for different beams at 60 GeV [24] . To scale the value of the cross section at lower energies a comparison with testbeam data was made [23] .

In fig B.1 the value of the cross section is plotted as a function of the energy of the colliding hadrons. It has to be noticed that, while $\pi^+(u\bar{d})$ and $\pi^-(\bar{u}d)$ have an identical cross section, the strange mesons $k^+(u\bar{s})$ and $k^-(\bar{u}s)$ have not. The reason is that the anti-u quark of the k^- meson can annihilate with an u quark of a proton (uud) or of a neutron (udd) . This is not possible for k^+. On the other hand the quark couplings $p - \pi^+$ and $n - \pi^-$ are exactly the same. In fig B.2 the noninteracting punchthrough probability is represented. An overall value can be given combining the results of the different curves. For doing this we need an estimate of the relative fraction of hadrons present, in average, per event. We use UA5 results [27]. A mixing of 58% pions, 21% kaons and 20% protons gives the summary plot shown in fig 5.2 and reported here in fig B.3 .

FIG B.3 - Weighted sum of all the processes of fig B.2 . The weights are $\pi : k : p = 50 : 23 : 20$ (UA5 results [25]) .

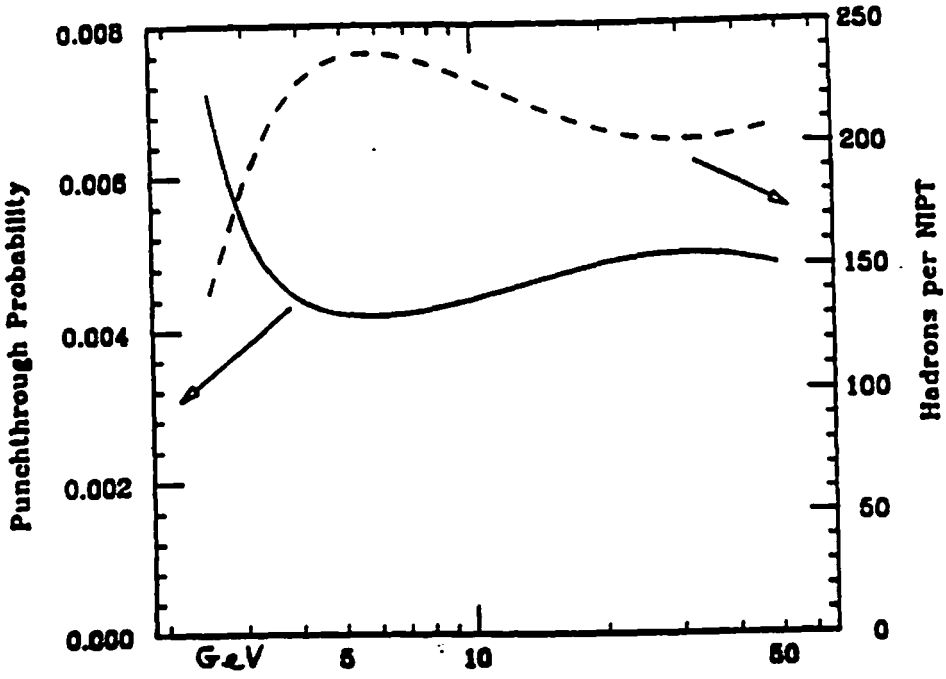

B.2 - Decays in flight

Muons can also be generated by decays in flight of hadrons. Though these are real muons, we consider them as background because not directly connected to the collision. Therefore we want to know the rate of events like :

$$\pi \rightarrow \mu\nu \qquad K \rightarrow \mu\nu$$

The probability that such a decay happen at a distance $r \leq R$ from the beam pipe, is :

$$P(P_t) = 1 - e^{-MR/c\tau P_t} \approx \frac{MR}{c\tau P_t}$$

where :

M = meson mass

$c\tau$ = decay length

If we take R = 347cm , the inner radius of the central muon chambers, we obtain:

$$P_{\pi->\mu\nu}(P_t) = \frac{0.062}{P_t(GeV)}$$

$$P_{K->\mu\nu}(P_t) = \frac{0.293}{P_t(GeV)}$$

The energy distribution of the muon produced in the decay process is flat for the allowed kinematical range :

$$c_M E_M \leq E_\mu \leq E_M$$

where :

E_M = meson energy

E_μ = muon energy

c_M = costant depending upon the meson type :

$c_\pi = 0.57$

$c_\mu = 0.05$

Thus, in principle, given a charge spectrum for pions and kaons, the spectrum of the decaying products can be straightforwardly computed. This simple picture has to be modified taking into account the following arguments :

- *Low secondary momentum* : decay muons have lower momenta than their parents, so they can not to fulfill our requirements. For example they can fail the momentum cut, or the matching cuts because of multiple scattering .
- *Muon energy lost* : energy lost inside the calorimeter slows down the hadron, increasing its decay probability .

Because of these effects, a more careful analysis, carried on with the help of Montecarlo simulation, is needed. For studying calorimeter effects, 3000 kaons and pions were generated at different momenta, with an uniform distribution in η and in ϕ [20].

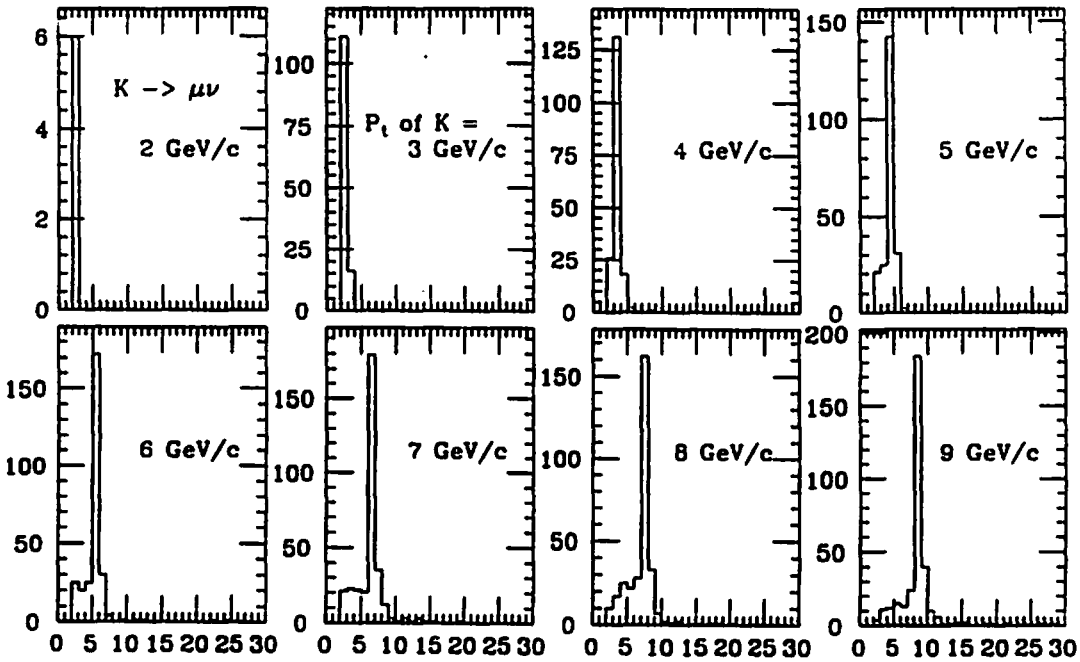

FIG B.4 - Probability for a pion of a fixed energy, specified in every diagram, of decaying in a muon having the momentum reported on the x axis.

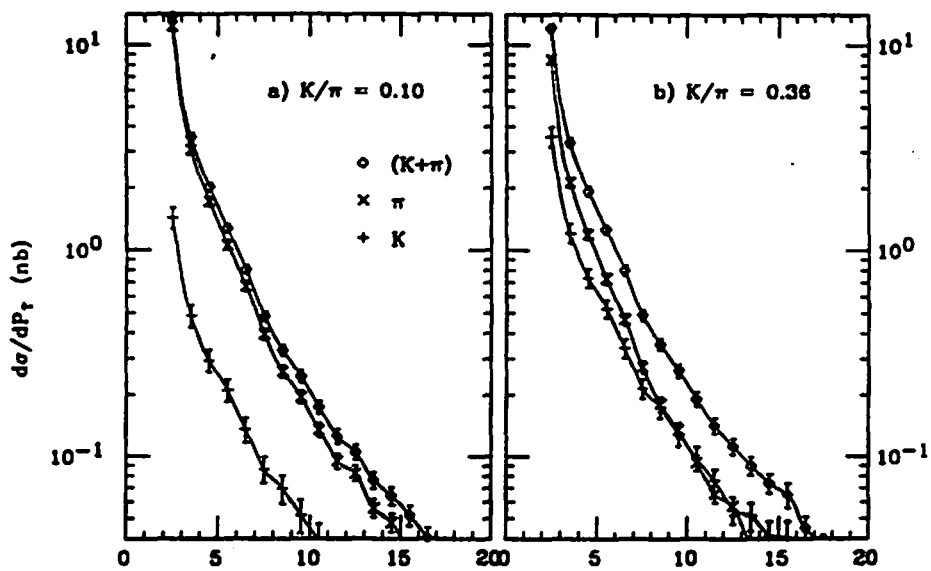

FIG B.5 - Pt distribution of muons from hadron decay given, as input, the spectrum of charged particles in jet events.

They were let decay inside the calorimeter and the emerging muon momentum was measured. Fig B.4 shows the values observed for the secondary muons according to CDFSIM (CDF simulation package) . Using this sample we can measure the output muon distribution of a given input spectrum of charged tracks. To do this we simply decompose the input distribution in momentum bins; we then let every bin decay according to our simulation.

Fig B.5 shows the output muon distribution, shown also in the text, if we take, as input, the spectrum of the charged tracks inside jet events. This result is obtained supposing a k/π ratio of 0.36 [25] .

REFERENCES

[1] Some standard books discussing te Standard Model are
• Aitchinson and Hey , 'Gauge theory in particle physics' (Adam Higler, Bristol, 1982)
• Leader and Predazzi , 'Introduction to gauge theory and the new physics', (Cambridge university Press, Cambridge, 1985)
• D. H. Perkins , 'Introduction to high energy physics', (Addison-Morley, Massachusset , 1982)

[2] • S.L. Glashow , Nucl. Phys. 22(1961)579
• S. Weinberg , Phys. Rev. Lett. 19(1967)579
• A. Salam , 'Elementary particle theory', (Stockolm 1968)

[3] Field and Feynmann , N. Phys. B136(1978)1

[4] Peterson et al. , Phys. Rev. , D27(193)105

[5] 'Design report of Tevatron I ' , FERMILAB (Sep-1984)

[6] Eitchen et al. , Rev. Mod. Phys. , 56(1984)579

[7] Drell and Yan , Phys. Rev. Lett. , 25(1970)316

[8] D. H. Perkins , 'Introduction to high energy physics' ([1])

[9] Anreasyan et al. , 'Associated multiplicity in μ-pair events at the ISR' , INFN PI/AE 86/9 (Submitted to Nuclear Physics)

[10] Eitchen , 'Theoretical expectations at collider energies' , Fermilab - Conf - 85/187 - T (1986)

[11] References on the contemporary discovery of the J/Ψ peak can

be found in :
• Aubert et al. , Phys. Rev. Lett. , 33(1974)1404
• Augustin et al. , Phys Rev. Lett. , 33(1974)1406
Concerning the Y, the first peak (Y') was found in Fermilab :
• Herb et al. , Phys. Rev. Lett. , 59(1977)1240

[12] Leader and Predazzi , 'Gauge theories and the new physics' ([1])

[13] Franzini and Lee-Franzini , in: ' e^+e^- annihilation : new quarks and leptons ' , (Robert Cahn editor, 1984)

[14] D. Sapirstein , Phys. Rev. Lett. , 43(1979)668

[15] 'Particle Data Booklet' , from 'Reviwe of particle properties', Phys. Lett. 170B(1986)

[16] Hans-Guenther Moser , Doktorarbeit , 'Dimuon production at the CERN pp collider' (1987)

[17] ARGUS collab. , 'ARGUS results in B°-B° mixing', V.Matveev talk in 'Production oand decay of heavy hadrons', Heidelberg(1986)

[18] CLEO collab. , Phys. Rev. Lett. , 53(1984)1309

[19] Albajar et al. , Phys. Lett. , 186(1987)247

[20] 'Design and construction of the Central Tracking Chamber' , Fermilab PUB-1987/182-E

[21] 'The CDF Vertex Time Projection Chambers' Fermilab PUB-1987/183-E

[22] 'Design report for the Fermilab Collider Detector Facility (CDF)' August, 1981

[23] D. Smith and H. Jensen , 'Pion punchthrough probability' CDF707 (1988)

[24] Carrol et al. , Phys Lett., 80B(1979)329
[25] UA5 collab. , Nucl. Phys. , 258(1985)505

[26] D. Smith and T. Westhusing , 'Decay in flight and acceptance of the Central Muon Chamber' , CDF726(1988)

[27] 'CDF Central Muon Detector' , Fermilab PUB-1987/179-E

[28] T.Kamon and F.Ukegawa , 'CDF Test Beam user's guide' , CDF618

[29] Arnison et al. , Phys lett B155(1985)442